Effects of Temperature Gradient in Inhomogeneous Superconductors Studied with Hybrid Quantum Interferometers

Connor Daniel Shelly

Supervisor: Prof. Victor Petrashov

Thesis submitted in part fulfilment of the requirement for the degree of Doctor of Philosophy from Royal Holloway, University of London

Declaration of Authorship

I, Connor Daniel Shelly, hereby declare that this thesis and the work presented in it is entirely my own. Where I have consulted the work of others, this is always clearly stated.

Signed: ____________________

Date: ____________________

Abstract

In this thesis we present an experimental investigation into the effects of temperature gradient in inhomogeneous superconducting circuits using a novel measuring method that allows the detection of genuine thermoelectric flux and its full separation from spurious effects present in all other measurement attempts to date. The method is based on the Andreev interferometer, a hybrid quantum interference device. A large number of interferometers were fabricated and tested to optimise the parameters of the device for sensitive magnetometry whilst minimising the intrusive effects of the read-out. To this end, a 'folded cross' geometry of the interferometer was developed to minimise spurious flux coupling during measurement. Investigation of the critical current in the interferometer led to a novel π-junction device. To avoid hysteresis during measurements a full investigation into the Josephson screening current and its effects on the interferometer was undertaken. Further device fabrication and investigation iterations allowed us to establish the design rules for an interferometer optimised for specific experiments. The practical elements of both the nano-fabrication and the experimental low-temperature, low-noise set-up are discussed. Installation of an experimental set-up in a dilution fridge as well as a ^{3}He system allowed for investigation of the devices in a wide temperature range between 20 mK and 1.6 K. The experiment presented explains why previous measurements were in gross discrepancy with theoretically predicted values. A theory was tested that calculates the thermoelectric flux by minimizing the energy of the system and uses the relationship between the thermoelectric current to the heat flow in the loop. An excellent agreement with the experimental results was found.

Acknowledgements

First and foremost I would like to thank my supervisor, Professor Victor Petrashov, for the support and guidance given to me during this work. His patience with my questions, and his enthusiasm for the work have been a continuing source of encouragement. In particular I would like to acknowledge the huge time spent discussing the analysis of the work in the later chapters, time that often ate into his weekends!

I would also like to thank Dr Rais Shaikhaidarov, who spent a considerable amount of time teaching me the nano-fabrication and low-temperature measurement techniques that I have relied upon throughout this work.

During the early stage of my PhD, I had the privilege of working with Dr Chris Checkley and Dr Andrea Iagallo. The techniques they taught me and the advice they gave me during this time have been invaluable.

I gratefully acknowledge the assistance received from Ekaterina Matrozova during her time spent working with me on the thermoelectric flux experiment.

Much of the work presented in this thesis began in the clean room - I have been lucky enough to share this space with a number of academics and fellow students - in particular I would like to thank Dr Vladimir Antonov, Dr Ray Davis and Dr Richard Marsh for their help, and company, during many long days of fabrication.

During the renovation of the dilution refrigerator I received a lot of advice and assistance; in this regard, Dr Phil Meeson, Dr Andrew Casey and Dr Jan Nyeki were particularly generous with their time. Dr George Nichols was generous with both his time and his thermometers!

I am very grateful for the technical assistance Massimo Venti has given throughout this work - without his help most of this work would still be at the drawing board stage. In addition to his technical expertise I appreciate his willingness to share life advice with me! I would like to thank Francis Greenough for always ensuring a steady supply of liquid helium to keep my experiment cold, even if it meant coming in during his holidays.

Professor Jon Goff and Dr Stewart Boogert deserve thanks for acting as my advisor and moderator respectively. In the later part of my PhD they also helped secure additional, much needed funding.

I would also like to thank Gill Green, Ian Murray and Andy Alway for their assistance with technical and administrative issues throughout.

It is a pleasure to thank the other members of the Physics department who have made the last four years so enjoyable, including, Dr Chris Harrison, James Poulten, Thomas Higgs, Christopher Ellingham, Dr Paco Cordobes, Toby Willis, Tom Wren, Dr Uthay Sivaperumal, Dr Aya Shibahara, Dr Rob Ainsworth, William Shields, Dr Lev Levitin, Dr Antonio Corcoles, Frank Arnold, Dr Dave Pavitt, Dr Daniel Porter, Matt Willson, Terence Giles and Dr Jon Burnett. In particular, I would like to thank Dr Kristian Kent, Dr James Wells and David Voneshen for many engaging discussions...

Outside of Royal Holloway I would like to extend my thanks to Leigh, Peter, Senaka, Daniel, Nikki, Bhavini and Sam who have distracted me throughout my education. In addition to their friendship, I am indebted to Alex Hirst and Gareth Bird for their proofreading of this thesis.

I also acknowledge the friendship of all my colleagues at LinkLine, and the flexible working hours afforded to me.

I would like to extend my gratitude to Professor Jonathan Williams and Dr Jane Ireland for welcoming me into their research group at the National Physical Laboratory.

The biggest thanks must go to my parents and my sister, for their endless support. Without their encouragement I would not have embarked upon this PhD.

Finally, I would like to thank my girlfriend Lorraine, for her patience, and her friendship, during this research.

Contents

List of Figures

CHAPTER 1

Introduction

Investigations into thermoelectric effects in superconductors have been carried out for almost 100 years. The early work in the 1920s and 1930s [1–5] saw no evidence of any thermoelectric effects present in superconductors; in fact, the very existence of thermoelectric effects was in question due to the requirement, given by Meissner, that any thermoelectric current must be completely cancelled with a counter-flowing supercurrent. In 1944, Ginzburg [6] stated that the complete cancellation of the thermoelectric current does not generally occur in inhomogeneous superconductors, and thus the thermoelectric effect may indeed be observed in a superconductor. In 1974, both Galperin *et al* [7] and Garland & van Harlingen [8] predicted the generation of a thermoelectric magnetic flux in a loop made of two different superconductors - the bimetallic loop.

A number of attempts were made to experimentally verify this prediction during the 1970s and 1980s [9–13], resulting in a large range of reported thermoelectric flux values, all in disagreement with one another. Furthermore, some of the results were in discrepancy with the predicted values by up to five orders of magnitude. Some of the earlier works [13] discussed the possibility that their results could be masked by the temperature dependent penetration depth λ(T) that also arises when the bimetallic loop is subjected to a temperature gradient.

In 2003, during his Nobel Prize lecture, Ginzburg [14] discussed the field of superconductivity and superfluidity, and highlighted the existence of thermoelectric effects in superconductors as a topic of particular interest. Chapter 2 of this thesis discusses some of the theory and experiments conducted in the field of thermoelectric effects in superconductors.

The motivation of the work presented in this thesis was to observe the thermoelectic flux in a nano-fabricated bimetallic loop. In contrast to the previous experimental efforts, that used macroscopic bimetallic loops measured with a coupled SQUID, we use a nano-fabricated bimetallic loop that is coupled to a hybrid interferometer on the same chip. All other necessary components of the experiment, a heater, a thermometer and a magnetic field source, are also nano-fabricated onto the same chip. The hybrid interferometer is used as a read-out device relying on the properties of Andreev reflection; the physics behind this phenomenon, and hybrid devices in general, are discussed in Chapter 3.

Details of the nano-fabrication techniques required to make the multi-layer devices are covered in Chapter 4. All samples were fabricated using the facilities available at the clean rooms of Royal Holloway, University of London. The low temperature facilities at Royal Holloway are discussed in Chapter 5, including details of the experimental set up of both a pumped ^{3}He system and a dilution refrigerator.

As the work in this thesis is based around the hybrid quantum interferometer as a read-out device it is necessary to investigate and optimise the device for optimal operation as a detector of thermoelectric magnetic flux. A number of experiments are performed in Chapter 6 that show that the hybrid interferometer can be operated in different regimes and can be tuned by application of a bias current. Both the hysteretic and non-hysteretic regimes are investigated - the non-hysteretic regime provides a sinusoidal relationship of the resistance to the phase of the junction and is used later in the detection of thermoflux. The hysteretic regime is investigated in its own right and is shown to behave as a latching read-out device. The critical current dependence on temperature, junction length and control current are also demonstrated. Finally a novel observation of the superconducting π-effect is presented.

The full details of the investigation into the detection of thermoelectric flux, in a bimetallic loop using an optimised hybrid interferometer are presented in Chapter 7. In this chapter, a set of equations describing the components of the magnetic flux in each of the loops are shown which relate the measurable quantities to the equation of a plane. The spurious flux caused by the temperature dependent λ-effect is separated to reveal only the true thermoelectric flux.

CHAPTER 2

Thermoelectric Paradox in Superconductors

2.1 Theory of Thermoelectric Phenomena

When a normal metal is heated at one end, a temperature gradient is produced. This causes a diffusion of the charge carriers from one end to the other, resulting in a potential difference between the two ends of the metal. The 'conversion' of a temperature gradient to a voltage difference is known as the *thermoelectric effect*. The transport equation for the electrical current density in a normal metal is given by [15],

$$\vec{j} = \sigma\vec{E} - \eta\vec{\nabla}T, \tag{2.1}$$

where σ is the electrical conductivity, $\vec{E}$ is the electric field, η is the thermoelectric coefficient and ∇T is the temperature gradient across the system.

Consider two normal metals with differing thermopowers connected together at a junction. A voltmeter is connected across either end of the metals (see Figure 2.1). The voltage difference measured when the junction is heated is given by,

$$\Delta V = \int_{T_1}^{T_2} (S_{\mathrm{A}} - S_{\mathrm{B}})\mathrm{d}T. \tag{2.2}$$

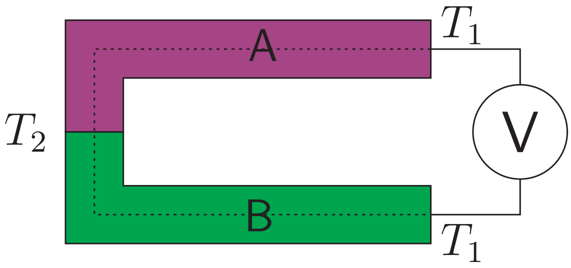

Figure 2.1: Typical measurement setup to observe the Seebeck Effect: Two different metals, A and B, are coupled and heated to T_2 at the junction. A voltmeter is connected across regions of same temperature T_1.

This is defined as the *Seebeck effect* where S_A and S_B are the Seebeck coefficients of the two metals. T_2 is the temperature of the junction where the two metals meet - this point is heated. The other end of each metal is maintained at a constant temperature T_1. Closely related to the Seebeck effect is the *Peltier effect* and the *Thomson effect*, each connected to one another via the Thomson relations [16]. After the discovery of superconducting materials it was only a matter of time before their thermoelectric properties were investigated. The first attempt to measure thermoelectric phenomena in a circuit of two superconductors, subject to a temperature gradient, was made by Meissner in 1927 [1]. No Seebeck effect was observed in this experiment. Further experiments by Borelius *et al* [2], Keesom & Matthijs [3], Casimir & Rademakers [4], and Burton *et al* [5] similarly showed no evidence of an observable Seebeck effect. However, lack of experimental observation of the Seebeck effect in a superconducting circuit does not mean that there are no thermoelectric effects in superconductors [14, 15].

In 1944 Ginzburg [6] claimed that there could be thermoelectric effects in a superconducting circuit. The two-fluid model (see, for instance, [17, 18]) states that both a superconducting current, $\vec{j}_\mathrm{s}$, and a normal current, $\vec{j}_\mathrm{q}$, carried in the form of quasiparticles, exist in the superconductor. Consider a length of bulk superconductor such that the ends are at temperatures T_1 and T_2, as shown in Figure 2.2. As a result of this temperature gradient, normal quasiparticles will flow from hot to cold resulting in a current flow,

$$\vec{j}_{\mathrm{q}} = -\eta \nabla T. \tag{2.3}$$

The normal quasiparticle current is compensated by a flow of the supercurrent in the opposite direction. Obeying the Meissner effect, the total current in the interior of a bulk isotropic homogeneous superconductor must be equal to zero [19, 20], $\vec{j} = \vec{j}_{\mathrm{q}} + \vec{j}_{\mathrm{s}} = 0$ thus,

$$\vec{j}_{\mathrm{s}} = -\vec{j}_{\mathrm{q}} = \eta \nabla T. \tag{2.4}$$

From this requirement it was considered impossible to observe the effects of the thermoelectric current in a superconductor when it is exactly cancelled. This led to textbooks of the day claiming that the thermoelectric effect is entirely absent from superconductors [21]. However, in the case of a non-uniform or anisotropic superconductor the quasiparticle current and supercurrent do not exactly cancel one another, leading to a finite current flow within the magnetic field penetration depth, $\lambda(T)$. An example of a non-uniform superconducting system is described in the next section.

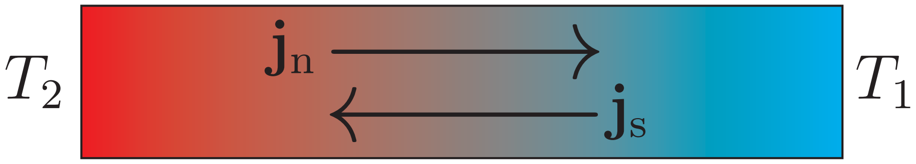

Figure 2.2: A rod of superconducting material with an established temperature gradient across its length is shown. The normal component of the current flows from one end of the rod to the other. Due to the requirement that the total current in a superconductor must be equal to zero the superconducting component flows in the opposite direction to compensate the normal current flow.

2.1.1 The Bimetallic Loop

It was suggested in 1974, by two separate groups [7, 8], that a non-uniform superconductor can be created by forming a closed ring of two different superconductors, resulting in the *superconducting thermocouple* or *bimetallic loop*. A simple schematic of the bimetallic loop is shown in Figure 2.3.

From the second Ginzburg-Landau equation the supercurrent can be written as,

$$\vec{j_\mathrm{s}} = \frac{\hbar n_\mathrm{s} e}{2m} \nabla\theta - \frac{e^2}{mc} n_\mathrm{s} \vec{A}. \tag{2.5}$$

Recall that $\vec{j_\mathrm{n}} = -\vec{j_\mathrm{s}}$, therefore,

$$\nabla\theta = \frac{2m}{\hbar n_\mathrm{s} e} \eta \nabla T + \frac{2e}{\hbar c} \vec{A}. \tag{2.6}$$

Equation 2.6 is then integrated over the contour passing through the interior of the bimetallic ring. Ginzburg-Landau theory also requires that the wavefunction must be single-valued, that is,

$$\oint \nabla\theta \mathrm{d}l = 2\pi n, \quad n = 0, 1, 2, \ldots \tag{2.7}$$

Therefore, integrating Equation. 2.6 results in,

$$2\pi n = -\frac{2m}{\hbar e} \int_{T_1}^{T_2} \left(\frac{\sigma_1 \alpha_1}{n_\mathrm{s1}} - \frac{\sigma_2 \alpha_2}{n_\mathrm{s2}} \right) \mathrm{d}T + \frac{2\pi\Phi}{\Phi_0}, \tag{2.8}$$

where,

$$\Delta\theta = \frac{2m}{\hbar e} \left(\frac{\sigma_1 \alpha_1}{n_\mathrm{s1}} - \frac{\sigma_2 \alpha_2}{n_\mathrm{s2}} \right) \Delta T. \tag{2.9}$$

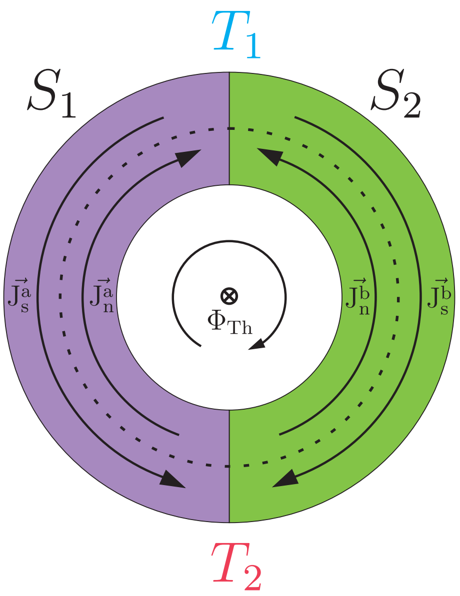

Figure 2.3: A bimetalic loop made of two different superconductors (S_1 - purple, S_2 - green) with junctions maintained at temperatures T_1 and T_2, where $T_2 > T_1$. In the bulk of the superconductor the normal current is cancelled by a counterflowing supercurrent.

At this point, most studies in the available literature connected $\Delta\theta$ to $\Phi_{\mathrm{Th}}/\Phi_0$.

As stated previously, a potential difference will appear across a thermocouple made of two differing normal metals. Although Van Harlingen *et al* [12] note that the analogous situation in a superconducting thermocouple is a quantum mechanical phase difference $\Delta\theta$ appearing across the thermocouple they too immediately connect $\Delta\theta$ to $\Phi_{\mathrm{Th}}/\Phi_0$.

A more recent paper by Gurevich *et al*, published in 2006 [22], takes a different approach. When a bimetallic loop is subject to a temperature gradient, a circulating current I_{cs} is established within the superconducting penetration depth $\lambda(T)$ (see Section 2.3). Gurevich *et al* suggest a method of calculating the circulating current by minimising the total energy of the bimetallic loop,

$$W = \frac{1}{2}(I_{\mathrm{n}} - I_{\mathrm{cs}})^2 \mathcal{L}_{\mathrm{k}} + \frac{1}{2} I_{\mathrm{cs}}^2 \mathcal{L}, \tag{2.10}$$

which results in,

$$I_{\mathrm{cs}} = I_{\mathrm{n}} \frac{\mathcal{L}_{\mathrm{k}}}{\mathcal{L}_{\mathrm{k}} + \mathcal{L}}, \tag{2.11}$$

where $\mathcal{L}_{\mathrm{k}}$ is the kinetic inductance of the loop and $\mathcal{L}$ is the geometric inductance. The method detailed above results in the thermoelectric flux, Φ_{Th}, being determined by the product of the circulating current and the geometrical inductance,

$$\Phi_{\mathrm{Th}} = \mathcal{L} I_{\mathrm{cs}} = I_{\mathrm{n}} \frac{\mathcal{L}_{\mathrm{k}} \mathcal{L}}{\mathcal{L}_{\mathrm{k}} + \mathcal{L}}. \tag{2.12}$$

This argument differs from that of Equations 2.8 and 2.9 which rely on complete compensation of the currents, $\vec{j}_{\mathrm{n}} = -\vec{j}_{\mathrm{s}}$, thus $I_{\mathrm{cs}} = 0$. Gurevich *et al* show that if the circulating current is zero then no thermoelectric flux should be observed.

2.2 Experimental Read-Out of Thermoflux

The first experimental measurement of thermoflux was presented by Zavaritskii in 1974 [9]. A closed superconducting loop of Sn-Pb was measured and showed results comparable to that predicted by theory. However, a series of experiments performed after Zavaritskii show discrepancies with theory. In 1976, Falco [10] observed thermoflux of the order $10^{-3}\,\Phi_0\,\mathrm{K}^{-1}$ using SQUID detection of flux in a Nb-Ta bimetallic loop. A number of experiments by van Harlingen *et al* [11,12] were performed using a geometry analogous to that of the bimetallic ring. The device was a toroid made from two different superconductors (In and Pb) coupled to a SQUID magnetometer (schematic of toroid and measurement setup shown in Figure 2.4). The results from this experiment showed a very large discrepancy from theory with reported thermoflux as large as $10^{5}\,\Phi_0\,\mathrm{K}^{-1}$.

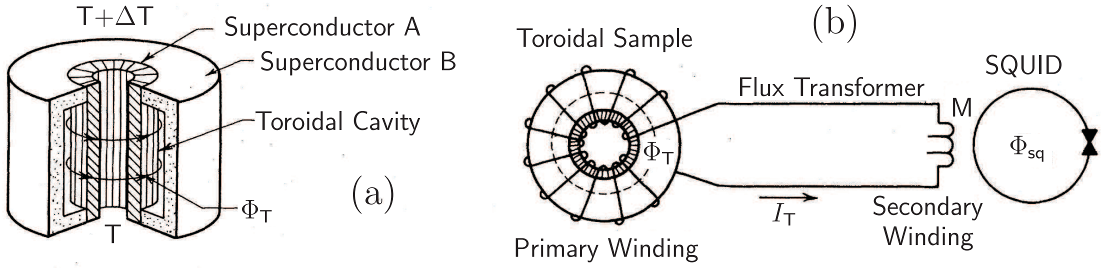

Figure 2.4: Experimental setup of experiment performed by van Harlingen *et al* [11,12]. (a) shows the device which is a toroid made of two different superconductors, in this case, indium and lead. Heating of one of the faces results in a temperature difference and a magnetic flux forming within the toroidal cavity. (b) shows a more detailed look at the means of detecting the thermoflux - a superconducting flux transformer allows coupling between the toroid and the SQUID magnetometer. The flux in the cavity induces a current in the transformer which is then detected by the SQUID. Image edited from [12].

The authors note that, despite taking all possible precautions, it is possible their results are due to measurement of ‘spurious effects’. A possible explanation of the large discrepancies between some of the experiments and theory was given by Pegrum & Guénault [13]; they make the suggestion that the previous experiments may have been measuring a change in flux due to the temperature induced changes in the superconducting penetration depth, $\lambda(T)$ (see Section 2.3). Pegrum & Guénault subsequently note that the trapped flux in the system should be very small in order to observe true thermoflux. To achieve this, one must have the ability to control the number ($k\Phi_0$) of trapped flux within the bimetallic loop in their experiment. With no control of the flux trapped inside the bimetallic loop, large measurements of the $\lambda(T)$-effect can be mistaken for unusually large thermoelectric flux observations. Kozub [23] makes the assertion that previous measurements may be including a spurious component from the redistribution of flux caused by the temperature dependence of $\lambda(T)$. Gurevich *et al* [22] also cast doubt on the experiments presented by van Harlingen *et al.* In particular, although the authors take great care to reduce background magnetic field in their bimetallic device (the toroid), a large magnetic field is able to penetrate the gap between the toroid and the measuring coil. Again, due to the temperature dependent nature of $\lambda(T)$ the magnetic flux trapped in the gap can indeed be temperature dependent and mistaken for a very large thermoflux. In 1985, Kozub [24] suggested another mechanism for the observation of thermoflux far higher than that predicted by theory. Consider the contact region between the two superconductors, one with higher T_c and one with lower T_c; it is possible that there is a large contact thermoelectric contribution to the measured flux due to phonon drag [25]. At the contact, the phonons from one superconductor (with high T_c) are irradiated into the other superconductor 'dragging' the quasiparticles with them. Due to this effect, the measured thermoflux can exceed theory by up to two orders of magnitude (by a factor of $\epsilon_\mathrm{F}/\Theta_\mathrm{D}$ [24–26]). However, the enhancement factor from phonon drag is insufficient to resolve the disparity between theory and the experimental results.

2.3 Temperature Dependent λ(T)-effects in Superconductors

When a superconducting material is placed into a magnetic field it is expected that, due to the Meissner effect, the magnetic field will be expelled from the superconductor. This is not precisely what happens; instead the magnetic field is able to penetrate the superconductor up to a certain distance from the surface. Consider a superconductor, the surface of which resides on the plane $x = 0$. By solving the second London equation, subject to boundary conditions $B(0) = B_0$ and $B(\infty) = 0$, we arrive at the following,

$$B = B_0 e^{-x/\lambda}, \tag{2.13}$$

where,

$$\lambda = \sqrt{\frac{m}{\mu_0 n_\mathrm{s} e^2}}, \tag{2.14}$$

m is the effective mass, e is the charge and n_s is the density of Cooper pairs. The consequence of the penetration depth is that the magnetic field can indeed penetrate a superconductor decaying over the characteristic decay length, λ. As λ depends on the number density of superconducting carriers it follows that the penetration depth is a temperature dependent quantity; as temperature is increased the penetration depth increases. The temperature dependence of λ is given by,

$$\lambda(T) = \frac{\lambda(0)}{[1 - (T/T_\mathrm{c})^4]^{1/2}}, \tag{2.15}$$

where d is the film thickness. The values of $\lambda(0)$ are given for a number of superconductors in Table 2.1

Table 2.1: Penetration depth values given for a selection of superconductors. Materials used within this work shown in bold. Data collated from [20, 27].

	Al	Cd	In	Nb	**Pb**	Sn	Tl	YBCO
$\lambda(0)$ (nm)	**50**	130	64	47	**39**	51	92	170

It is important to note that the $\lambda(T)$-effect can mask the true thermoelectric flux: In 1978, further measurements of superconducting loops by Guénault & Webster [28] show evidence of a thermally generated magnetic flux. The experimental set-up was identical to that of [13] but this time the authors measured a loop made of a single superconductor - tin. As this is a uniform superconductor, the thermoflux, as defined by Ginzburg, should not be observed; this experiment serves as a test of the temperature dependence of the $\lambda(T)$-effect. The temperature dependence of this flux varied as $(1 - (T/T_\mathrm{c})^4)^{-1/2}$ as expected for a penetration depth effect. The sign and magnitude of the signal depends on the flux trapped within the loop unlike a true signal of thermoflux which should depend only on the direction of the temperature gradient. This experiment further highlights the importance of controlling the trapped flux within the bimetallic loop and accounting for the $\lambda(T)$-effect inherent in any of these measurements.

When the penetration depth varies due to a change in temperature it is clear that the effective area of the superconducting loop will also change. The geometrical loop inductance and thus the mutual inductance between two loops are also subject to change.

Brandt and Clem [29] state that in superconducting ring structures, such as SQUIDs, a finite $\lambda(T)$ is of particular importance. Some of the magnetic flux is able to penetrate not only the free space inside the SQUID loop but also in some of the superconducting film making up the ring. As well as a change of effective area, the geometrical inductance is altered.

Hao *et al* [30] have performed an experiment to determine the temperature dependent penetration depth in washer-type SQUIDs. They state that conventional rule-of-thumb expressions for inductance and effective area do not take into account the flux penetration into the thin-film superconductor. The measured penetration depth is shown in Figure 2.5. Note that the authors present the Pearl length, Λ, which is related to the London penetration depth by $\Lambda = (\lambda_0^2/d)/[1-(T/T_c)^4]$.

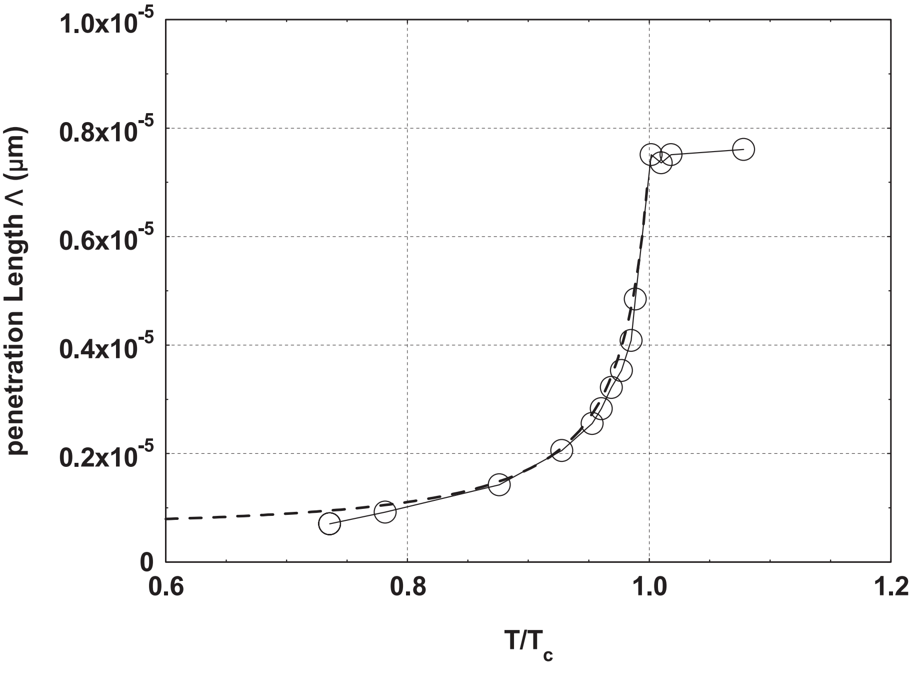

Figure 2.5: Penetration depth $\Lambda(T)$ vs T. Image taken from Hao *et al* [30].

2.4 Summary

In this chapter, the field of thermoelectric effects in superconductors have been introduced. A brief history of some of the earliest experiments are presented which searched for Seebeck effects in superconductors - all of these early experiments lacked an experimental observation of the Seebeck effect. A brief discussion of Ginzburg's 1944 prediction has been presented which states that a thermoelectric current can be carried by the normal quasiparticles which exist in a superconductor. The superconducting bimetallic loop is introduced as a possible system in which the thermoelectric magnetic flux may be observed. A summary of the previous experimental efforts towards observing the thermoelectric magnetic flux are also presented. The large discrepancy between experimental results and the values expected from the theory is highlighted: Possible causes of this discrepancy are also mentioned including the temperature-dependent λ-effect which is discussed in more detail in the latter part of this chapter.

CHAPTER 3

Hybrid Quantum Interference Devices

3.1 Andreev Reflections and Proximity Effects in Hybrid SN Systems

3.1.1 The Superconducting Proximity Effect

When a normal metal is placed in good contact with a superconductor, Cooper pairs will penetrate into the normal metal and remain coherent for a certain distance. A result of this is that a thin layer of normal metal close to the SN boundary will become superconducting. There is also a reduction in the Cooper pair density in the superconductor close to the SN boundary. This can be described in terms of the superconducting order parameter Ψ. Ginzburg & Landau described the order parameter such that $|\Psi(r)|^2 = n_s$, where n_s is the density of Cooper pairs [31]. Consider the situation where a normal metal and superconductor are in contact such that the interface between them is at $x = 0$. In the normal metal the order parameter will be small ($\psi \ll 1$) so the first Ginzburg-Landau equation can be

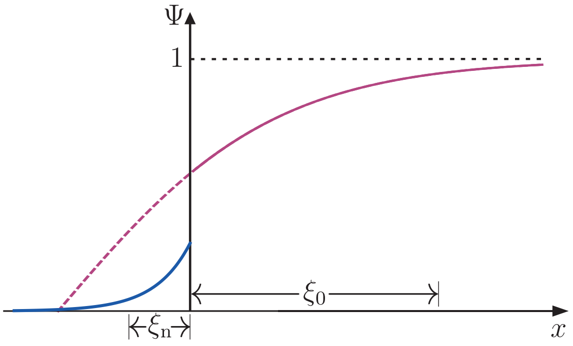

Figure 3.1: Variation of the order parameter about the NS interface.

written in the following form;

$$-\xi_\mathrm{n}^2 \frac{\mathrm{d}^2\psi}{\mathrm{d}x^2} + \psi = 0. \tag{3.1}$$

Using the condition that ψ will tend to zero deep in the normal metal (as $x \to \infty$) the solution is given as,

$$\psi = \psi_0 e^{-|x|/\xi_\mathrm{n}}. \tag{3.2}$$

The above is a simplified model but is qualitatively descriptive of the order parameter penetration. A more rigorous treatment is given in [32] which derives the coherence length as given in Equation 3.3. In the clean limit, when the mean free path, l_n is larger than the coherence length (i.e. $l_\mathrm{n} > \xi_0$) the normal coherence length is given as,

$$\xi_\mathrm{n} = \frac{\hbar v_\mathrm{F}}{2\pi k_\mathrm{B} T}. \tag{3.3}$$

In the opposite case, in the dirty limit ($l_\mathrm{n} < \xi_0$), the coherence length is given as,

$$\xi_\mathrm{n} = \sqrt{\frac{\hbar v_\mathrm{F} l_\mathrm{n}}{6\pi k_\mathrm{B} T}}. \tag{3.4}$$

The superconducting coherence length [33] is given by,

$$\xi_0 = a \frac{\hbar v_\mathrm{F}}{k_\mathrm{B} T_\mathrm{c}}, \tag{3.5}$$

where the microscopic BCS theory finds $a = 0.18$ [34]. A physical interpretation of this quantity is that of the size of the Cooper pair state.

3.1.2 Andreev Reflection: A Microscopic Mechanism of the Proximity Effect

Consider the interface between a superconductor and a normal metal. At low temperatures, ($\Delta \gg k_{\mathrm{B}}T$) a quasiparticle of energy within $k_{\mathrm{B}}T$ of the Fermi energy, incident on the SN boundary is unable to enter the superconductor. The energy gap, Δ, restricts tunnelling of the normal quasiparticle as there are no states available in the superconductor [35]. In 1964, Andreev [36] proposed a mechanism to explain how charge transport can take place across an SN interface. When an electron with an energy above the Fermi level is incident on the SN interface, it combines with another electron from below the Fermi level forming a Cooper pair. Whilst the Cooper pair is able to travel into the superconducting condensate, a hole is *Andreev reflected* back into the normal metal. The Andreev reflection is a retro-reflection of the electron as a hole, whereby the velocity and charge are reversed, resulting in the hole retracing the path of the incoming electron. In contrast to an 'ordinary' reflection, all components of momentum are conserved during an Andreev reflection [37, 38]. An important feature of Andreev reflection is that the reflected hole will acquire a macroscopic phase χ from the superconductor. The superconducting order parameter is given as $\Delta e^{i\chi}$; therefore, the phase change associated with an incident electron of energy $\epsilon = \epsilon_{\mathrm{F}} + \delta\epsilon$ is given as,

$$\delta\phi = \chi + \arccos\left(\frac{\delta\epsilon}{\Delta}\right). \tag{3.6}$$

The distance over which the superconducting correlations can travel into the normal metal whilst remaining coherent is given by the energy dependent coherence length scale [39] described by,

$$L_{\delta\epsilon} = \sqrt{\frac{\hbar D}{\delta\epsilon}}, \tag{3.7}$$

where $D = \frac{1}{3} v_{\mathrm{F}} l$ is the diffusion constant. At $\delta\epsilon = k_{\mathrm{B}}T$ the above equation is identical to the dirty limit coherence length given by Equation 3.4. It is useful to define the energy at which the electrons will remain coherent over the entire length of the normal metal conductor. This energy is defined by letting $L_{\delta\epsilon} = L$ and is known as the Thouless energy [40],

$$\epsilon_{\mathrm{Th}} = \frac{\hbar D}{L^2}. \tag{3.8}$$

There is, of course, an ultimate upper limit on the length over which the electrons will remain coherent. This is considered by recognising that scattering events will affect the phase, causing the electrons to lose coherence. The length at which the electrons are no longer correlated is known as the phase breaking length, $L_\phi = \sqrt{D\tau_\phi}$ where τ_ϕ is the normal metal phase breaking time [41]. It will be seen later that this length scale is important, allowing for long-range proximity effects.

3.1.3 The Josephson Effect in SNS Junctions

In 1962, Brian Josephson [42] predicted that a supercurrent will flow between two superconducting electrodes separated by a tunnelling barrier. He defined the supercurrent in terms of the phase difference between the two electrodes as follows in the fundamental Josephson current-phase relation,

$$I_{\mathrm{s}} = I_{\mathrm{c}} \sin(\chi_1 - \chi_2) = I_{\mathrm{c}} \sin\phi, \tag{3.9}$$

where $\chi_{1,2}$ are the macroscopic phases of the superconducting electrodes and I_{c} is the critical current of the junction. This fundamental relationship is known as the *dc Josephson Effect*. The critical current defines the maximum dissipationless supercurrent that the junction can support; if the current exceeds I_{c} then a finite voltage drop will be present across the junction. The second fundamental Josephson equation, the *ac Josephson effect*, relates a time-varying phase to a fixed voltage drop across the junction,

$$\dot{\phi} = \frac{2e}{\hbar}\bar{V} = \frac{2\pi}{\Phi_0}\bar{V}. \tag{3.10}$$

Although Josephson's predictions were based on an insulating tunnel junction between two superconductors (SIS), Josephson junction behaviour has been observed in a number of different 'weak links'. A weak link is simply defined as the region between two superconducting electrodes through which the critical current is much reduced from that of the electrodes [43]. In addition to the aforementioned SIS geometry, the weak link can be made by sandwiching a normal metal between two superconducting electrodes creating a SNS junction. Weak links can also be manufactured in any number of ScS geometries where 'c' denotes a constriction [33].

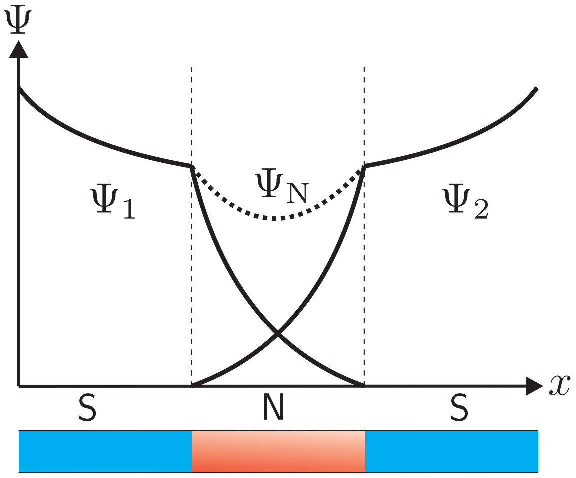

Figure 3.2: Superconducting wavefunctions overlapping in the normal region of a SNS junction. Finite order parameter and thus finite supercurrent observed in the normal region.

Consider now the SNS geometry where a normal metal is placed between two superconducting electrodes as shown in Figure 3.2. With a normal metal of sufficiently small length ($L < 2\xi_{\mathrm{n}}$) the superconducting wavefunctions will overlap. This means that coherent Cooper pairs can travel the length of the normal metal and support a finite supercurrent through the system. The critical current in the normal part of the SNS junction is lower than the critical current in the superconducting electrodes. This is due to the reduced condensate amplitude in this region, and thus, a reduced Cooper pair density. It was shown by de Gennes [44, 45] that the critical current is related to the length of the junction,

$$I_c(L) \propto \mathrm{e}^{-L/\xi_{\mathrm{N}}}. \tag{3.11}$$

It follows that the temperature dependence should be given by [46],

$$I_c(T) \propto \mathrm{e}^{\sqrt{-T/T_0}}, \tag{3.12}$$

where T_0 is a fitting parameter.
However, experimental results from Courtois *et al* [47] show a better fit to the typical ballistic dependence of,

$$I_c(T) \propto \mathrm{e}^{-T/T_1}, \tag{3.13}$$

where T_1 is a fitting parameter.
An experimental and theoretical study in 2001 by Dubos *et al* [45, 46] explained the measured temperature dependence using quasiclassical Green's functions in the diffusive limit. For long junctions ($L > \xi_{\mathrm{n}}$) the critical current can be written as,

$$eR_{\mathrm{N}}I_{\mathrm{c}} = \frac{32}{3+2\sqrt{2}}\epsilon_{\mathrm{Th}}\left[\frac{L}{\xi_{\mathrm{n}}}\right]^3 e^{-L/\xi_{\mathrm{n}}}, \tag{3.14}$$

Leading to a temperature dependence of

$$I_{\mathrm{c}} = T^{3/2}e^{-\sqrt{T}}. \tag{3.15}$$

3.1.4 Phase-periodic Electron Transport

In 1982, Spivak & Khmelnitskii [48] predicted that the weak localization correction to the resistance of a normal metal between two superconducting electrodes should oscillate as a function of the phase difference between the superconductors. The first experimental observation of phase interference effects in a SNS junction was presented by Petrashov *et al* in 1993 [49]. The device consisted of normal metal rings with superconducting 'mirrors' placed in different geometries (see Figure 3.3). Evidence of giant amplitude conductance oscillations were observed with a value of $\delta G \approx 3 \times 10^2 (e^2/h)$, two orders of magnitude higher than expected. An additional $h/4e$ period was also evident in the oscillations of some of the devices. Due to the geometry of these devices it was impossible to control the phase between the superconductors.

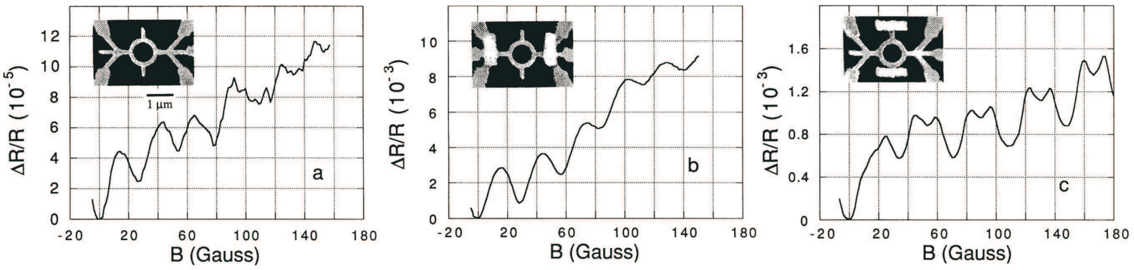

Figure 3.3: (a) shows the typical Aharonov-Bohm dependence of the resistance on magnetic field. Oscillations with flux quantum period, $\Phi_0 = h/2e$ are visible. (b) shows the device with superconducting 'mirrors' perpendicular to the current flow - this geometry also shows the $h/2e$ oscillations but at an enhanced amplitude of almost two orders of magnitude. (c) shows the device with the 'mirrors' parallel to the current flow. A similar amplitude enhancement to that of (b) was seen in addition to a $h/4e$ period of the oscillations. This extra periodicity was attributed to Andreev reflections at the interfaces. Image taken from [49].

In 1994, an experiment performed by de Vegvar *et al* [50] also showed phase dependent resistance oscillations. The geometry of this device was a Nb-Au-Nb SNS junction connected in parallel to an array of SIS junctions. By passing a current through the SIS array the phase difference between the superconducting electrodes could be tuned. Although the devices showed $h/2e$ periodicity, the oscillations demonstrated arbitrary phase at $\Delta\phi = 0$. Also in 1994 Petrashov *et al* [51] improved upon their previous experiment by connecting the superconducting 'mirrors' with a superconducting wire. Attached to the loop was a control line; this geometry allowed direct manipulation of the phase difference between the superconductors using either a 'control current' or by varying the magnetic field, and thus, the flux, linking the loop. The geometry of the device and phase dependent resistance oscillations are shown in Figure 3.4. The phase difference between the superconductors is described [52] by,

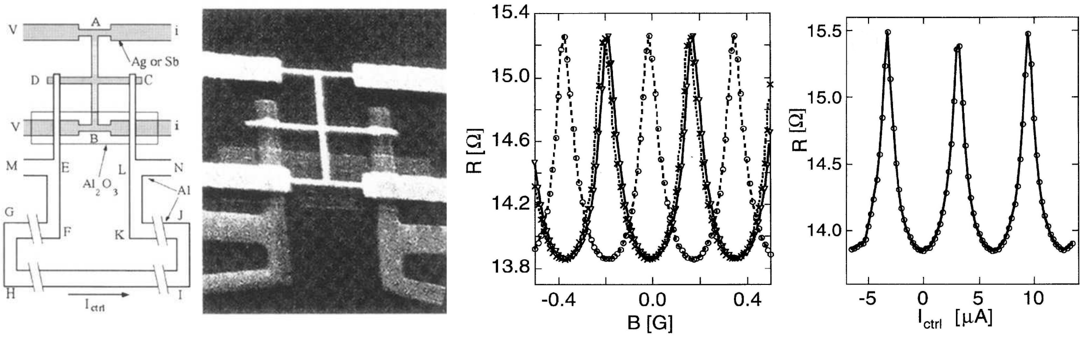

Figure 3.4: Schematic and SEM image of sample geometry from Petrashov's experiment [52]. Silver (or antimony) was used as the normal metal and was connected to aluminium superconducting leads which formed a loop with a control current line. Oscillations showing phase-dependent resistance oscillations where the phase is controlled using either a magnetic field or a control current. Note the non-sinusoidal nature of the oscillations. Data shown taken from the Al/Ag sample, Al/Sb not shown.

$$\phi = 2\pi \frac{\Phi_{\text{ext}} + \mathcal{L} I_{\text{ctrl}}}{\Phi_0}. \tag{3.16}$$

3.1.5 The Re-entrance Effect

The results from Petrashov's 1995 experiment [52] showing large amplitude conductance oscillations were analysed by Nazarov & Stoof [53]. They concluded that the diffusion coefficient, D, of the quasiparticles is altered by penetrating superconductivity causing a maximum in the conductance at temperatures close to to the Thouless energy, $\epsilon_{\text{Th}} = \hbar D/L^2$. A remarkable feature of the conductance of an SN interface is that, at low energies (low temperature and low bias), it does not decrease toward zero as one would expect from BTK theory [54]. Instead it was observed that as the SN interface is lowered in temperature the conductance will increase back to its normal-state value[1] in the absence of electron-electron interactions [55, 56]. This non-monotonic behaviour of the SN conductance is known as the *re-entrance effect*. The re-entrance effect can be explained by accounting for the two separate terms that contribute to the conductance of the normal metal [57];

$$\delta\sigma(\epsilon) = \delta\sigma_{\mathrm{DOS}}(\epsilon) + \delta\sigma_{\mathrm{AN}}(\epsilon). \tag{3.17}$$

The first term, $\delta\sigma_{\mathrm{DOS}}(\epsilon)$, is related to a decrease of the density of states in the normal metal as the temperature is reduced which results in a decrease of the conductance. The second term, $\delta\sigma_{\mathrm{AN}}(\epsilon)$, is known as the anomalous (or Maki-Thompson [58, 59]) contribution and results in an increase of the conductance. It is found that at $\epsilon = 0$ the two contributions are exactly equal leading to a 're-entrance' of the conductance to its normal state value. At higher energies the anomalous term exceeds that of the DOS term resulting in a maximum in the conductance which occurs when the energy in the system is roughly equal to the Thouless energy (i.e. $\epsilon_{\mathrm{Th}} \approx eV, k_{\mathrm{B}}T$). The effect of the two contributions to the conductance is shown in Figure 3.5.

---

[1] For an interesting discussion on why there is a finite resistance at a SN interface see Ref [38]

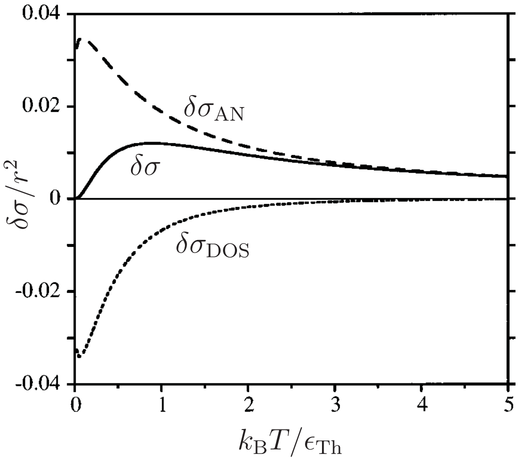

Figure 3.5: Temperature dependence of the conductance. The total conductance $\delta\sigma$ is shown by the solid line. The total conductance is determined from two contributions. The density of states term, $\delta\sigma_{DOS}$, is shown by the dotted line. The anomalous term $\delta\sigma_{AN}$ is depicted by the dashed line. Image edited from [60].

The first experimental observation of re-entrance was performed by the group of Pannetier [61] using a copper loop in contact with a superconducting aluminium island. When all involved energies were below that of the Thouless energy, the predicted re-entrance of the conductance was observed.

Further experiments performed by Petrashov *et al* in 1996 [62] and 1998 [63] confirmed the predictions of Nazarov & Stoof showing a maximum in the oscillation amplitude close to the Thouless energy with a reduced amplitude at both higher and lower temperatures. The theoretical predictions and the experimental results can be seen in Figure 3.6.

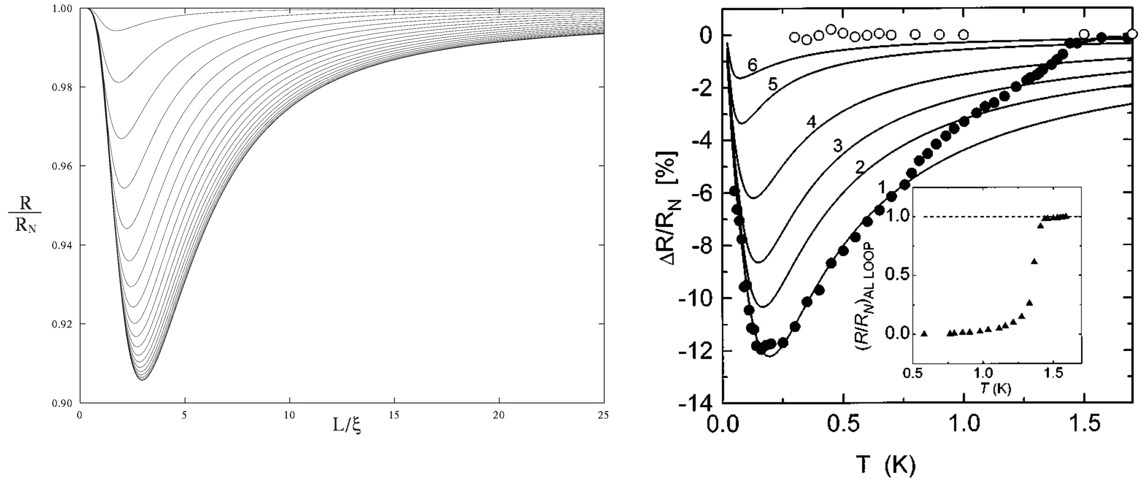

Figure 3.6: (left) shows the theoretical curves predicted by Nazarov and Stoof showing the a maxima in the resistance oscillations. (right) Experimental data taken by Petrashov *et al* for two Ag-Pb devices confirming the maxima in the resistance oscillations occurring close to ϵ_{Th}. Images taken from [53] and [63] respectively.

It is shown in Equation 3.11 that for a typical short Josephson junction the critical current decays exponentially as L/ξ_{n}. In contrast to this result are the conductance oscillations which decay as a power law in 1/T [64]. The separation of these two different contributions was shown by Courtois *et al* [65] demonstrating the contrasting short-range and long-range effects of the two contributions. Their results can be seen in Figure 3.7.

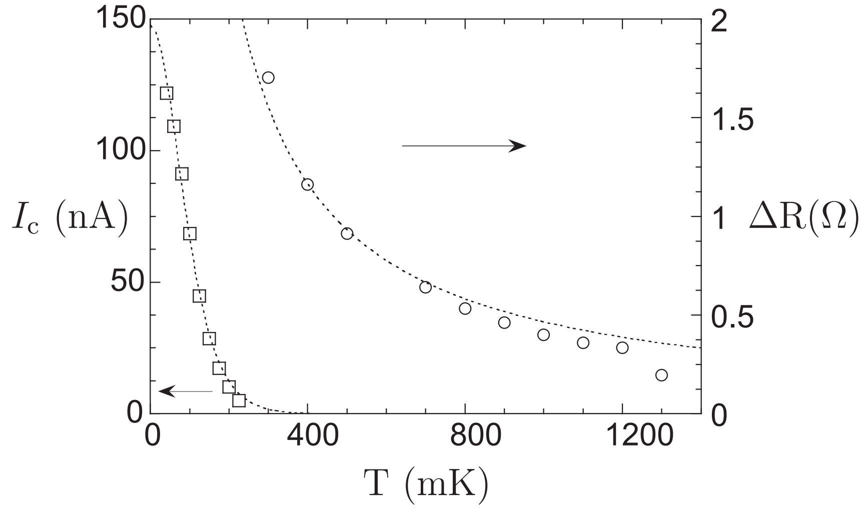

Figure 3.7: Temperature dependence of the critical current, I_c, shown (squares) on the left axis demonstrating the exponential decay with increasing temperature. The circles (right axis) demostrate the $1/T$ dependence of the long range conductance oscillations. Image edited from [65].

3.2 Metastable States in Hybrid Interferometers

It was also observed that the phase-dependent resistance oscillations were non-sinusoidal for the Ag/Al structure in Petrashov's experiment. It was suggested by van Wees *et al* [66] that due to L being comparable to ξ_n a supercurrent must flow between the two electrodes. An additional flux term due to the supercurrent-induced flux through the loop is added so the total flux threading the loop is given as,

$$\Phi = \Phi_{\text{ext}} - \mathcal{L} I_c \sin\left(\frac{2\pi\Phi}{\Phi_0}\right), \tag{3.18}$$

which can be rewritten conveniently as;

$$\varphi = \varphi_{\text{ext}} - \beta \sin(\varphi), \tag{3.19}$$

where $\varphi = 2\pi\Phi/\Phi_0$, $\varphi_{\text{ext}} = 2\pi\Phi_{\text{ext}}/\Phi_0$ and $\beta = 2\pi\mathcal{L}I_c/\Phi_0$.

Of importance is the screening term, β; at values of $\beta > 1$ the curve describing

$\varphi(\varphi_{\text{ext}})$ becomes increasingly non-linear. This gives rise to stable and unstable branches. In order to investigate this, Likharev's treatment [67] of the rf-SQUID is discussed. The potential energy of the system is given by,

$$U_{\text{S}}(\varphi) = E_{\text{J}}\left[1 - \cos\varphi + \frac{(\varphi - \varphi_{\text{ext}})^2}{2\beta}\right] + \text{const.} \tag{3.20}$$

It is shown in Figure 3.8 that several minima in the energy-phase diagram are present when $\beta > 1$. The extrema occur at;

$$\frac{\varphi - \varphi_{\text{ext}}}{\beta} = -\sin\varphi. \tag{3.21}$$

The critical flux φ_{c} can be determined from the inflection point criterion $U''_{\text{S}}(\varphi) = 0$. Therefore, $\cos(\varphi_{\text{c}}) = -1/\beta$. With this substituted back into Equation 3.20, the critical flux can be found at,

$$\varphi_{\text{c}} = \frac{\pi}{2} + \arcsin(\beta^{-1}) + \sqrt{\beta^2 - 1}. \tag{3.22}$$

This system can be modelled as a particle travelling in the potential given by Equation 3.20 [67,68]. By splitting the potential into its parabolic and oscillating components and varying φ_{ext}, one can observe a shift of the oscillating component relative to the parabolic part, as shown in Figure 3.8. At zero applied flux the particle is trapped in a single minimum. By increasing φ_{ext} the particles energy is smoothly raised until, at $\varphi_{\text{ext}} = \pi$, the two energy wells are at the same energy and the particle is trapped in one of them. Further increase of φ_{ext} results in a tilting of the system trapping the particle in a higher energy state. The barrier between the wells is lowered as the external flux is increased. Eventually the barrier is reduced sufficiently to allow escape of the particle to the lower well. The escape of the particle results in a sudden change of phase in the system, observed experimentally as a sharp drop in the measured resistance.

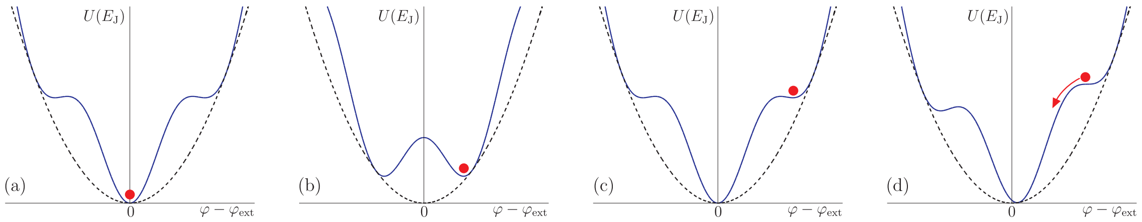

Figure 3.8: (a) $\varphi_{\text{ext}} = 0$: With zero applied flux the particle sits in the single minima. (b) $\varphi_{\text{ext}} = \pi$ As the flux is increased the particle is trapped in the right-hand-side well and increases in energy. (c) $\varphi_{\text{ext}} = 2\pi$: Profile of potential is 2π-periodic so identical to the first image, however the particle is now trapped in a higher energy state. (d) $\varphi_{\text{ext}} = \varphi_c$: As applied flux reaches its critical value the barrier is reduced sufficiently to allow the particle to fall down to the lower energy state.

The experimentally observed response of the resistance is shown in the data from Petrashov *et al* [62] shown in Figure 3.9. They show the temperature dependence of β and the corresponding changes to the magnetoresistance line-shapes. A discussion of the screening effect in superconducting systems can be found in Refs [67, 69].

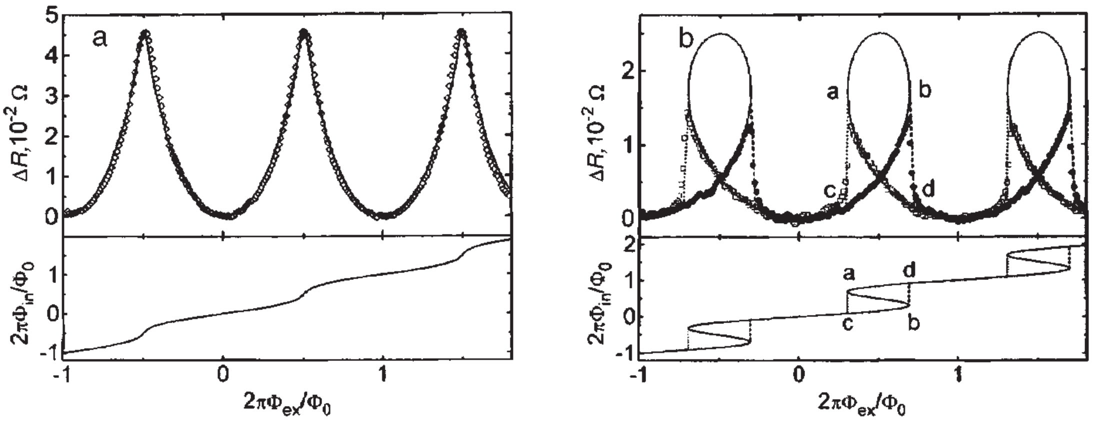

Figure 3.9: Left panel shows a sinusoidal line-shape which would be expected to have $\beta < 1$, this data is taken at $T = 3.75$ K. As the temperature is reduced to $T = 1.3$ K a hysteretic line-shape is observed corresponding to $\beta > 1$. The jumps in the resistance correspond with the unstable branches of the non-linear $\varphi(\varphi_{\text{ext}})$ dependence. Image taken from [62].

3.2.1 Control of the Screening Current with Bias Current

It has already been discussed that the critical current of a SNS junction can be varied by changing the temperature of the junction. It is also possible to change the critical current using a 'control current' applied perpendicularly to the junction as shown in Figure 3.10.

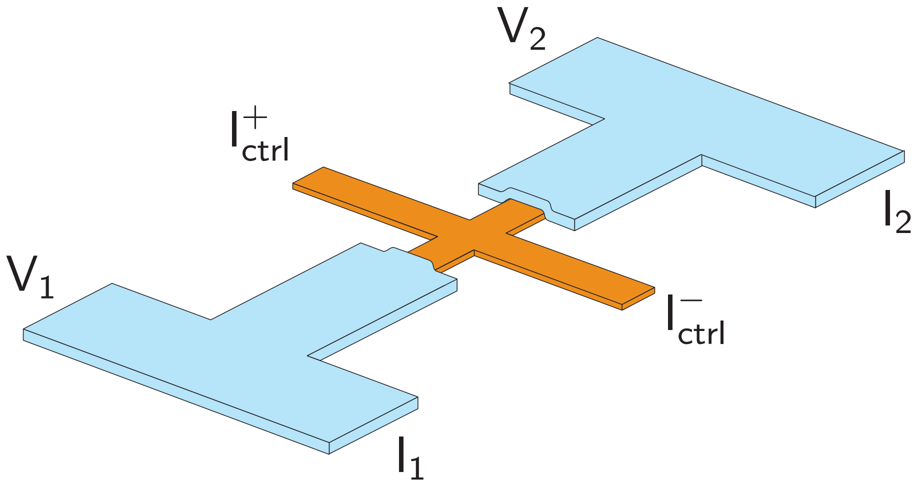

Figure 3.10: Schematic of SNS junction with normal control line attached. Normal metal is shown in orange, superconductor is shown in blue. A control current is driven through the normal metal part of the cross, perpendicular to the SNS junction.

As there is a finite voltage difference across the control line, the electrons in the control current have a higher energy than the electrons at equilibrium in the SNS junction. The excess of high energy electrons modifies the electronic distribution in the SNS junction. The occupation of bound states carrying current in opposite directions are equilibrated resulting in a reduction of the supercurrent magnitude [70]. A more in-depth discussion regarding the Andreev bound states and the effect of a non-equilibrium distribution function is described in the following paragraphs. When a quasiparticle is Andreev reflected at both NS interfaces an Andreev bound state is created. In essence a quasiparticle reflected at both NS interfaces can be considered as the transport of a Cooper pair between the superconducting electrodes. This means that the Andreev bound state contributes to the supercurrent across the junction. A discrete spectrum of bound states are formed at equally spaced energy levels up to Δ [71]. Each level can contribute to the current in a positive or negative direction. At $\varphi = 0$ the net supercurrent is zero; however, a phase difference results in a finite supercurrent determined by the contribution of each electron and hole component.

$$I_{\mathrm{s}} = \sum_{n=0}^{m} [I^{+}(E_n) f^{+}(E_n) + I^{-}(E_n) f^{-}(E_n)], \tag{3.23}$$

where $I^{-}(E_n)$ and $I^{+}(E_n)$ define the current contribution of the electron and the hole, which are of equal magnitude and opposite direction. f^{-} and f^{+} define the occupation probability of the state. Clearly the occupations can be defined as $f^{+}(E_n) + f^{-}(E_n) = 1$, and thus, $f^{+}(E_n) = 1 - f^{-}(E_n)$. Equation 3.23 can subsequently be expressed as,

$$I_{\mathrm{s}} = \sum_{n=0}^{m} I(E_n)[1 - 2f(E_n)]. \tag{3.24}$$

In the diffusive regime the discrete Andreev states are replaced with an energy dependent spectral current [72],

$$I_{\mathrm{s}} \propto \int_{-\infty}^{\infty} \Im(j_E)[1 - 2f(E)] \mathrm{d}E. \tag{3.25}$$

It is clear from Equations 3.23, 3.24 and 3.25 that the supercurrent is dependent on the occupation of the electronic states. Volkov [73] first proposed, in 1995, that the supercurrent in a SINIS junction could be changed by varying the distribution function of the wire, also suggesting that the SINIS may become a π-junction if the voltage exceeds a certain value. In 1998, Morpurgo *et al* [70] also claimed that the distribution function has an effect on the supercurrent in an SNS junction.

The distribution function of a mesoscopic normal metal wire is determined by the quasiparticle-quasiparticle interactions; this is the dominant inelastic scattering process occurring at low temperatures. Consider a mesoscopic normal wire between two bulk normal reservoirs. The steady state distribution function for this system is satisfied by the Boltzmann equation [74–76];

$$\frac{1}{\tau_{\mathrm{D}}} \frac{\partial^2 f(x,E)}{\partial x^2} + I_{\mathrm{coll}}(x, E\{f\}) = 0, \tag{3.26}$$

where x is the position along the wire, E is the energy, $\tau_{\mathrm{D}} = L^2/D$ defines the electron diffusion time, and I_{coll} is defined as the 'collision integral'. In the absence of electron-phonon scattering events, (i.e. $\tau_{\mathrm{ph}} > \tau_{\mathrm{D}}$) only electron-electron scattering processes are considered. Two possible scenarios can now occur depending on if electron-electron scattering can take place over the length of the wire or not. In the case that $\tau_{\mathrm{ee}} < \tau_{\mathrm{D}}$, electrons are able to interact with one another over the length of the wire and thus the distribution function is determined by these inelastic collisions. In this regime the distribution function is described by a typical Fermi function but with an elevated effective temperature,

$$T_{\mathrm{eff}} = \sqrt{T^2 + x(1-x)(aV)^2}, \tag{3.27}$$

where a is a constant, which at the centre of the wire is equal to $3.2\,\mathrm{K\,mV^{-1}}$. Morpurgo *et al* [77] show that as the voltage (and T_{eff}) is increased, the critical current through the SNS junction is reduced as shown in Figure 3.11.

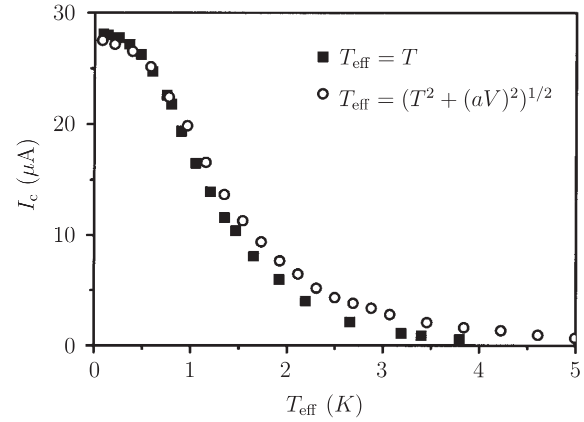

Figure 3.11: Critical current as a function of the effective temperature. The deviation between perfect agreement between the two is attributed by the authors to the non-negligible electron-phonon interaction above 1 K. Image taken from [77].

Let us now consider the second regime, where $\tau_{\rm ee} > \tau_{\rm D}$. In this case no electron-electron scattering takes place through the mesoscopic wire, which means $I_{\rm coll} = 0$. Therefore the Boltzmann equation can be solved as follows,

$$f_0(x, E) = (1 - x)\left(\frac{1}{1 + \exp[E/k_{\rm B}T]}\right) + x\left(\frac{1}{1 + \exp[(E + eV)/k_{\rm B}T]}\right). \qquad (3.28)$$

The form of the solution taken at an equal distance between the two reservoirs biased at $\pm V$ is given as,

$$f(E) = \frac{1}{2}\left(\frac{1}{1 + \exp[(E + eV)/k_{\rm B}T]} + \frac{1}{1 + \exp[(E - eV)/k_{\rm B}T]}\right). \qquad (3.29)$$

The distribution function $f(E)$ is effectively describing the superposition of two Fermi-Dirac distributions, one from the reservoir biased at $+V$, and one from the reservoir biased at $-V$. This manifests as a double-step feature in the distribution function of the normal wire.

3.2.2 Experimental Observations of π-states

The following discussion describes what happens to the observable supercurrent when the non-equilibrium double-step distribution function is controlled. As the control voltage is increased, the width of the double-step function also increases. An increasing number of states are thus excluded from the contribution to the supercurrent as the control voltage is increased. Figure 3.12 shows the theoretical plot by Heikkilä [78]. The black line represents the spectrum of supercurrent states, whilst the solid blue line shows a typical double-step distribution function. By integrating this function it is clear that the states corresponding to $f(E) = 0$ are excluded from contributing to the observable supercurrent. The supercurrent is reduced to zero when the contribution of positive and negative supercurrent-carrying states are equalised. Increasing the control voltage further results in an interesting case whereby all the positive supercurrent-carrying states are excluded and only negative states contribute to the observable supercurrent. At this point, the Josephson current-phase relation changes from $I_\mathrm{s} = I_\mathrm{c} \sin\phi$ to $I_\mathrm{s} = I_\mathrm{c} \sin(\phi + \pi)$ with the supercurrent now exhibiting π-junction behaviour.

Baselmans *et al* [79] (see also later work in Ref [80]) were the first group to experimentally observe π-junction behaviour as shown in Figure 3.13. They fabricated a Nb-Au-Nb SNS junction with a perpendicularly attached gold control line. In order to create the desired step-like distribution function, the control line was connected at either end to 'bulk' ($475\,\mu$m thick) gold reservoirs which were biased with a voltage difference, V.

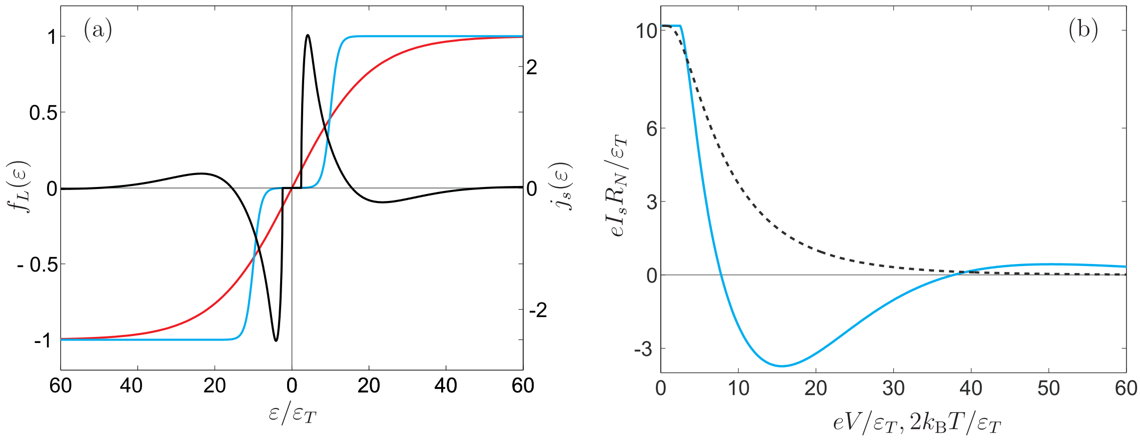

Figure 3.12: (a) shows the spectrum of supercurrent-carrying states (black, right axis). The occupation number of correlated pairs is also shown (left-axis). Both an equilibrium distribution (red) and a non-equlibrium double-step distribution (blue) are shown. (b) shows the voltage dependence of the supercurrent (blue). The temperature dependence of the supercurrent is also shown (dashed). Image edited from [78].

Experimentally, upon an increase of the control voltage a suppression and re-emergence of the critical current was observed. This is because it is the magnitude of the supercurrent that is actually measured. In order to show that the system does indeed enter the π-state, Baselmans *et al* also measured the phase dependent resistance, ΔR, at control voltages corresponding to the two different states. Figure 3.13 (e) shows that the phase of the system does change and proves that the π-state was observed.

Shaikhaidarov *et al* [81] reproduced the π-effect experiment in a similar geometry to Baselmans *et al*. In addition, they showed that it was possible to observe the π-effect with no current being driven through one of the SN interfaces - the so called 'dangling arm' experiment. Huang *et al* [82] fabricated a similar device to that measured by Shaikhaidarov, this time omitting one of the normal reservoirs entirely, resulting in a three terminal device. Again the π-junction behaviour was observed.

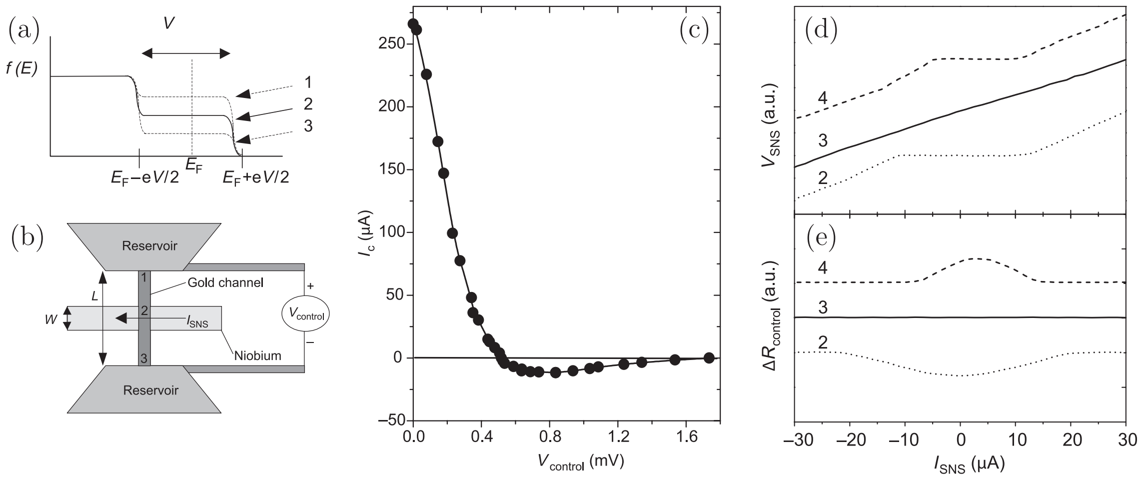

Figure 3.13: Highlights of the experiment by Baselmans *et al.* (a) gives an example of the double-step distribution function. (b) shows the sample geometry with the SNS junction with a gold control line attached perpendicularly to the centre of the SNS. Note that the points 1,2 and 3 correspond to the different distribution functions. (c) is the measurement of the critical current as a function of the control voltage It is clear that as the control voltage is increased the critical current through the SNS junction is reduced. The critical voltage is reached at approximately 0.52 meV at which point the system enters the π-state. (d) shows the I-V curves at three different control voltages. (e) shows the change of sign of the control line subject to the same three control voltages. The change of sign of ΔR is considered proof that the system enters the π-state. Image edited from [79].

3.3 Hybrid Quantum Interference Devices and Applications

Having gone through some of the basic physics behind the interferometer and its properties, it is interesting to have a look at some of the applications these types of devices have been used for. Clearly the device shares many similarities with SQUIDs; in fact, a number of experiments have been performed using a HyQUID instead. It is known that superconducting circuits interrupted by Josephson junctions can contain a persistent current, which can flow either clockwise or counter-clockwise providing two qubit states [83]. Qubits are the building blocks of quantum computing, and superconducting circuits are one of the proposed systems that have received a lot of attention in recent years. Spectroscopy of a persistent current qubit was performed by Chiorescu *et al* [84] using a galvanically coupled SQUID circuit. In 2005, Petrashov *et al* combined the Andreev interferometer loop with a four-junction Josephson circuit (see Figure 3.14) in order to probe the persistent current states of the quantum circuit [85]. They were able to perform a continuous readout of the ground state. Full details of the experiment can be found in Refs [86, 87].

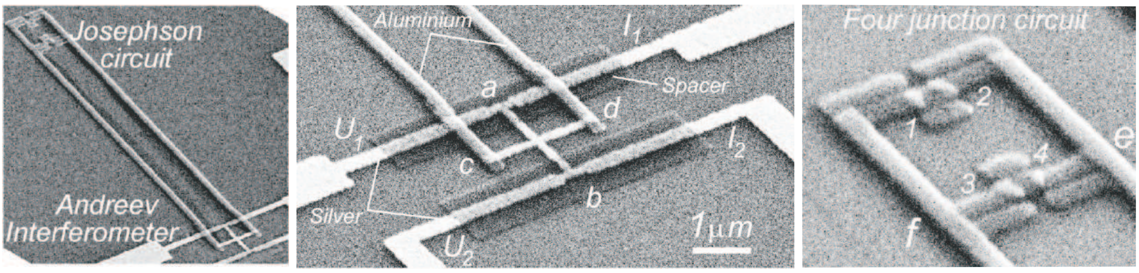

Figure 3.14: SEM images of the device made by Petrashov *et al* [85]. (left) shows the main superconducting loop connected to the Andreev interferometer and the four-junction Josephson circuit. (middle) shows the typical interferometer - there is a phase difference between c and d which is determined by measuring the oscillating resistance across a and b. (right) shows a higher magnification image of the Josephson circuit.

More recently the HyQUID has been adapted to incorporate a ferromagnetic disc into the device with the hope of seeing effects of the long range triplet in superconductors [88,89]. In 2010, Giazotto *et al* [90] presented a very similar device called the superconducting quantum interference proximity transistor (SQUIPT) comprised of a superconducting loop interrupted by a normal metal. The device also showed the typical periodic magnetoresistance oscillations as shown in Figure 3.15 (b). An important figure of merit that the authors measure and discuss is the ‘flux-to-voltage transfer function’ (shown in Figure 3.15 (c)).

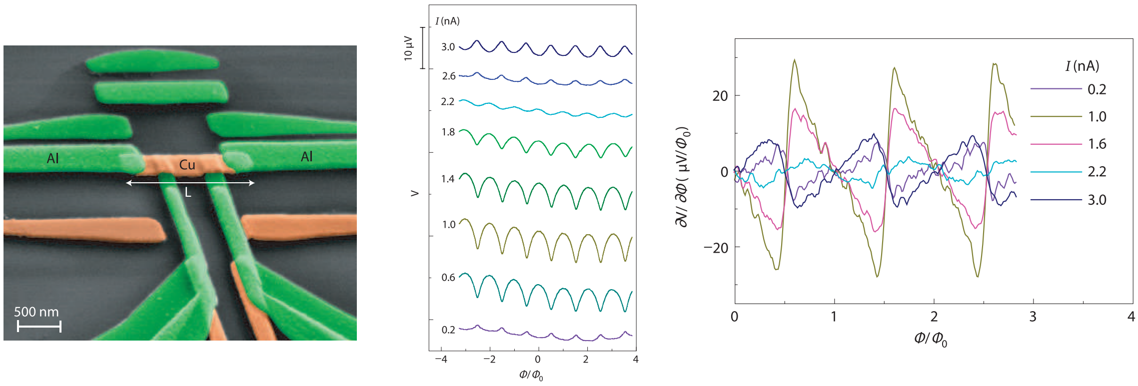

Figure 3.15: (left) SEM image showing SNS contact of device using Al for superconductor and Cu for the normal metal. Interferometer attached to superconducting loop not shown. (center) Magnetoresistance oscillations taken at different bias currents. (right) Flux-to-voltage transfer function $\partial V/\partial\Phi$ at different bias currents. Image edited from Giazotto *et al* [90].

3.4 Summary

In this chapter, the physics of Andreev reflection and the proximity effect has been introduced. A number of important length and energy-scales are discussed which lead to the phase-periodic electron transport across a normal metal junction between two superconductors. A number of early experiments are discussed, particularly those which demonstrated control of the phase-periodic oscillations by means of either an externally applied magnetic flux or current. The possibility of metastable states existing in hybrid interferometers are discussed by modelling the system as an rf-SQUID. The metastable states occur when the screening parameter $\beta \approx \mathcal{L}I_{\mathrm{c}} > 1$. As the value of β can be varied by changing the critical current of the junction, experiments exhibiting direct control over the critical current with a control current are discussed. Further control of the supercurrent has been shown during the discussion of previous experiments in which a π-state is observed. Finally, a few examples of hybrid interferometers which have been used experimentally as read-out devices are highlighted.

CHAPTER 4

Design and Fabrication of Hybrid Nanostructures

All the samples made during this work use a positive resist lithography process. A simplified overview of the whole process is explained here and depicted in Figure 4.1. The first step of any pattern transfer process is the spin coating of a resist. The resist is a polymer that is sensitive to exposure to light or electrons, causing the structure to change. In the case of a *positive resist* the structure of the resist is weakened by scission of the polymer chains [91]. The resist is typically applied to the substrate using a spin coating process. The wafer is held in place by a vacuum plate and the liquid resist is dispensed on to it. The spin coater is then accelerated to a ‘low’ speed of around 500 rpm before accelerating to a pre-programmed ‘high’ speed which determines the final resist film thickness. Once the spin programme is finished it is necessary to bake the wafer on a hot plate in order to remove any remaining solvents.

In order to transfer a pattern to the resist, one must perform the lithography process. Optical (or photo-) lithography is performed by exposing the resist to a UV light source. The resist is covered with a quartz mask containing a printed chromium pattern. The UV light is able to penetrate the quartz but is blocked by the chromium pattern resulting in an inverse of the mask pattern being transferred to the resist.

Photo-lithography is able to expose large areas of substrates quickly and easily making it ideal for patterning of whole wafers. The main disadvantage of photo-lithography is that the minimum feature size is ultimately diffraction limited to a few hundred nanometers [92]. An alternative lithography method for small features sizes is electron beam lithography. Unlike photo-lithography, where the UV floods the entire area and must be blocked by a physical mask, the electron beam is guided over the resist and thus 'writes' the pattern.

The weakened areas of resist are removed using a developer solution. The bare substrate is left in the areas that were exposed during the lithography process. It should be noted that a two-level resist profile is used - the bottom layer of resist is chosen to develop more quickly that the top layer. This results in a well defined pattern on the top resist which determines the geometry of the deposited film. The bottom layer is developed to a greater extent forming an *undercut* which greatly aids a clean lift-off. The development process is typically not perfect, and some resist residual may be left behind which can affect the quality of the deposited film. The residual resist is removed by bombardment of either argon or oxygen plasma. This process is known as plasma etching. Argon is an inert gas, and thus the etching is an entirely mechanical process (ion milling). When oxygen gas is used there is also a reactive ion etch taking place.

Once the residual resist is removed and the exposed substrate is clean, thin film deposition can take place. A thermal evaporation technique is used in this work utilising the Edwards 306 Coating System. This is a thermal evaporation system in which materials can be deposited in a low pressure environment. The deposition process takes place in a bell jar evacuated to low pressures using two-stage pumping system. Initial evaporation down to approximately 200 mbar is performed by a rotary pump before switching to a diffusion pump to achieve a base pressure of around 2×10^{-6} mbar. It is necessary to achieve sufficient vacuum to ensure the source-to-wafer distance is less than the mean free path of the source particles [91]. If the vacuum is insufficient the source particles will be scattered by any residual gases in the chamber.

The source material is placed on a tungsten boat held between two electrodes. A current is passed though the highly resistive boat which heats the material to a high enough temperature to allow evaporation to take place. The material is deposited on the sample (both resist and exposed substrate).

To reveal the final patterned sample the remaining resist must be removed - this is the *lift-off* process. The sample is placed into a lift-off remover solution (and sometimes heated) which removes of the remaining resist and any deposited material on top of the resist and walls. This reveals only the desired pattern still adhered to the substrate. It has been necessary throughout this project to process bare silicon oxide wafers into usable chips. Once the chips are fabricated the nano-structure devices are fabricated onto the chips. These two separate processes follow the fabrication stages discussed above and shown in Figure 4.1. Some of the specifics are discussed in more detail in the following two sections.

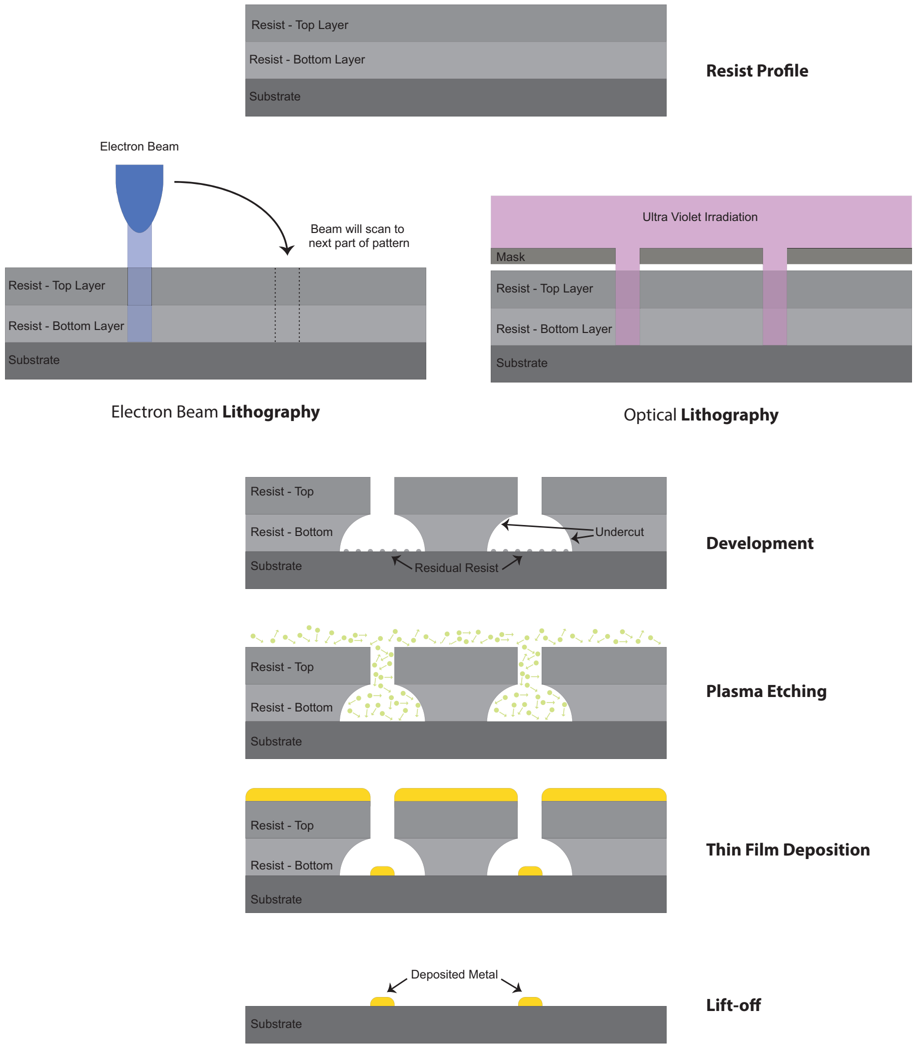

Figure 4.1: Overview of fabrication process: The *resist profile* is created by spinning two different resists onto the substrate. The *lithography* is performed using either a focussed electron beam which 'writes' the pattern into the resist, or a mask in conjunction with ultra violet irradiation which transfers the whole pattern at once. *Development* of the resist results in the weakened areas of resist being washed away revealing the desired pattern. Some residual resist may be left on the substrate which is removed using a *plasma etching* process. Once the substrate is clean, *thin film deposition* is performed to evaporate a thin film of the chosen metal onto the substrate. The remaining resist and unwanted metal is removed during *lift-off* leaving material in the desired pattern.

4.1 Wafer Processing and Chip Preparation

In order to connect the devices to electronic measuring equipment, a standardised chip was used. The chips are made on a 3 inch SiO wafer, each with 7 × 7 mm dimensions. Each chip contains 16 gold contact pads with leads converging to a 80 × 80 μm exposure field as shown in Figure 4.2. The gold contacts allow the samples to be connected to the measuring set-ups using either pogo-pins or wire bonding. In order to ensure that the resist is applied onto a good surface it is important that the wafer is thoroughly cleaned. Dust and other large particulates can be removed by submerging the wafer in acetone in an ultrasonic bath. The acetone wash is followed by rinsing in isopropanol to remove any acetone film left behind. Any remaining organic matter is removed using an oxygen plasma etch.

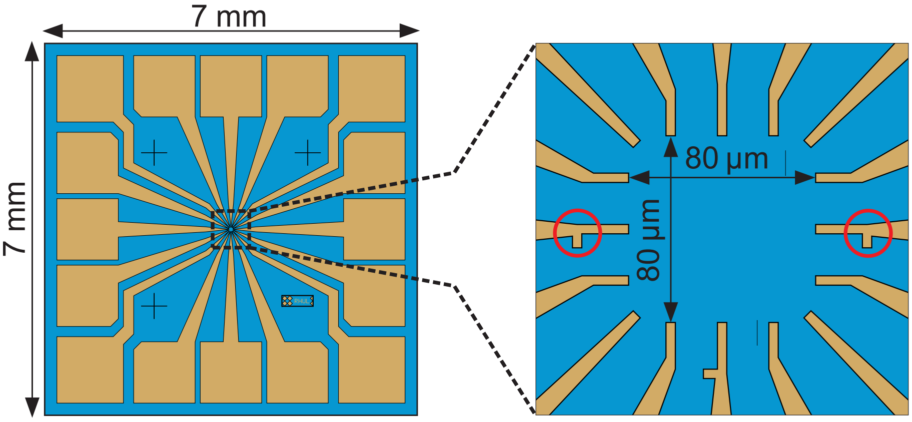

Figure 4.2: Single 7 × 7 mm silicon chip after deposition of gold contact pads and leads. Zoomed-in section shows the 80 × 80 μm exposure field where electron beam lithography takes place. Red circles highlight distinctive features known as 'marks'. The marks are used to allow the SEM to correctly align the first exposure.

4.1.1 Resist Deposition

The resist profile used for photo-lithography of the wafers is a typical two-resist system: First a layer of LOR-5B is deposited at 3000 rpm followed by baking for 5 minutes at 150 °C, resulting in a film thickness of approximately 500 nm. Next, a photoresist, S1813, is deposited and spun at 4500 rpm prior to baking for 5 minutes at 90 °C to form the top layer of 120 nm thickness.

4.1.2 Photo-lithography and Development

The photo-lithography step is performed in an enclosed box with a mercury ultra-violet light source. The wafer is typically exposed for 2 minutes although the exact time depends on the light emittance measured prior to exposure. Once the exposure is complete the weakened resist is removed by placing the wafer in Microposit Developer MF319 - again the times are variable but typically 90 seconds is sufficient. Any residual resist is removed by performing a 30 second oxygen etch using the Oxford Plasmalab 80.

4.1.3 Thin-Film Deposition of Contact Pads and Leads

The whole wafer is secured to a plate which faces the source material. Gold is the material that is used for the sample contact pads and leads on the generic chip design. However, as gold is a low reactivity metal it is necessary to deposit a thin (10 nm) layer of nichrome as an adhesion promoter prior to the gold deposition [93]. The evaporation system contains three electrodes which allows deposition of up to two different materials without breaking vacuum. Once the nichrome layer is deposited, 80 nm of 99.9999 % purity gold is then deposited on top.

4.1.4 Lift-off

With a layer of nichrome and gold deposited on the entire wafer it is necessary to remove the remaining resist and excess metal, leaving only the desired chip pattern remaining. The wafer is placed into Microposit Remover 1165 and heated to 60 °C on the hot plate. Once the pattern is revealed the wafer is rinsed in isopropanol and dried with a nitrogen gun prior to observation under the optical microscope to check for any unremoved material or defects. The completed wafer is then coated in a protective layer of resist and then cut into individual chips using a diamond wafer cutter. The chips are then ready for device fabrication.

4.2 Device Fabrication

As mentioned in the general overview, optical lithography is diffraction limited - this restricts its use to rather large scale structures. For the devices measured in this work it is necessary to utilise electron-beam lithography for smaller structures. Apart from the chip production all other lithography performed was e-beam lithography. Prior to electron beam lithography, the chips must be coated in electron-beam sensitive resists. During the course of this work a number of different resist profiles were used but typically a two layer resist profile was necessary to provide the undercut properties previously discussed. Most commonly the bilayer was made with a bottom resist of Copolymer 6 % in Ethyl Lactate and a top layer of PMMA (2, 4, 6 or 9 %) in Anisole.

4.2.1 Electron Beam Lithography

The e-beam lithography system used during this work is a JEOL JSM-6460 Scanning Electron Microscope (SEM) with the addition of the NanoMaker software package that allows control of the beam for patterning. The SEM provides a focused beam of electrons that are incident on the electron sensitive resist, which, similarly to the photo-lithography process, weakens it making it more susceptible to removal by a developer solution. It is also possible, through overexposure of the resist, to harden the exposed areas through a cross-linking process [91]. This would be classified as a negative process and is not used in this work - over exposure is thus avoided in this work. One cause of over exposure is the failure to account for the proximity effect. Electrons incident on the resist and substrate undergo scattering processes leading to energy losses and changes of direction. The electrons will travel through the resist until either all energy is dissipated, or they are backscattered out of the resist. Figure 4.3 shows simulations of the energy dissipation of electrons incident on a layer of PMMA and silicon substrate, at different accelerating voltages. Larger and closely spaced features will have a large energy density deposited in the film due to superposition of backscattered electrons [94].

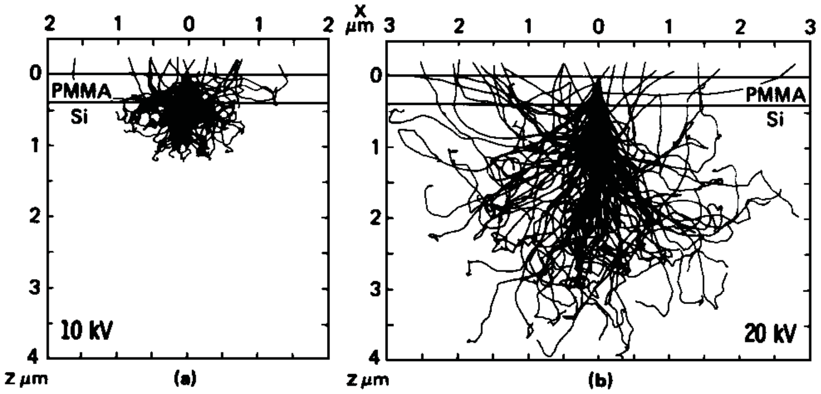

Figure 4.3: Monte Carlo simulations of energy dissipation of electrons incident on a silicon substrate with a layer of PMMA resist. Simulations are performed for accelerating voltages of 10 kV and 20 kV. It can be seen that the spread of scattered electrons within the resist is reduced at the higher accelerating voltage. Image taken from [94].

This problem is overcome through use of a proximity correction calculation. The proximity correction spatially shapes the dose incident on the resist to compensate for the backscattered electrons. An example of a design file after proximity correction has been applied is shown in Figure 4.4. The larger structures have a reduced applied dose at their centers - this is to reduce the total received dose so that the shape is formed as desired. Fine features such as the Andreev cross and marks are given a flat rate - this is to avoid them being broken up into smaller components which could lead to problems due to misalignment because of the stitching of the different pieces.

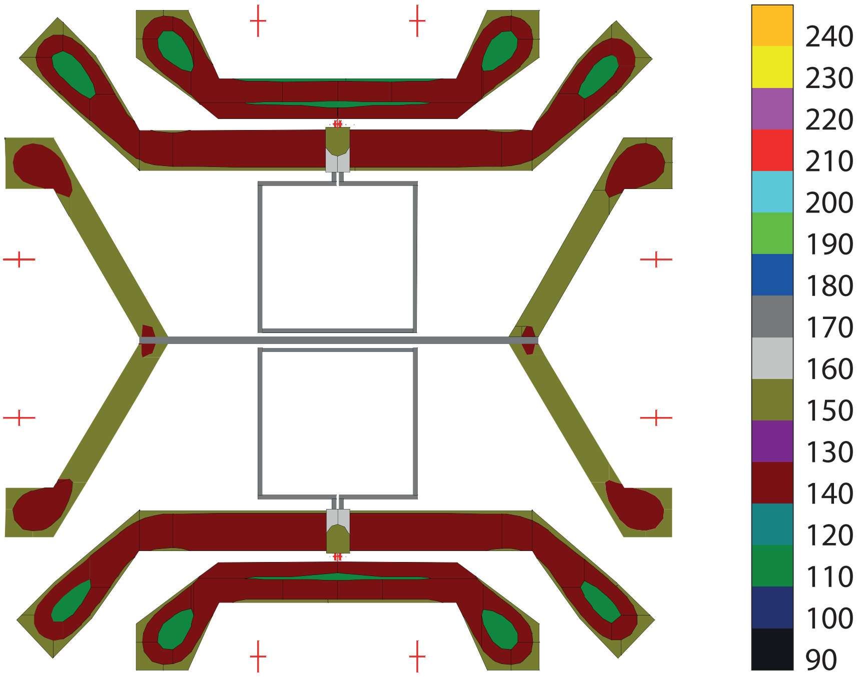

Figure 4.4: Example of a proximity corrected sample design. Note that the large parts of the design have a smaller dose at the center to reduce the total dose received. Small features receive a user defined flat dose to avoid splitting fine elements into many pieces. The colour key gives the relative dose values.

4.2.2 Thin Film Deposition of Devices

Deposition of the materials for the devices also takes place in the Edwards Coating system. The system has additional functionality for the actual device fabrication. Two 7 mm samples can be mounted on a rotating platform which allows multiple angle depositions (useful for Josephson junctions or multiple material devices to be fabricated without breaking vacuum). The sample holder is situated approximately 20 cm from the source electrodes. Another use for the rotating sample holder is that the chips can face the source material for deposition or can be turned 180° to face into a small glass chamber. The chamber is connected to a gas line and can be filled with either argon or oxygen at a controllable pressure or flow. The samples are subjected to a 20 second in-situ argon etch prior to deposition without breaking vacuum in order to clean any residual resist from the substrate. The oxygen gas can be used to grow insulating aluminium-oxide tunnel barriers in traditional SIS Josephson junction fabrication. Lift-off is performed as described in Section 4.1.4 revealing the desired pattern. The chip is cleaned and is then ready for measuring or further layers of material deposition.

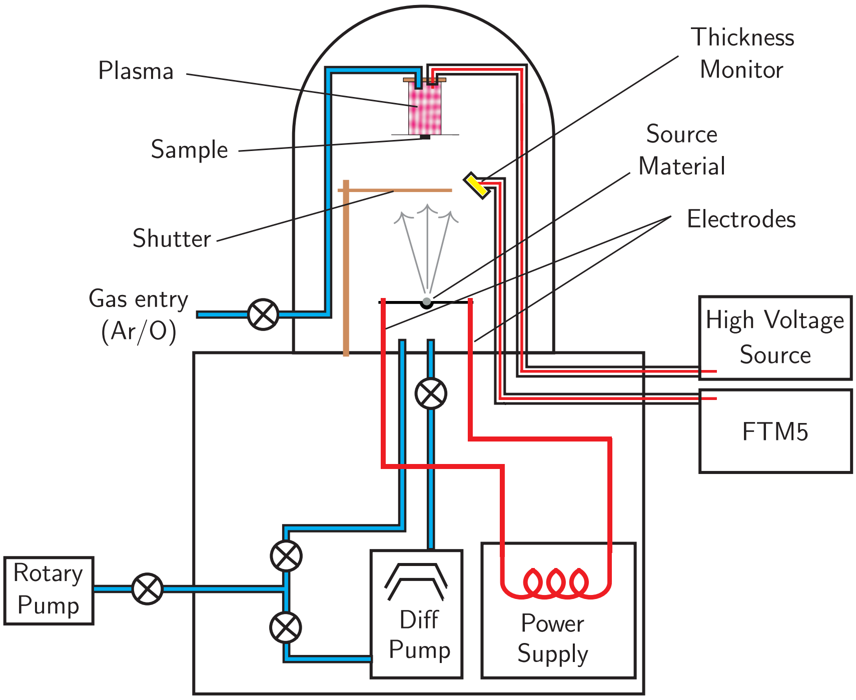

Figure 4.5: Simplified schematic of the Edwards 306 Coating System.

4.3 Summary

In this chapter, an overview of all the techniques required for fabrication of the devices is shown. The patterning of gold contact pads and leads onto bare silicon wafers to create the ‘blank chips’ is highlighted in the first part of this chapter. The latter half of this chapter goes into more detail regarding the nano-fabrication techniques required to make accurate multi-layer devices. A brief discussion of the proximity effect which occurs when using electron-beam lithography is presented. A solution to this problem using proximity correction software is also shown.

CHAPTER 5

Experimental Setup and Low-Temperature Equipment

All of the experiments presented in this thesis use materials that exhibit the phenomenon of superconductivity. In order to observe the interesting behaviour that appears in the superconducting phase the samples must be cooled to below their superconducting transition temperature, T_c. Two different cryostats have been used throughout this work, a Heliox ^{3}He cryostat with a base temperature of 240 mK, and a dilution refrigerator with a base temperature of approximately 20 mK.

5.1 Heliox Top-Loading ^{3}He Cryostat

The majority of the samples presented in this thesis were measured in the Heliox top-loading ^{3}He cryostat. The base temperature of 240 mK is well below the T_c of aluminium ($\sim$ 1.2 K) which was the superconductor most commonly used during this work. The cryostat comprises of two main vacuum chambers, the outer vacuum can (OVC) and the inner vacuum can (IVC). The space between the OVC and the IVC is known as the main bath and is filled with liquid ^{4}He which is at a temperature of approximately 4.2 K. The main bath is used to reduce the heat load of the surroundings on the components inside the IVC. A smaller vessel located inside the IVC also contains liquid ^{4}He that is constantly filled from the main bath - this is known as the 1 K pot. By pumping on the ^{4}He in the pot with a rotary pump the vapour pressure is reduced and evaporative cooling can occur. This allows the pot to cool to approximately 1.4 K [95]. The next drop in temperature comes with the use of ^{3}He which is condensed whilst flowing through pipes in contact with the 1 K pot before filling the sample space. The liquid ^{3}He is cooled further through use of a charcoal sorption pump. The sorption pump absorbs gas when cooled below 40 K increasing the rate of evaporation and thus reducing temperature of the ^{3}He sample space to approximately 240 mK.

The system is inherently single-shot due to the finite capacity of the sorb to pump the helium gas. Once the sorb is full, the cycle can restart by heating the sorb to 45 K causing re-condensation of the helium. The amount of time for measurements in between each re-condensation cycle was approximately 36 hours. The sorb is also used to control the temperature of the sample space. Directly applying heat to the helium results in a greatly increased evaporation rate and thus shorter lifetime of the cycle. Instead the sorb is heated, which controls the pressure of the ^{3}He vapour and thus its temperature [96]. This allows stable control of the temperature in order to investigate the temperature dependent properties of samples, typically in the range of 0.25 to 1.4 K.

The Heliox cryostat is a top-loading design; this means that the measurement probe is mounted at room temperature and then lowered into the bottom of the fridge. The probe has a maximum capacity of four 16-pad samples which are contacted using a spring-loaded pogo-pin mechanism. As the sample holder is screwed onto the bottom of the probe the sample pads make contact with the pogo-pins. The spring-loaded pins push back at the sample ensuring good contact between probe and device even in the case that the metal contracts due to the change in temperatures. The pogo pins are connected to 16-way Fischer connectors at the top of the probe with constantan twisted pairs.

5.2 Dilution Refrigerator

For some of the samples measured in this thesis a dilution fridge was used in order to enter the sub-50 mK range. The principle of the dilution refrigerator was first proposed by London, Clarke and Mendoza in 1962 [97] based on London's earlier suggestion in 1951 that cooling could be achieved by making use of the entropy of mixing of ^{3}He and ^{4}He [98]. The first experimental realisations of the dilution fridge occured concurrently in Manchester, by Hall *et al* [99], and in Dubna, by Neganov *et al* [100], both claiming a base temperature of approximately 25 mK.

The main cooling process of the dilution fridge takes place in the mixing chamber where a mixture of ^{3}He and ^{4}He separate into a concentrated phase (^{3}He rich) and a dilute phase (^{4}He rich). The separation of the two phases occurs at approximately 0.7 K. As the mixture is cooled further the top concentrated phase tends to 100 % of ^{3}He whilst the dilute phase tends to 6.6 % of ^{3}He. This limit of 6.6 % in the dilute phase is maintained even as $T \rightarrow 0$. The ^{3}He is pumped from the dilute phase in the still (see Figure 5.1). In order to maintain the 6.6 % concentration in the dilute phase, ^{3}He is evaporated across the phase boundary from the concentrated phase. The cooling occurs due to this evaporation across the phase boundary. Unlike the Heliox ^{3}He cryostat discussed in Section 5.1, the dilution refrigerator is able to run continuously if the pumped ^{3}He gas from the dilute phase is cooled and returned to the concentrated phase.

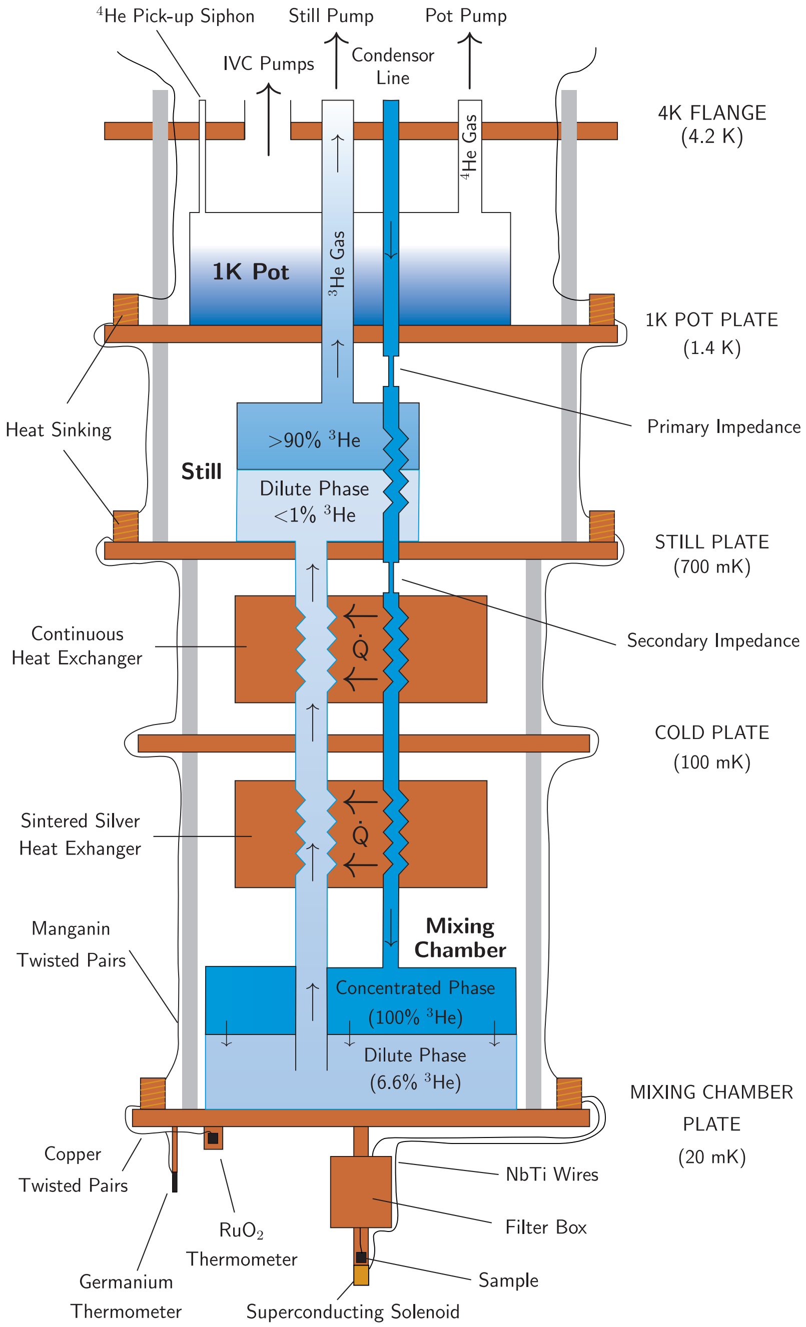

Figure 5.1: Schematic of the ^{3}He-^{4}He dilution fridge

5.2.1 Thermometry and Filtering

Of utmost importance to all low temperature work is the ability to accurately determine the temperature. Initially, the fridge was equipped with three thermometers;

- Rhodium Iron (RhFe) - calibrated between 1.4 - 300 K
- Carbon Glass
- Cerium Magnesium Nitrate (CMN)

Unfortunately, the CMN thermometer was not functioning, most likely due to a faulty circuit. Instead a RuO_2 surface mount resistor was mounted to the mixing chamber. The initial cooldown of the cryostat resulted in a base temperature of 300 mK, clearly this is comparable to the Heliox ^{3}He cryostat and unacceptable for a dilution unit.

The poor base temperature achieved was attributed to either heat leaks (including insufficient filtering) or faulty thermometry. Due to time constraints all possible problems were tackled prior to the next cool-down.

A large possible heat leak was found in the form of a microwave guide travelling from room temperature down to the mixing chamber (this was used on a previous experiment by another group). The microwave guide was removed and the holes remaining at each stage were plugged to stop photons from hot parts of the fridge travelling down to the mixing chamber and sample holder.

Additional thermometry was acquired and added to the mixing chamber. A germanium resistance thermometer already attached to its own copper post was screwed directly into the mixing chamber. The Ge thermometer was previously used on the fridge and detailed records were kept of its use in parallel with that of the old working CMN thermometer so it was possible to be confident of its temperature reading down to approximately 50 mK. The previous RuO_2 thermometer was discarded and replaced by four more from a single batch of resistors - one of the batch, not used, was calibrated against a ^{3}He melting curve thermometer [101] with all remaining tested thermometers behaving similarly [102].

With regard to filtering, two possible filters were considered to reduce high amplitude noise reaching the devices causing local heating. TUSONIX π-filters are a cheap commercial L-C low-pass filter and although showing adequate attenuation characteristics (see Figure 5.2). It was decided to not use them due to experiencing poor results from thermal cycling [103].

The second type of filter investigated are the copper powder filters first developed by Martinis *et al* [104] in 1987. The filters discussed here follow the improved design proposed by Lukashenko *et al* [105]. The concept of operation of these filters is that the measurement lines are in close contact with a fine copper powder. High frequency components are then dissipated in the powder in the form of eddy currents. Due to the large surface area of the powder the damping of the high frequency components can be quite considerable. An outline of the filter design is summarised here (see also Figure 5.3 (a)). The copper powder is mixed with epoxy so that epoxy/Cu rods can be machined. The measurement wire is wrapped tightly around the rod terminated by an MCX connector at both ends (Each MCX connector is also soldered to a discoidal capacitor to provide some low-frequency cut-off). The entire assembly is then inserted into a cylindrical copper shield and filled with more epoxy/Cu mixture.

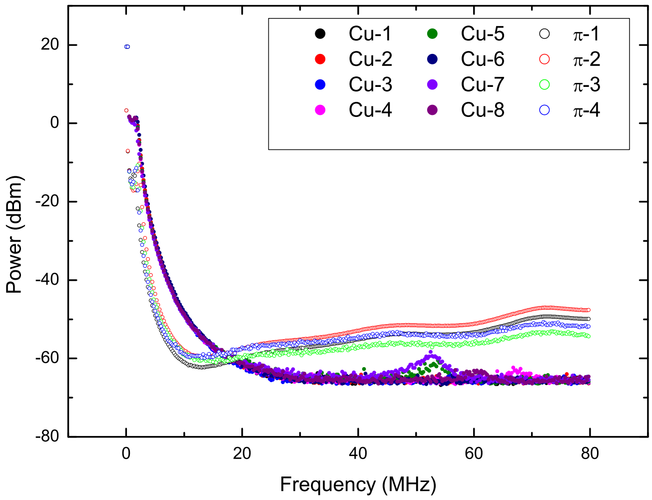

Figure 5.2: Comparison of the TUSONIX π-filters and the copper powder filters. Both have similar transmission properties however copper powder filters were chosen for their reproducibility following thermal cycling [103].

A large batch of Cu-powder filters made by Dr. Chris Checkley were obtained and tested. Figure 5.2 shows the reproducible transmission characteristics of the filters. It was also known that the filters held up well under thermal cycling having been used on another experimental set-up [106, 107] so these were chosen to be installed on the dilution fridge. Once the measurement lines have been filtered it is necessary for the wires to be shielded. For this reason a 'horseshoe' type filter mount was made by Massimo Venti with a cinch connector to attach to the sample holder. The sample holder was also made by Massimo Venti for the experiment discussed in [106], see Figure 5.3 holder for photographs of both filter and sample holder.

Once the changes discussed above were made it was possible to cool-down the cryostat again. The Ge resistance thermometer indicated that temperatures below 50 mK were obtained. The surface mount RuO_2 resistance thermometers showed that the base temperature of the fridge reached approximately 16 mK.

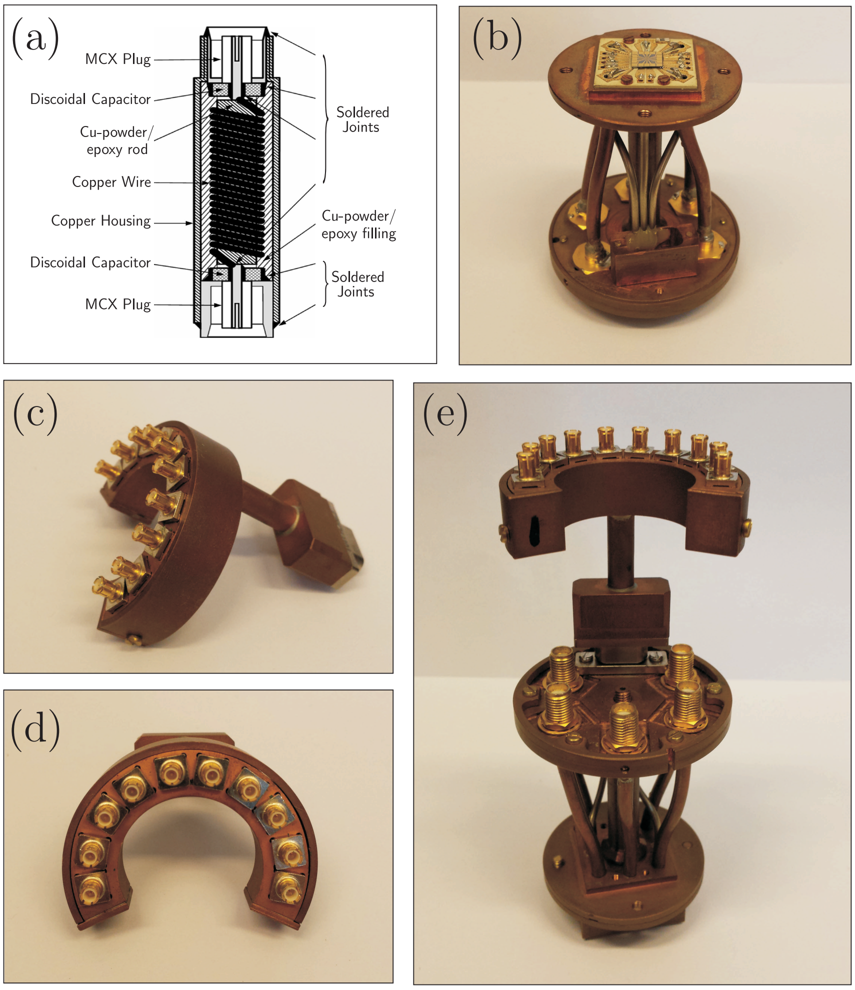

Figure 5.3: (a) Schematic of copper powder filters. Image edited from [105] (b) Copper sample holder used for dilution fridge measurements - was made for previous experiments detailed in [106]. (c) and (d) show the copper powder filter mount to allow filtering between mixing chamber stage and sample holder. (e) Filter mount connected to sample holder.

5.2.2 Wiring and Magnetic Field Control

Unlike the Heliox ^{3}He cryostat, the dilution refrigerator was not set up for any transport measurements. All measurement lines had to be installed from the 1 K plate down the mixing chamber and subsequently, the sample holder. For the main sample, 16 manganin wires, in 8 twisted pairs were made and attached to the 1 K plate. The lines were thermally anchored at each plate (still, cold and mixing chamber) by winding around a copper pillar and securing with GE varnish. The manganin twisted pairs were terminated at a cinch connector. The other side of the cinch connector had copper lines, thermally anchored to the mixing chamber plate, that were wired into the Cu-powder filters, ultimately terminating at the sample holder PCB.

Magnetic field control was provided by a small superconducting solenoid. The coil was made by winding superconducting NbTi wire around a small epoxy/Cu cylinder. The superconducting wire was run inside existing coaxial ports up to the top of the fridge.

The thermometer lines were installed similarly to the sample measurement lines - manganin twisted pairs thermally anchored at each plate until converting to copper lines thermally anchored at the plate of interest.

5.3 Electrical Measurement Technique

In order to measure the resistance of the devices, conventional 4-terminal transport measurements were undertaken. A Signal Recovery 7621 Lock-in Amplifier was used to provide the ac signal to the device. To allow for differential resistance measurements or any measurements with a dc offset an adder was used to combine the ac and dc signals. This combined signal is connected to a bias resistor (typically R_{bias}=100 kΩ) to drive a current (μA range) through the device. Voltage probes are connected to the device and fed to a pre-amplifier (×100 gain) before being passed to the lock-in amplifier. The lock-in amplifier compares the measured signal with that of the reference signal, any signal from frequencies other than the reference frequency are reduced close to zero thereby considerably reducing the noise in the measurement. Typically, frequencies are chosen to avoid large sources of noise in a lab environment (i.e. 50 Hz mains hum), the value used throughout this work is 187 Hz. The dc current is provided by a Yokogawa 7651 DC Current Source. The adder and pre-amplifier are powered by battery packs to further reduce mains noise in the measurement set up. The measured voltage is then recorded on a PC after phase detection from the lock-in.

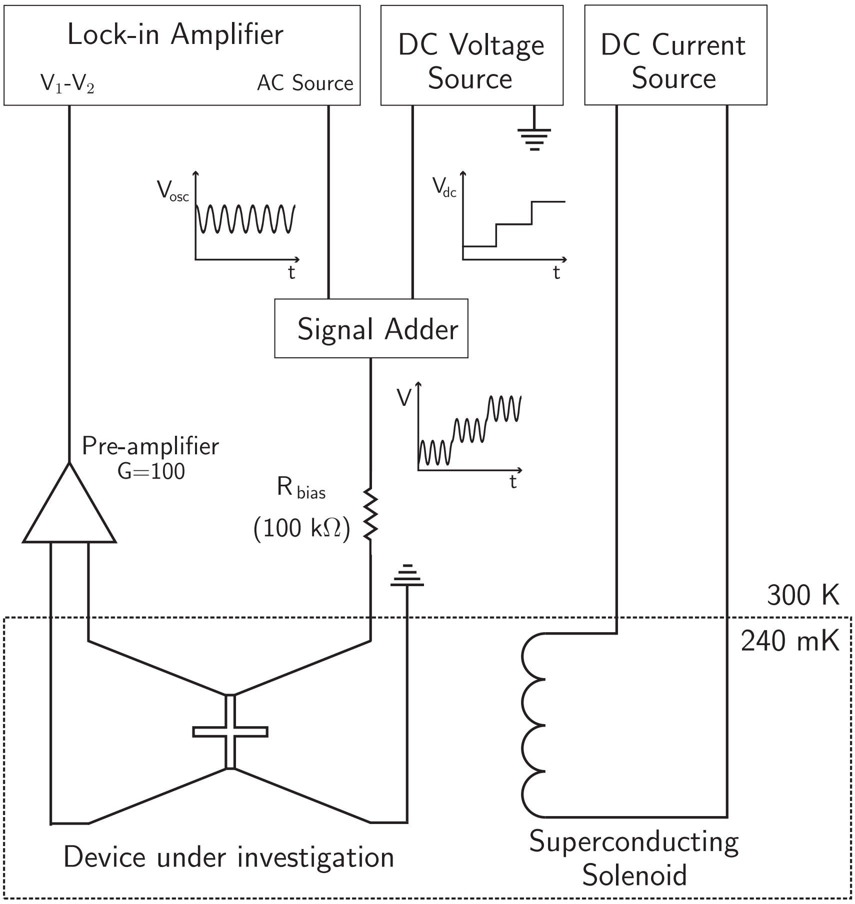

Figure 5.4: Simplified schematic of the typical measuring set-up. Differential resistance measurements are achieved using a 4-point measurement technique as shown. The ac source is provided by the lock-in amplifier and added to a variable dc source. The resulting signal is an oscillating part on top of a stepped dc signal. Magnetoresistance measurements are performed by measuring the resistance whilst sweeping the magnetic flux using either an on-chip flux source or a superconducting solenoid.

5.4 Summary

This chapter discusses the experimental set-up used throughout the work presented in this thesis. Two separate cryostats are discussed; a pumped ^{3}He system and a dilution fridge. The working principles behind both systems are explained. The pumped ^{3}He system was set-up for use prior to the start of this work and needed no further engineering. The dilution fridge, on the other hand, required full re-wiring, thermometry installation and filtering. The work done to prepare the dilution fridge for device measurement is discussed in some detail. The conventional 4-point transport measurement technique is also explained.

CHAPTER 6

Optimisations of the Hybrid Interferometer for Sensitive Magnetometry

In this Chapter a number of experiments are presented which were designed to investigate some of the key characteristics and parameters of the hybrid interferometers.

6.1 Superconducting Phase-Periodic Transport

Consider a SNS junction with the two superconducting electrodes connected to form a closed loop - this is the basis of the hybrid interferometer device. In this geometry, the phase between the two SN contacts can be varied by changing the magnetic field. A schematic and a scanning electron micrograph of the measured device is given in Figure 6.1. The phase difference φ between the two superconducting contacts, c and d, depends on the magnetic flux threading the loop, $\varphi = 2\pi\frac{\Phi}{\Phi_0}$. The resistance of the normal mesoscopic wire is measured between a and b. The resistance measured is a function of the phase between c and d, and thus the flux threading the loop,

$$R = R_0 - r\cos\varphi. \tag{6.1}$$

Therefore, if the magnetic flux through the loop is varied whilst measuring the differential resistance it is possible to observe phase periodic oscillations of resistance. Extrema in the resistance occur at $\Phi = n\Phi_0$ where $n = (2m+1)/2$ for maxima and $n = 2m$ for minima, where $m = 0, \pm 1, \pm 2, \pm 3 \cdots$. For the purpose of this investigation however, this view is considered incomplete. As discussed in Section 3.1.4, in a system where ξ_{n} is comparable to L, an additional flux term due to the supercurrent-induced flux must be considered. The phase would now be described by $\varphi = \varphi_{\mathrm{ext}} - \beta \sin \varphi$. The resistance is now written as,

$$R = R_0 - r \cos(\varphi_{\mathrm{ext}} - \beta \sin \varphi), \tag{6.2}$$

where $\beta = 2\pi \mathcal{L} I_{\mathrm{c}}/\Phi_0$ is the screening parameter. The relationship between total and externally applied magnetic flux is shown in Figure 6.2. If $\beta = 0$ there is a linear relationship between the two parameters. As β increases, the relationship becomes increasingly non-linear as shown by the $\beta = 0.9$ curve in the figure. At $\beta > 1$ the system becomes multi-valued. Experimentally, certain values of Φ are inaccessible - as the external flux is increased it will reach a critical value at which point the gradient of the $\Phi - \Phi_{\mathrm{ext}}$ curve becomes negative. The system then jumps to the next stable value of Φ. Reversing the direction of the applied flux reveals a hysteresis in the system.

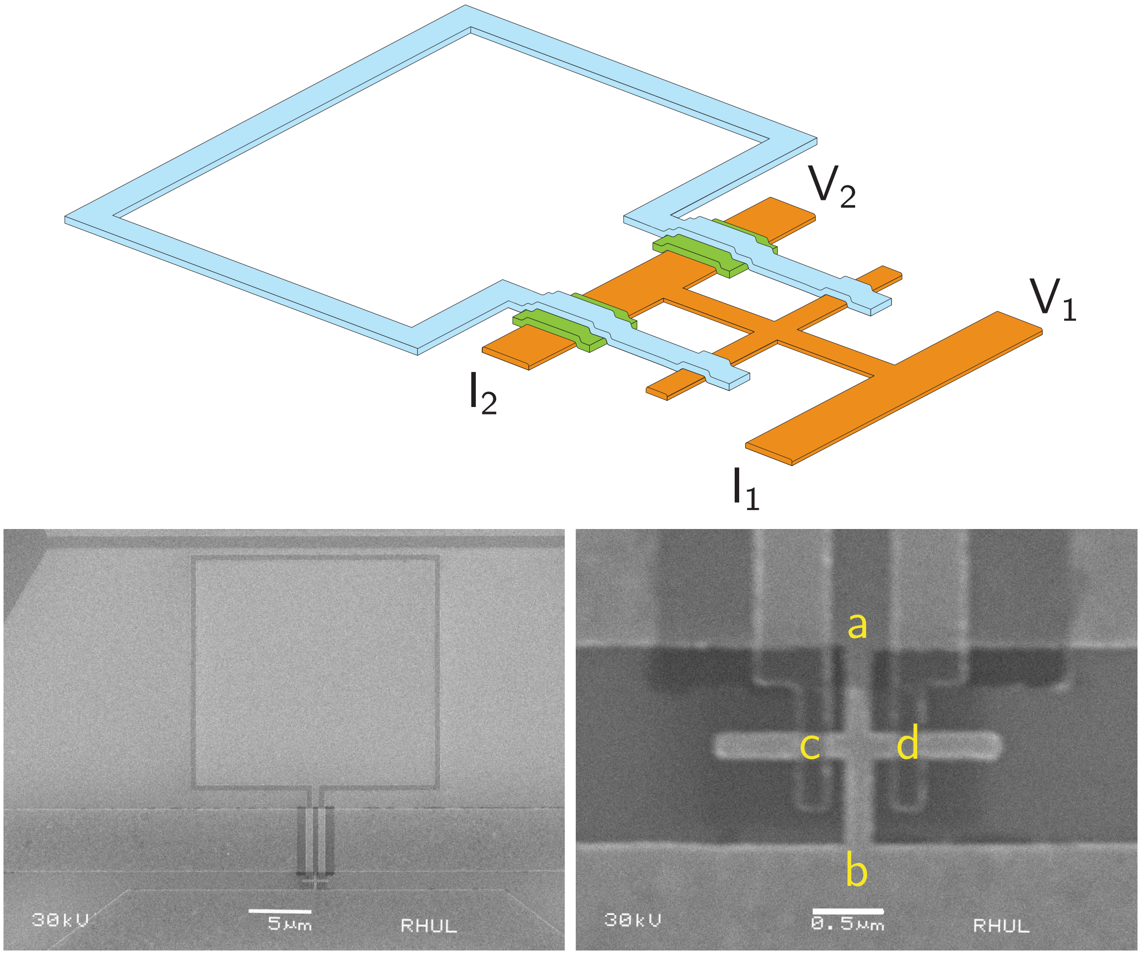

Figure 6.1: (top) shows a schematic of the hybrid interferometer device. The normal metal cross (shown in orange) is connected to a superconducting loop (shown in blue). A spacer (shown in green) insulates the two layers from one another. (bottom left) shows the full device SEM image. (bottom right) shows an image at higher magnification showing the accuracy of the superconducting contact placement with respect to the normal cross. Resistance is measured between a and b, whilst a phase difference occurs between c and d.

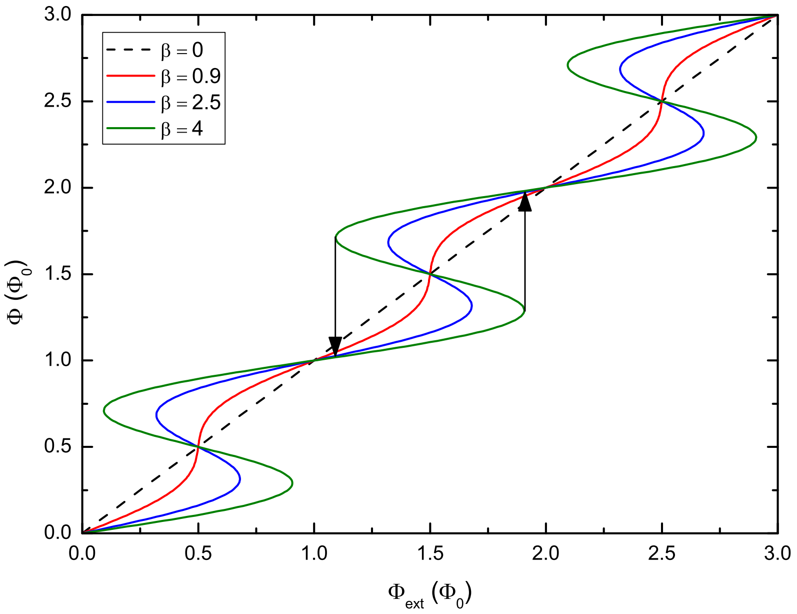

Figure 6.2: Relationship between the total flux through the loop, Φ, as a function of the externally applied flux Φ_{ext}. As the screening parameter β increases, the curve becomes increasingly non-linear. At $\beta > 1$ a negative slope arises leading to inaccessible regions of phase. Due to the inaccessible regions, the phase jumps from one branch to the other; an example of which is indicated by the arrows on the plot.

The screening parameter can be varied by changing either the loop inductance, $\mathcal{L}$, or the critical current, I_c. In the experiments presented here the loop inductance is related to the geometry of the loop, which is determined during the fabrication process. The critical current can be varied, as was discussed in Sections 3.1.3 & 3.2.1, by temperature, or an applied bias current. Due to the screening parameter, the flux jumps shown in Figure 6.2 can be observed in the magnetoresistance oscillations. The screening parameter causes deviations from a typical sinusoidal line-shape. Figure 6.3 shows experimental magnetoresistance measurements taken with different dc offsets applied to the measuring current. At the lowest bias current shown ($30\,\mu$A) the curves exhibit strong hysteresis when measured in positive and negative directions. At a critical flux, the system enters an unstable position and a sharp drop in the resistance is observed. It shall be shown in Section 6.3 that the critical current in the interferometer is reduced as the applied bias current is increased. It follows that an increase of the bias current results in a reduced screening parameter. It is evident in Figure 6.3 (b) & (c) that the critical flux required to exhibit a drop in resistance gets closer to $\Phi_0/2$ as the bias current is increased. Figure 6.3 (d) shows oscillations with no sudden drop in the resistance. It is expected that the screening parameter in the last case would be less than 1. The origin of the resistance drop is the non-linearity of the Φ vs Φ_{ext} relationship when $\beta > 1$.

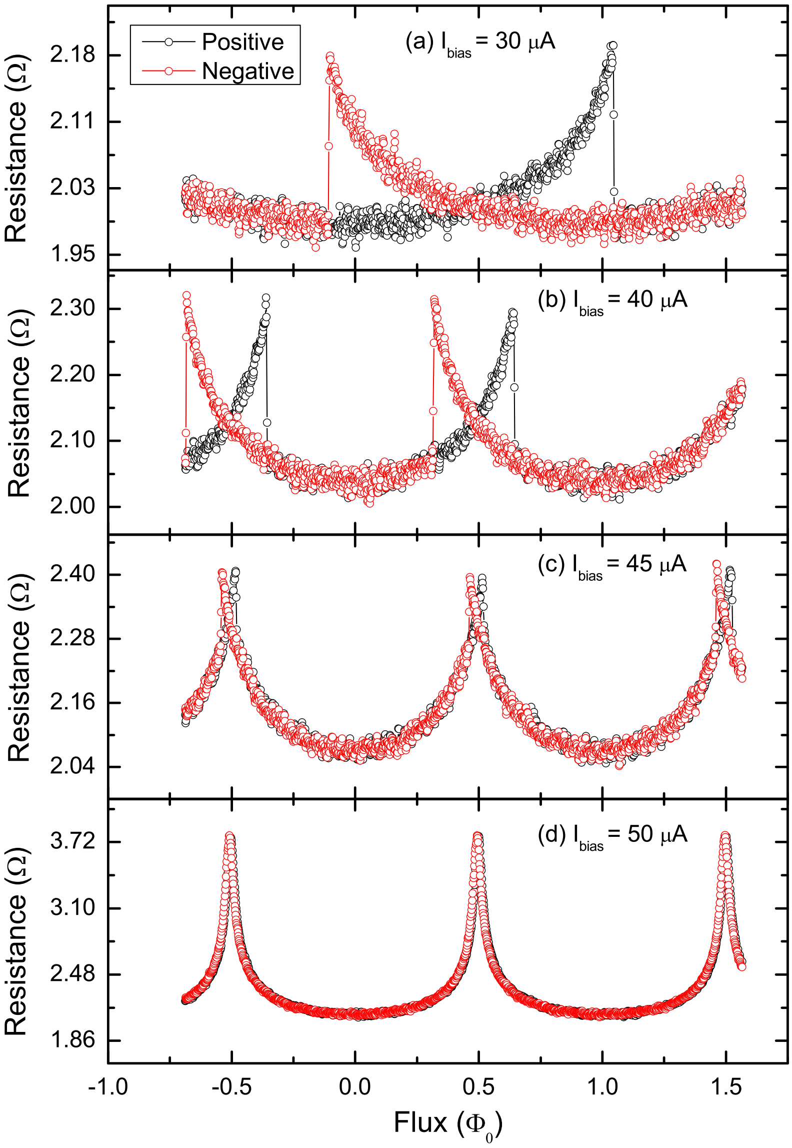

Figure 6.3: Magnetoresistance oscillations of device shown in Figure 6.1. Measurements recorded with increasing bias current (a → d). As a consequence, the critical current is reduced. Due to the definition of the screening parameter $\beta = 2\pi\mathcal{L}I_c/\Phi_0$, a decrease in the critical current results in a reduction of β. It is clear in (a), (b) and (c) that at some critical flux a sudden drop in the resistance is observed. (d) shows no evidence of entering this 'unstable' state as no resistance drop is observed. Note that the amplitude of the measurements are not the same at each bias current.

It is possible to obtain values of the screening parameter, β. Using Equation 6.2 the oscillations can be fit using β as one of the fitting parameters. In the case of $\beta > 1$, large regions of the phase are inaccessible resulting in the sharp drops in resistance. The sharp drop occurs when the theoretical curve takes on a negative gradient. An example of two large β measurements are shown in Figure 6.4.

As $\beta \to 1$ the curves tend to a more 'cusp-like' line-shape. Using Equation 6.2 it is not possible to obtain reasonable fits to the measured line-shape (see Figure 6.5 (a)). A better fit is achieved when the second harmonic of the critical current is taken into account. The total supercurrent is given by [108],

$$I_{\mathrm{s}} = \sum_{j} \beta_{(j)} \sin(j\varphi). \tag{6.3}$$

The supercurrent used to fit the 'cusp-like' oscillations including the contributions from the second harmonic is given as,

$$I_{\mathrm{s}} = \beta_{(1)} \sin(\varphi) + \beta_{(2)} \sin(2\varphi). \tag{6.4}$$

The improvement in the fit when including the second harmonic of the supercurrent is shown in Figure 6.5 (b).

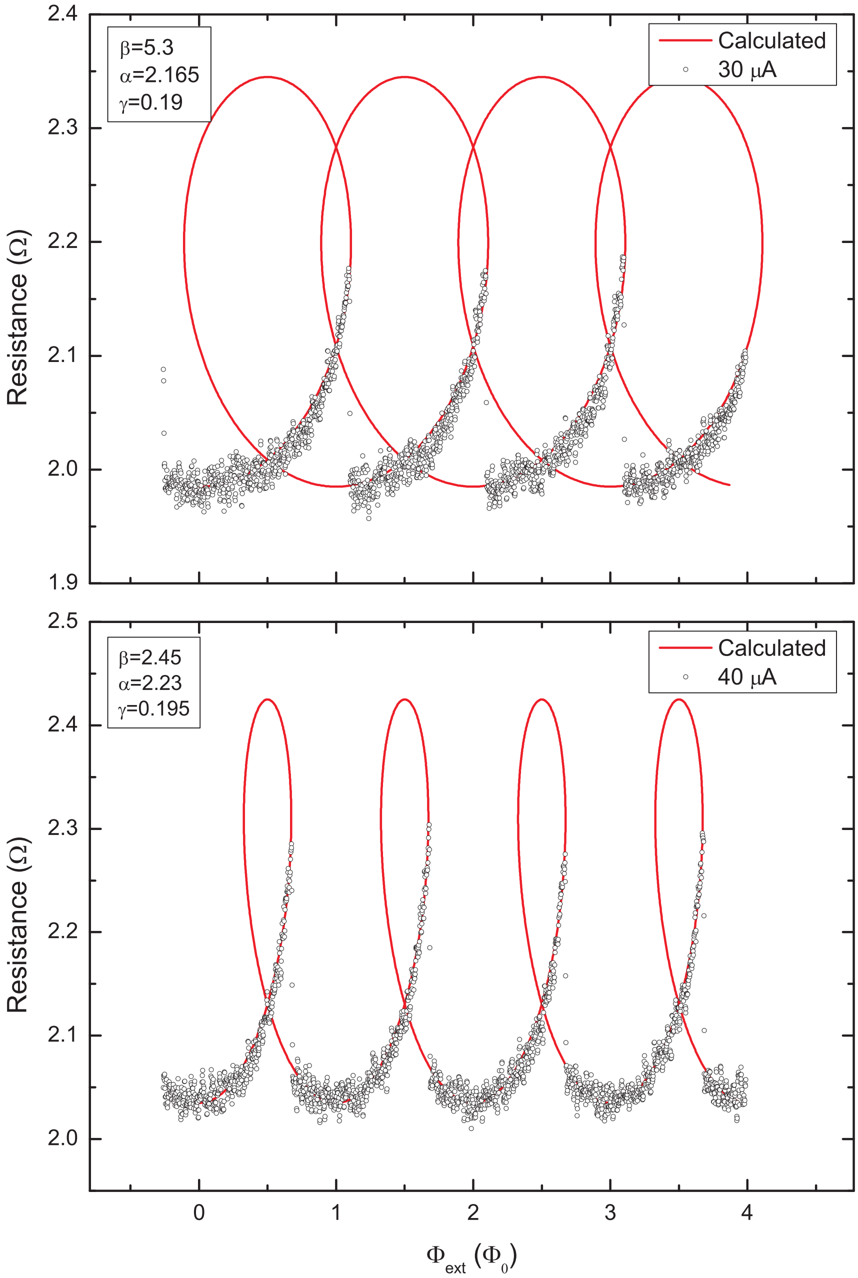

Figure 6.4: Magnetoresistance oscillations at two different bias currents, I_{bias}= 30 and 40 μA. There is a clear jump in the resistance as Φ_{ext} is increased. The red line is a fit to the oscillations using Equation 6.2. The jump in resistance occurs due to the negative slope of the calculated curve. The fitting parameter is the screening parameter β which increases as I_{bias} is reduced.

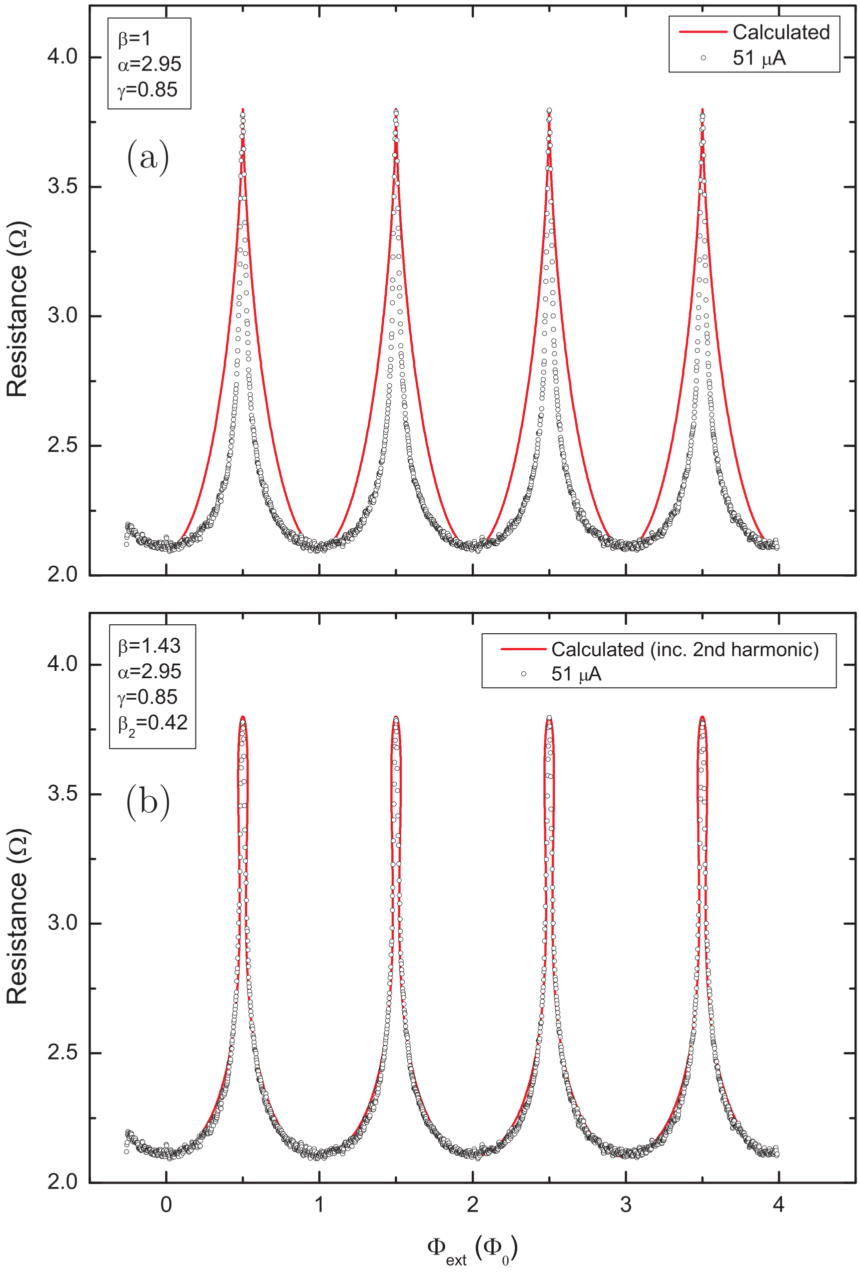

Figure 6.5: As the I_{bias} is increased and β approaches 1 the data becomes harder to fit as shown by (a). Including the second harmonic of the supercurrent in the calculated fit improves the quality of the fit as shown in (b).

6.2 Metastable States in the Hybrid Interferometer

By utilising information gained in the preceding sections it is possible to fabricate a device and bias it with the appropriate dc current in order to operate in the $\beta > 1$ regime. The sample is shown in Figure 6.6 and measurements were obtained at approximately 250 mK. This device exhibited exactly the same line-shape progression as detailed in Section 6.1.

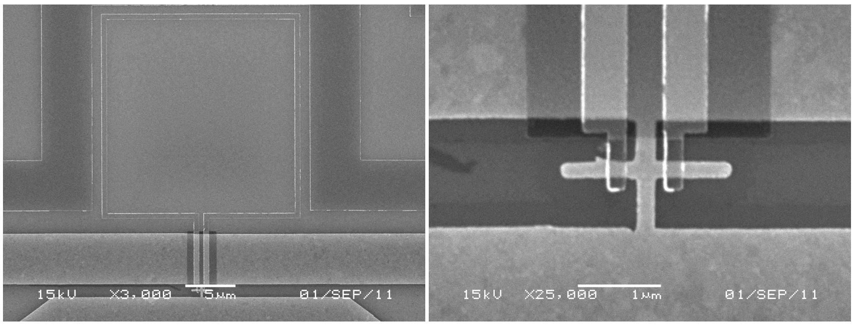

Figure 6.6: SEM images of the sample used for the metastable state experiment. (left) shows a low magnification image of the whole device including the interferometer, superconducting loop and the on-chip field source. (right) shows a higher magnification of the interferometer and superconducting loop contacts. The thickness of the Ag and Al are 50 nm and 70 nm respectively. L_{SNS}=500 nm.

As the device is operated in the $\beta > 1$ regime, the resistance oscillation line-shape will be strongly hysteretic due to the unstable branches of the Φ vs Φ_{ext} relationship. As before, certain regions of the magnetoresistance oscillations are inaccessible leading to the observed hysteresis. In this regime the investigated system can be modelled as a particle trapped in a double well (see Section 3.1.4) with a potential energy described by,

$$U_{\mathrm{S}}(\phi) = E_{\mathrm{J}}\left[1 - \cos\phi + \frac{(\phi - \phi_{\mathrm{ext}})^2}{2\beta}\right] + \mathrm{const.} \tag{6.5}$$

The escape rate from such a system is given by,

$$\Gamma = \frac{\omega}{2\pi} e^{-\frac{U_0}{k_{\mathrm{B}}T}}. \tag{6.6}$$

The escape rate can be experimentally determined using a double-step flux pulse profile, similar to that previously used by Lisenfeld [109], as shown in Figure 6.7.

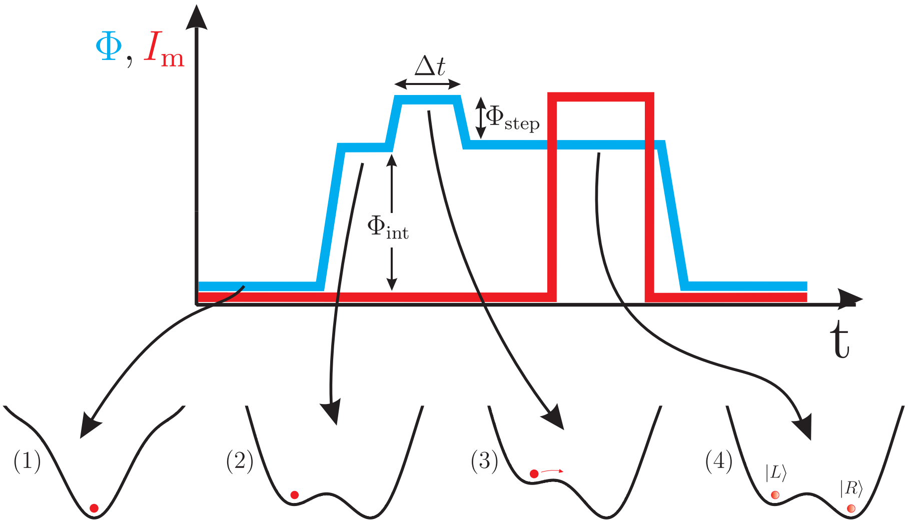

Figure 6.7: Schematic of the pulsed measurement technique: (1) At the initialisation flux the 'particle' is trapped in the minimum. (2) The flux is then increased to an intermediate value which raises the potential of the system. (3) A short pulse that increases the flux is applied for 200 μs - it is possible that this pulse may lower the barrier enough to allow the particle to enter the other potential well. (4) The flux is then reduced back to the intermediate value which raises the barrier, a measurement pulse then is applied to the Andreev cross to determine its resistance and thus what state it is in. By repeating this hundreds of times for each flux step it is possible to determine the probability of changing states. The physical representation of the two states is the two distinct resistance levels depending on what branch of the hysteresis curve the device is on.

The lowest flux level is the 'initialisation' flux, which prepares the system by putting the particle in the single minimum. The flux is then increased to an intermediate level at which the two wells are at similar potential energies. The second pulse, Φ_{step}, is applied for a time Δt which lowers the barrier between the two wells. It is during this time period that the particle may escape from its initial well. After Δt has elapsed the flux is reduced back to the intermediate state allowing the barrier to increase again. A current pulse is then sent through the cross to measure the voltage across the device. The 'particle in a double well' model describes the state (or branch of the Φ vs Φ_{ext} graph) that the system is in. Therefore, the voltage measurement is sufficient to determine the state the system is residing in. This process is repeated 100 times to obtain an averaged resistance value which will lie somewhere between the two possible resistance states. This method is then repeated for a number of different values of Φ_{step}. The probability of the system being found in a given state is found by balancing the escape rates Γ_{01} and Γ_{10}, such that,

$$\frac{\mathrm{d}P_0}{\mathrm{d}t} = -\Gamma_{01}P_0(t) + \Gamma_{10}P_1(t), \tag{6.7}$$

where $P_0(t) + P_1(t) = 1$ [110]. P_0 and P_1 describe the probabilities of finding the system in the left or right well. Γ_{01} and Γ_{10} are the escape rates describing the transition from the left to right well and vice versa. A simplification to the expression can be made due to our method of measurement which involves always initialising (at t=0) the system in the left well (for instance). The expression is then simplified to,

$$\frac{\mathrm{d}P_0}{\mathrm{d}t} = -\Gamma_{01}. \tag{6.8}$$

Therefore the probabilities of finding the system in the left (P_0) or right (P_1) well are described by,

$$P_0 = e^{-\Gamma_{01}\Delta t}, \tag{6.9}$$

$$P_1 = 1 - e^{-\Gamma_{01}\Delta t}. \tag{6.10}$$

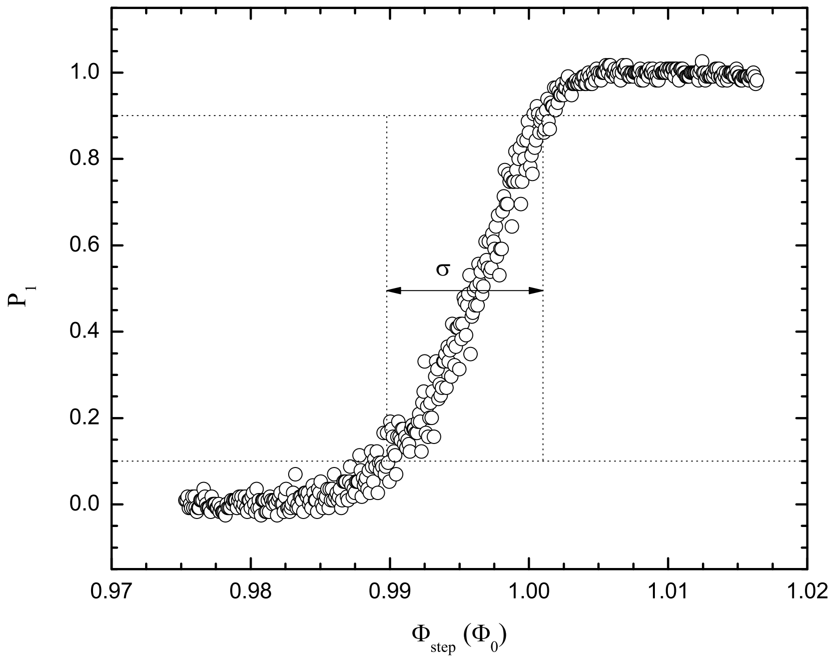

Figure 6.8: Experimentally measured escape probability vs the amplitude of the flux pulse Φ_{step}. σ defines the width of the external flux between $P_1 = 0.1$ and $P_1 = 0.9$. Measurements taken at 250 mK.

The parameter σ displayed on the graph defines the difference in applied flux between $P = 0.1$ and $P = 0.9$. The importance of this value is that it demonstrates that the interferometer can detect changes in flux $\sigma \approx 0.01\,\Phi_0$ with 80% fidelity. A similar latching technique using a Josephson bifurcation amplifier [111] has been used to probe the state of a superconducting flux qubit [112, 113].

6.2.1 Time Domain Measurements

In this brief subsection, measurements are presented that show switching between two distinct states. Although these measurements were performed at dilution fridge temperatures of approximately 20 mK the sample used showed similar magnetoresistance properties as those used in the flux pulse experiments already presented. Once again the interferometer is biased such that the line-shapes are strongly hysteretic. Figure 6.9 shows a close-up of the measured magnetoresistance curves in the large-β regime of the device. The solenoid current was swept forwards and backwards to obtain the two sets of data.

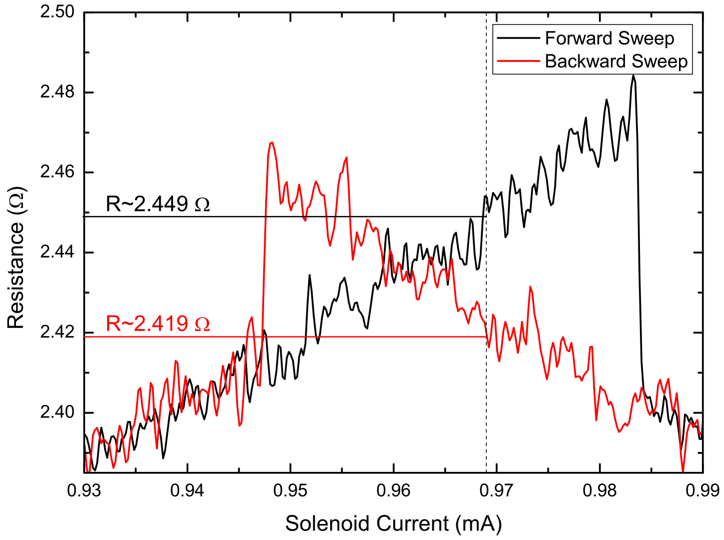

Figure 6.9: Close-up of magnetoresistance oscillations showing both forward and backward sweeps of magnetic field. The measurement is taken as a precursor to a time trace to observe switching events - by setting the magnetic field to one static position (dashed line) two distinct states are available. The states are defined by their different resistance values.

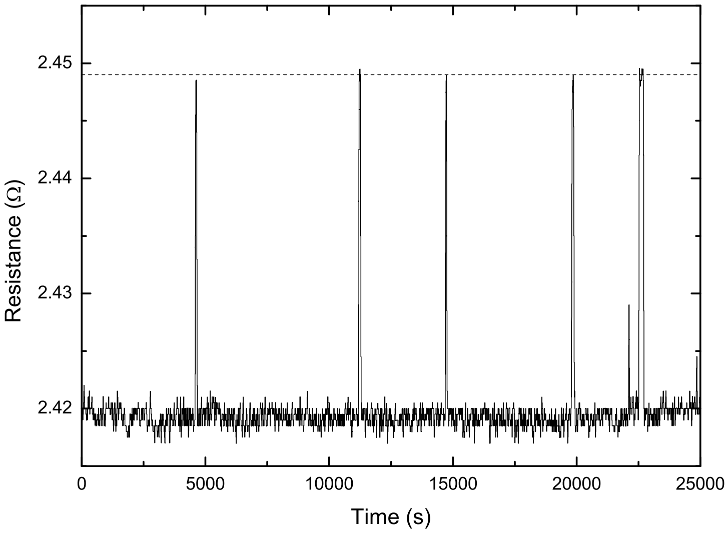

Figure 6.10: Time trace of the resistance whilst magnetic field position is constant. Distinct jumps are observed between the two states. The dwell time in the higher resistance state is much smaller compared to that of the lower state.

It is clear from the image that if the magnetic field is held at a stationary position (see dashed line) the device can exist in one of the two branches of the magnetoresistance curve. This results in a possibility of the device being in one of two distinct resistance states. In order to measure how stable the resistance states are the device was initialised to the lower resistance state and then held stationary (solenoid current held constant) for the duration of the measurement. The resistance of the cross is then measured continuously as a function of time. Figure 6.10 shows distinct jumps between the two resistance states as a function of time. It is possible that the switching between the two states is evidence of 'random telegraph signals' typically associated with two-level systems [106]. In this case it is seen that the dwell time in the higher resistance state is very small and the system quickly returns to the lower resistance state.

6.3 Investigation of the Critical Current in a SNS Junction

So far, it has been seen that the line-shape of the phase-periodic resistance oscillations can be controlled by changing the screening parameter of the system. As the inductance $\mathcal{L}$ is set by the geometry during fabrication, the critical current is changed to vary the screening parameter. Varying β has allowed us to work in both hysteretic and non-hysteretic regimes. The following section describes the experiments carried out to investigate how the critical current of a SNS junction can be varied by geometry (length of the junction, L_{SNS}), temperature and current bias. The first experiment is designed to investigate how the critical current I_{c} of an SNS junction varies with application of a perpendicular control current, I_{ctrl}. In order to investigate the SNS device fully a normal metal control line was added perpendicular to the SNS junction. The control line was attached to an electrode at either end, one normal and one superconducting. Each electrode then split into two to allow 4-point measurements to be carried out. The geometry is shown in Figure 6.11, note that in this device the superconductors do not form a closed loop - instead each lead is connected to a pad on the chip to be connected to the room-temperature electronics. Four separate devices were fabricated, identical in their geometry except for the distance between the two superconducting electrodes, L_{SNS}. The four L_{SNS} values investigated were 0.5, 1, 1.5 and 2 μm.

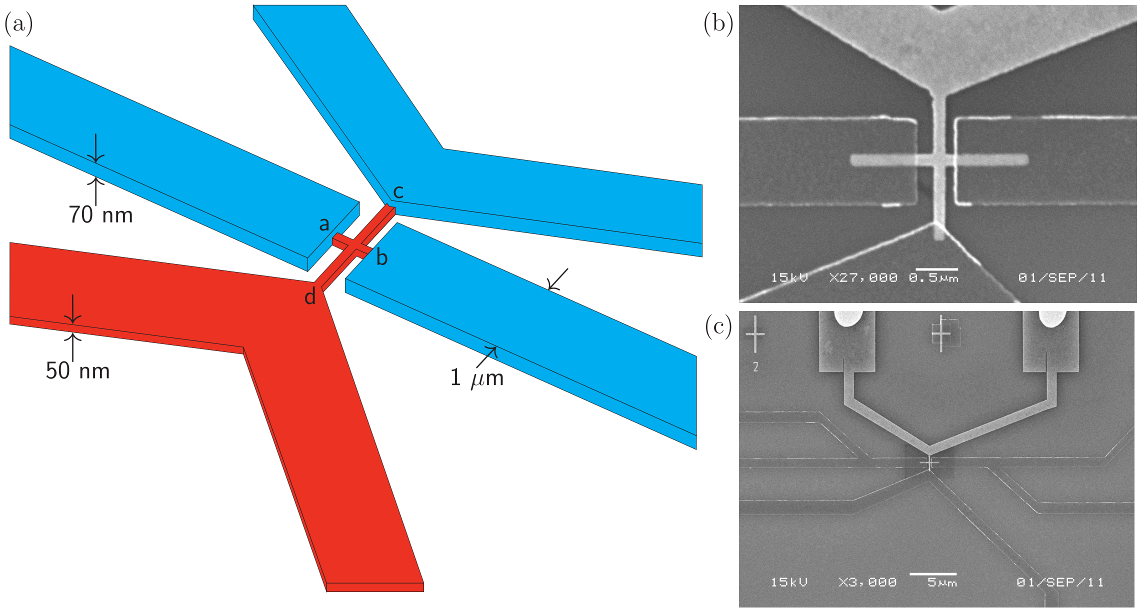

Figure 6.11: (a) Schematic of the SNS sample; normal metal shown in red, superconductor shown in blue. Four samples were made with different L_{SNS} (0.5, 1, 1.5 and $2\,\mu$m). The control line is attached perpendicular to the SNS junciton and was the same length in each sample, $L_{\mathrm{ctrl}} = 1.5\ \mu$m. (b) Scanning electron micrograph showing the normal cross connected to 3 'S', and 1 'N' electrode. (c) is a lower magnification image showing the extent of the measurement leads allowing for 4-point measurement of both the SNS line and the control line.

The differential resistance was measured across the SNS junction, the results can be seen in Figure 6.12. From the differential resistance measurements it is clearly observed that the critical current of the junction reduces as the length of the normal metal is increased. This dependence is to be expected as it has already been stated (see Section 3.1.3) that the critical current is related to the length of the junction by $I_{\mathrm{c}}(L) \propto e^{-L/\xi_{\mathrm{N}}}$. Figure 6.13 shows a plot of L_{SNS} verses I_{c} and a fit to the equation is obtained. The fitting parameter of importance is ξ_{N}=5.7 × 10^{-7} m. This is in reasonable agreement with the coherence length, ξ_{N}=4.4 × 10^{-7} m, determined from the resistivity of the silver, ρ=1.4 × $10^{-8}\,\Omega$m.

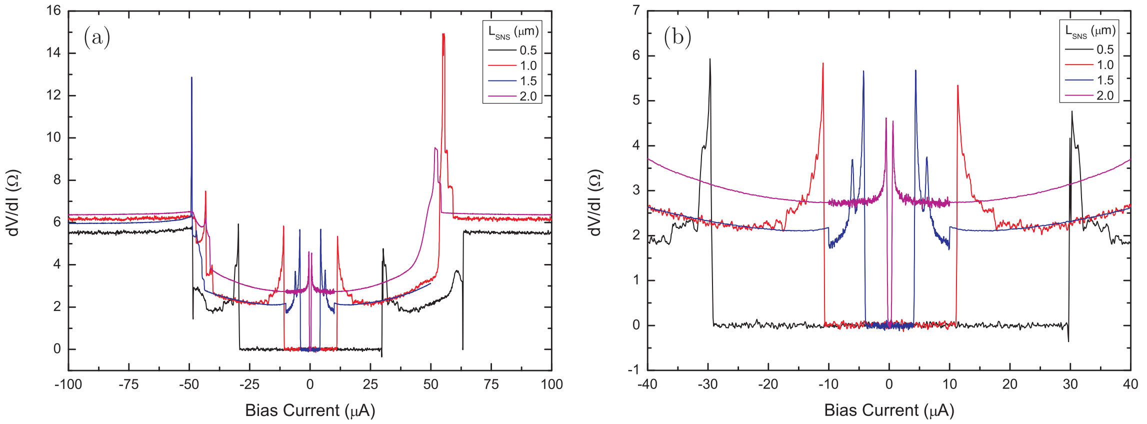

Figure 6.12: (a) Differential resistance measurements of the SNS junction of the samples. It is clear that an increase in the SNS length of the device results in a reduced critical current. (b) shows the same data but at zoomed in on the critical current region. Note that the increased noise in the 1.5 and 2 μm sweeps between -10 and +10 μA is because the data shows two separate sets of measurements. The 'noisier' data is taken with a smaller I_{osc} and is swept slower. Using high measuring currents and sweeping quickly can inhibit transition to the superconducting state. Measurements taken at T=250 mK, $I_{\text{ctrl}} = 0$.

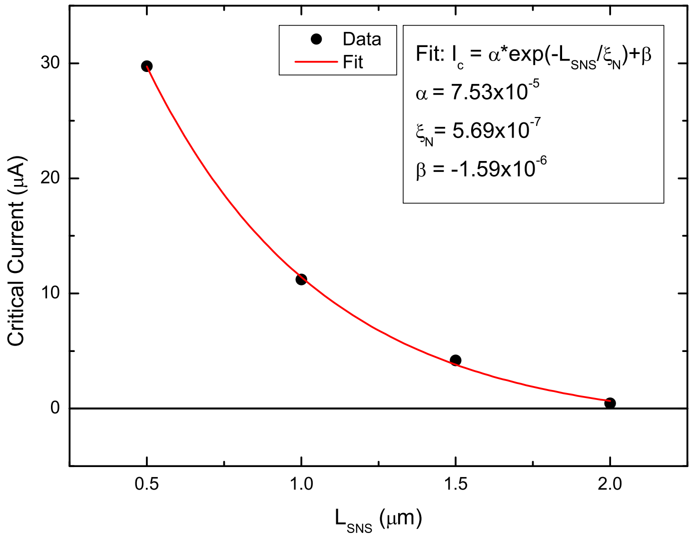

Figure 6.13: Graph showing reduction of I_c as L_{SNS} is increased. The critical current values are determined from the experimental dV/dI measurements taken at base temperature, T=245 mK. Following a fit to $I_c(L) \propto e^{-L/\xi_N}$ the coherence length is calculated to be ξ_N=5.7 × 10^{-7} m.

A more recent theory by Zaikin [45] was also used to fit the data. In the long-junction limit the critical current is given as $I_c(L) \propto (L^3/\xi_N^3)e^{-L/\xi_N}$. In this regime the fitting parameter is calculated to be ξ_N=1.7×10^{-7} m. The fit is shown in Figure 6.14.

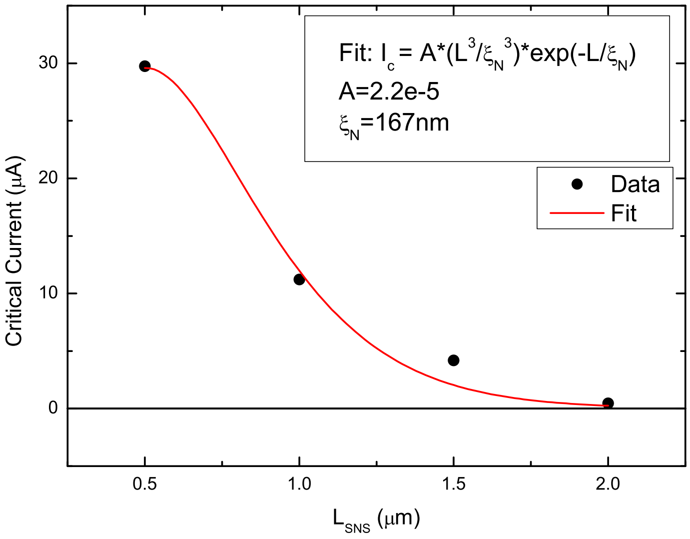

Figure 6.14: Graph of I_c as $L_{\rm SNS}$ is increased. The fit to $I_c(L) \propto (L^3/\xi_N^3)e^{-L/\xi_N}$ given in [45] yields a the coherence length of ξ_N=1.7×10^{-7} m.

6.3.1 Temperature Dependence of the Critical Current

It is clear that the critical current is strongly dependent on the length of the SNS junction. It was also mentioned previously (see Section 3.2.1) that the temperature affects the critical current of the junction. Results are presented here of the temperature dependent measurements of three of the samples, $L_{\rm SNS}$ = 0.5, 1, and 1.5 μm. The fourth sample ($L_{\rm SNS}$ = 2 μm) was not investigated further due to its very small base temperature critical current. It is likely that any increase in bath temperature would result in transition to the normal state for this sample. Measurements were performed by heating the sorb and allowing the helium to re-condense. Differential resistance measurements are performed on the SNS junctions whilst the fridge is cooling. Figure 6.18 shows the temperature dependence of the critical current for the three L_{SNS} investigated.

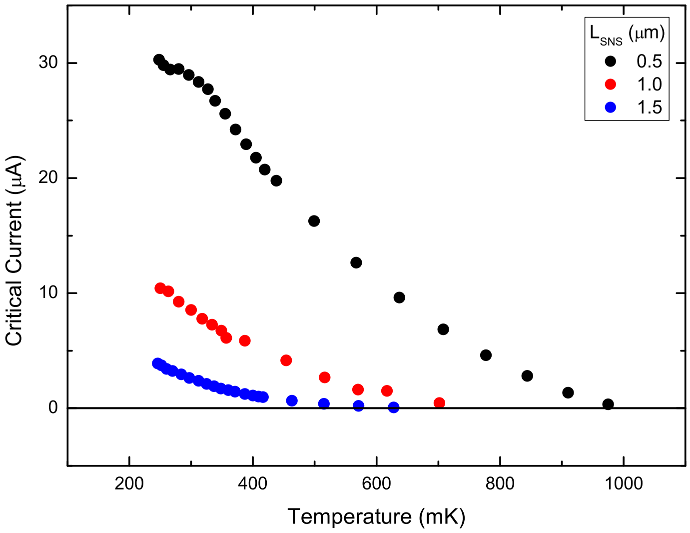

Figure 6.15: Temperature dependence of the critical current for three SNS lengths: $L_{\mathrm{SNS}} = 0.5$, 1, and 1.5 μm.

The measured temperature dependencies are compared to the to existing SNS junction theory mentioned above described by Zaikin [45]. In this case the dependence of critical current on length which, for the long-junction regime, is given by;

$$eR_{\mathrm{N}}I_{\mathrm{c}} = \frac{32}{3+2\sqrt{2}}E_{\mathrm{Th}}\left[\frac{L}{\xi_{\mathrm{n}}}\right]^3 e^{-L/\xi_{\mathrm{n}}}, \tag{6.11}$$

can be used to determine the critical current temperature dependence. By combining the constants it is possible to fit the critical current temperature dependence as follows,

$$I_{\mathrm{c}} \propto \left[\frac{L}{\xi_{\mathrm{n}}}\right]^3 e^{-L/\xi_n}. \tag{6.12}$$

Recall that the coherence length is given by $\xi_{\mathrm{n}} = \sqrt{\hbar D/2\pi k_{\mathrm{B}}T}$, thus the temperature dependence of the critical can be written as,

$$I_c \propto AT^{3/2}e^{-B\sqrt{T}}. \tag{6.13}$$

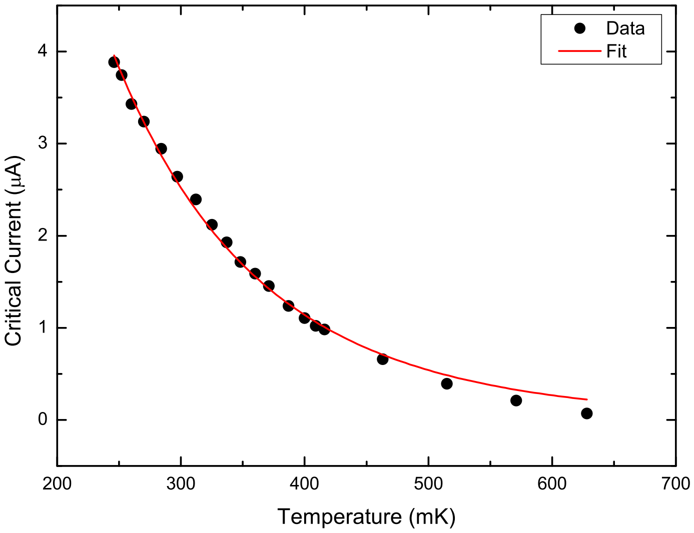

Figure 6.16: Temperature dependence of the critical current for 1.5 μm sample. The data is fit using Equation 6.13.

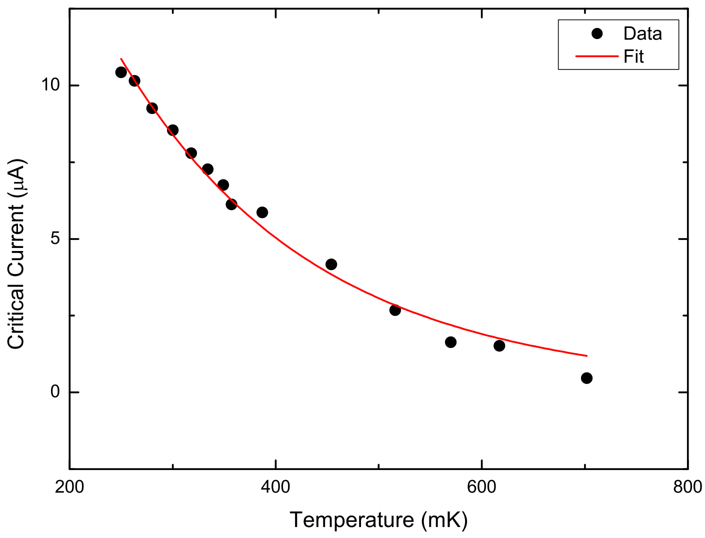

Figure 6.17: Temperature dependence of the critical current for 1 μm sample. The data is fit using Equation 6.13.

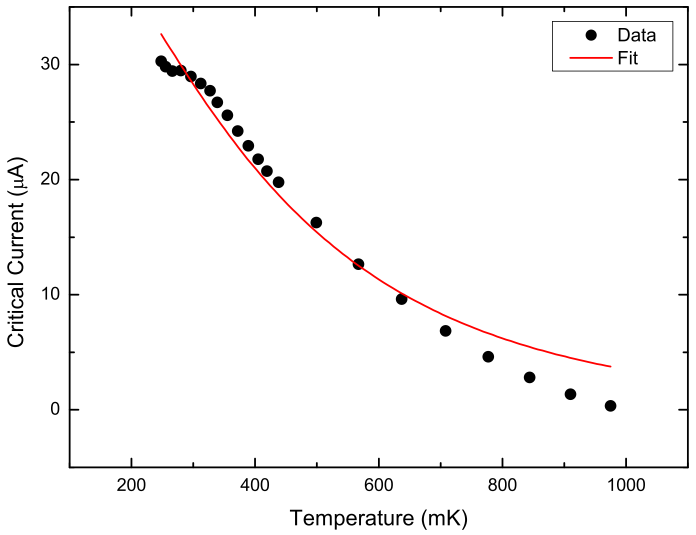

Figure 6.18: Temperature dependence of the critical current for 0.5 μm sample. The data is fit using Equation 6.13.

Clearly the larger SNS junction measurements are better fit by the long-junction theoretical approach. As L_{SNS} is reduced the further the fit deviates from the data set. It should be noted that the theoretical treatment considers only a diffusive normal metal between two superconducting electrodes. The devices presented here are also attached to a normal metal reservoir and an additional superconducting electrode by the perpendicular control line. This type of geometry is not considered within this theory.

6.3.2 Applying a Control Current: Observation of the π-effect

Two devices were fabricated differing only in configuration of the normal and superconducting leads. The geometry and configuration of the two samples are shown in Figure 6.11 (*SNN*) and Figure 6.19 (*NNN*). Both samples contained a normal metal cross made of silver. The cross is 50 nm in thickness and 100 nm wide. Two of the arms of the cross are connected to aluminium electrodes 0.5 μm apart to form the SNS junction under investigation. The perpendicular control line has a different geometry in each of the two samples. The first structure, designated as *NNN*, has silver electrodes connected at either end of the control line 1.5 μm apart from one another. The second structure, designated as *SNN* has a silver electrode at one end of the control line and a superconducting aluminium electrode at the other end, again, 1.5 μm apart from one another. The electrodes are approximately 1 μm wide. The silver electrodes are 50 nm thick whilst the aluminium electrodes are 70 nm thick.

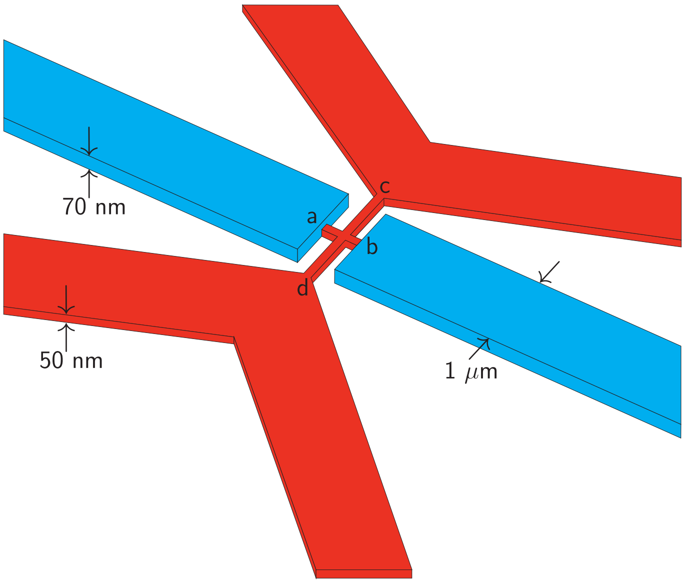

Figure 6.19: Schematic of the *NNN* sample: Red indicates the normal metal components made of silver, blue indicates the superconducting components made of aluminium. The SNS junction weak link occurs between a and b with a length of $L_{\text{SNS}} = 0.5$ μm. The control line is defined by the length between the two normal reservoirs c and d, L_{ctrl}=1.5 μm

As mentioned above, the devices were made with an additional normal metal connected perpendicularly to the the SNS junction forming a normal metal cross-like structure. This allows one to apply a control current perpendicular to the SNS junction. Figure 6.20 shows a colourmap plot of differential resistance measurements of the SNS junction whilst the control current is increased from 0 to 60 μA in steps of 1 μA. It is expected that an additional current in the system is likely to cause a reduction of the overall critical current available in the SNS junction (see Section 3.2.1) and this is indeed observed - full suppression of the critical current occurs when the control current reaches 36 μA. Further increase of the control current results in a reappearance of the critical current prior to complete suppression at a control current of 44 μA. Further increase of the control current has no effect beyond this point and a second reappearance is not observed.

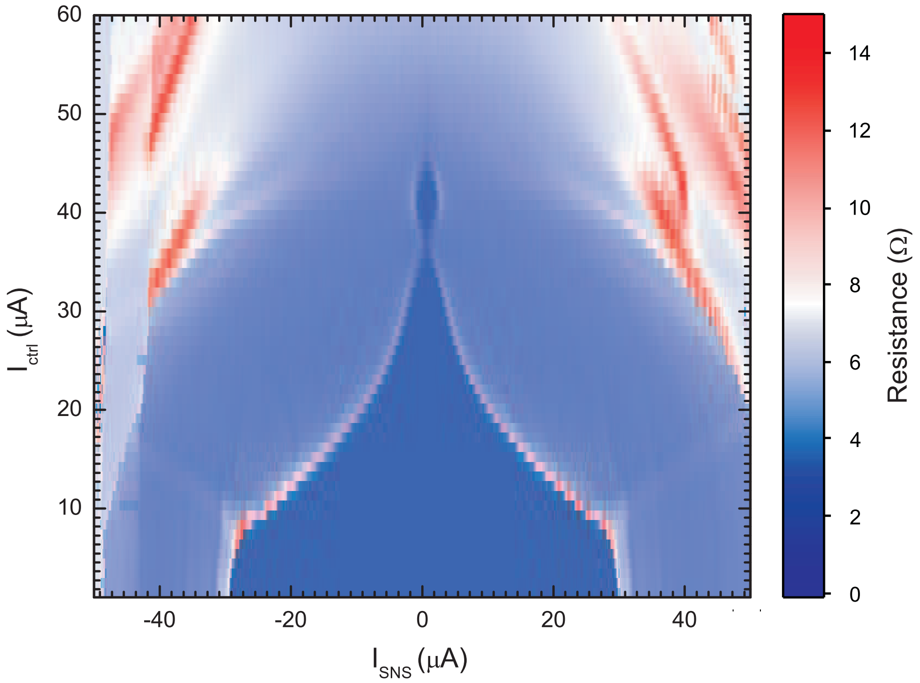

Figure 6.20: Colourmap plot of the differential resistance measurements of the SNS junction. The applied control current is stepped from 0 to 60 μA in 1 μA increments. Clear suppression of the critical current is observed at approximately I_{ctrl}=36 μA. In the range 36 μA $< I_{\mathrm{ctrl}} <$ 44 μA the critical current of the SNS junction reappears.

Typically the suppression and subsequent reappearance of critical currents in SNS junctions is evidence of a transition of the system into the π-state as observed in mesoscopic SNS systems by Baslemans *et al* [79, 80] (see Section 3.2.2). Previous experimental observations of the π-junction effect are seen using 4-terminal devices: two superconducting electrodes to form the SNS junction and two normal reservoirs to provide the control current. The normal reservoirs are made of a thick layer of normal metal (475 nm of Au, 1 mm in lateral dimensions [80]) - the reason bulk reservoirs are used is to ensure the distribution functions are well-defined. In the middle of the control line, the distribution function is expected to be a double-step and thus positive supercurrent-carrying states can be excluded as discussed in Section 3.2.1.

The device presented in this experiment does not have 'bulk' reservoirs as was necessary in previous work. In addition the control line is attached to only one normal contact, the remaining contact is a superconducting electrode.

6.3.3 Comparison of 'SNN' and 'NNN' Geometries

In order to investigate if the additional superconducting contact is responsible for the transition to the π-state a comparison with a sample with two thin normal control contacts must be made. The *SNN* device is that shown previously in Figure 6.11. The second sample was fabricated with the same dimensions, however both control line contacts were made of silver - the sample is referred to as *NNN*. The thickness of the silver contacts were 50 nm which would not be considered 'bulk' and thus it was predicted that no π-effect would be observed in this sample. The schematic for this sample is shown in Figure 6.19.

The comparison of *SNN* and *NNN* curves are shown in Figure 6.21. It is clear that no reappearance of the critical current is observed in the *NNN* sample containing only thin (50 nm) normal reservoirs at the end of the control line.

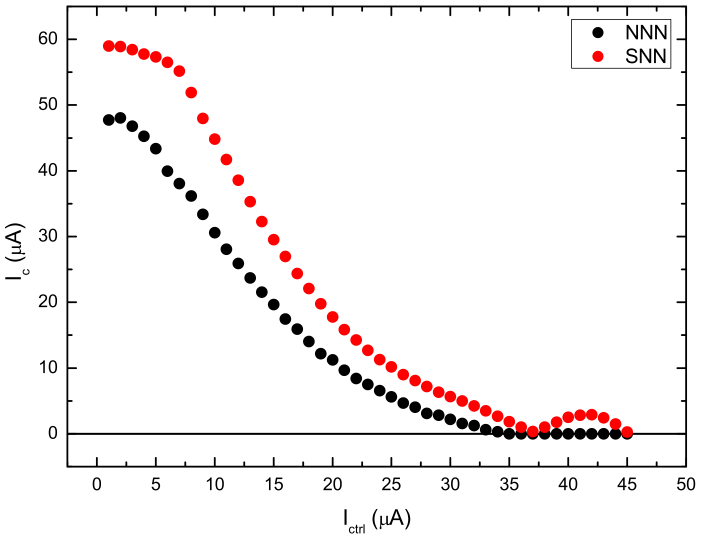

Figure 6.21: Graph of the two different samples, *NNN* and *SNN*. Clear reappearence of the critical current is exhibited in *SNN*. In the *NNN* sample no transition to the π-state is observed, just full suppression of the critical current to zero.

Although the *SNN* device shows a clear reappearance of critical current it is necessary to provide further evidence to confirm that a transition into the π-state occurs. The differential resistance of the control line is measured whilst the current through the SNS junction is varied. Given that, from the dc Josephson effect, the current-phase relation is given by $I = I_c \sin(\phi)$, the resistance of the control line should go through a minima at I_{SNS}=0. This is indeed observed in the measurements presented here with a minima in the resistance of all sweeps up to the first suppression of the critical current. Assuming the reappearance of the supercurrent is a transition to the π-state the current-phase relation would be given by $I = I_c \sin(\phi + \pi)$. In this case, when I_{SNS}=0, $\phi = \pi$. Differential resistance measurements taken with control currents in the region of the π-state exhibit a maxima at I_{SNS}=0. This is considered direct proof that the junction switches from a normal state to a π-state as a function of the applied control current [79].

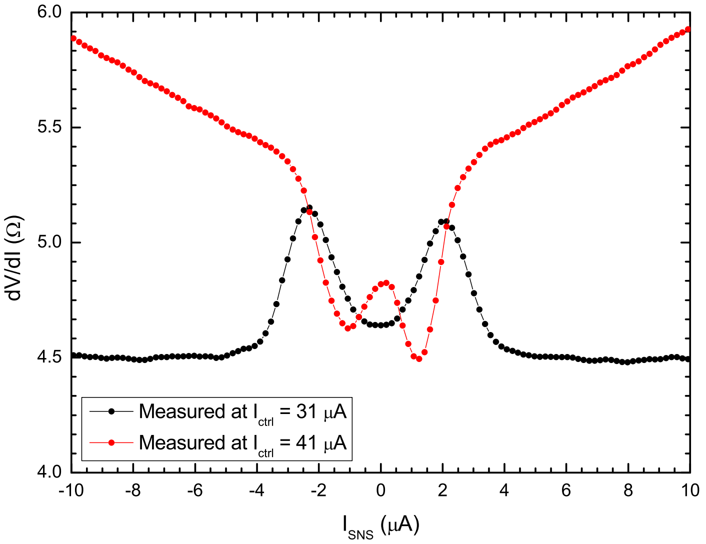

Figure 6.22: dV/dI measurements close to I_{SNS}=0. At I_{ctrl}= 31 μA the current-phase relationship is described by $I = I_{\mathrm{c}} \sin(\phi)$ and a minimum in the resistance is observed at I_{SNS}=0. At I_{ctrl}= 41 μA, beyond the transition to the π-state, the current-phase relationship is described by $I = I_{\mathrm{c}} \sin(\phi + \pi)$. The change of phase results in a maxima in the resistance at I_{SNS}=0.

6.4 Summary

The experiments described in this chapter provide the groundwork for the choice of device parameters used in the next chapter. In order to obtain a sinusoidal line-shape, the strongly hysteretic regime investigated in Section 6.1 is to be avoided. Although a device operated in the hysteretic regime could be potentially useful as a latching read-out device, the experiments in the next chapter require a non-hysteretic regime. It has already been seen that one device can be operated in either regime by in-situ modification of the screening parameter β by means of controlling the critical current. This would mean that any device could be used and shifted to the required regime by application of additional bias current. The disadvantage to operating a device that requires an additional bias current to enter the sinusoidal non-hysteretic regime is that the device now has an extra current present in the system. In the early sample designs such as those shown in Figures 6.1 and 6.6 it is quite clear that by having a comparatively large bias current present to reduce β it is possible to couple extra flux into the system through the measurement leads that are inside the loop area. This is a strong incentive to fabricate the device with parameters that put the device in the non-hysteretic regime with zero additional current. The previous point also highlights an important oversight which is addressed in the following chapter. Regardless of the need for an additonal bias current, the usual ac measuring current (which is typically small - 0.1 to $1\,\mu$A) is still present inside the interferometer loop and could lead to some flux pick-up. In order to remedy this a folded interferometer cross was developed in which the cross is split into two sections laid on top of one another with a SiO spacer layer in between. The repositioning of the current and voltage leads of the measuring cross to be outside of the interferometer loop reduces the spurious flux felt by the system. The investigation into the length dependence and temperature dependence of the critical current in the interferometer system provides a framework of design rules. With this experimental data available it is possible to manufacture a device to work in either the hysteretic or non-hysteretic regime (whichever is appropriate for the experiment) and to fabricate a device optimised for the experimental set-up available, for instance in a 300 mK ^{3}He system or a 20 mK dilution refrigerator. Note also that the inductance of the measuring loop can also be varied during the fabrication stage as it is a geometry dependent parameter. This too affects the value of the screening parameter.

CHAPTER 7

Resolving the Thermoelectric Paradox in Inhomogenous Superconductors using HyQUIDs

This chapter presents the results of an investigation into thermoelectric effects in inhomogeneous superconductors using the hybrid quantum interferometer as a read-out device. It has already been discussed in Chapter 2 that applying a temperature gradient to a normal conductor results in an electric current, $\vec{j_{\mathrm{n}}} = -\eta_{\mathrm{n}} \nabla T$ where η_{n} is the thermoelectric coefficient. Similarly it is found that application of a temperature gradient to a superconductor results in a thermoelectric current $\vec{j_{\mathrm{q}}} = -\eta_{\mathrm{s}} \nabla T$ carried by normal quasiparticles. The normal quasiparticles are unpaired charge carriers that exist in superconductors at finite temperatures.

A requirement of the Meissner effect is that the total current in a bulk superconductor must be zero, $\vec{j} = \vec{j_{\mathrm{s}}} + \vec{j_{\mathrm{q}}} = 0$, which implies that the thermoelectric current is cancelled by a superconducting current $\vec{j_{\mathrm{s}}}$.

In order to measure the thermoelectric current in superconductors one must take advantage of the relationship between the supercurrent and the phase gradient of the superconducting condensate wavefunction, $\Psi_{\mathrm{s}}(\vec{r}) = (n_{\mathrm{s}}/2)^{1/2} e^{i\theta(\vec{r})}$. The supercurrent is described as $\vec{j_{\mathrm{s}}} = (e\hbar n_{\mathrm{s}}/2m)\nabla\theta(\vec{r})$ which, when combined with the aforementioned relation, $\vec{j_{\mathrm{s}}} = -\vec{j_{\mathrm{q}}} = \eta_{\mathrm{s}} \nabla T$ shows that a superconductor under the influence of a temperature gradient will create a phase difference $\Delta\theta = (2m\eta_s/e\hbar n_s)\Delta T$ across the region of superconductor that has a non-zero thermoelectric current, $\vec{j_q}$.

7.1 Principles Behind Thermoflux Determination

To observe the thermoelectric effect in superconductors a bimetallic loop is used. Two superconductors with different gap energies are connected in order to form a single closed superconducting loop. A circulating supercurrent, I_{cs}, is established within the superconducting penetration depth, $\Lambda(T)$, which generates a thermoelectric magnetic flux $\Phi_{Th} = \mathcal{L}I_{cs}$ through the loop where $\mathcal{L}$ is the self-inductance of the bimetallic loop. As the bimetallic loop is a closed superconducting circuit, Ginzburg-Landau theory states that the wavefunction must be single valued, thus setting the requirement that the flux through the loop must be quantized. The total flux through the bimetallic loop is then $\Phi_2 = \Phi + \Phi_{Th} = k\Phi_0$, where $k = 0, \pm1, \pm2, \cdots$, are the number of flux quanta, $\Phi_0 = h/2e$ trapped in the loop, and Φ is the applied magnetic flux.

To measure the flux through the bimetallic loop an optimised hybrid interferometer was fabricated to surround the bimetallic loop. This allows read-out of the flux through the device. A schematic of the device is shown in Figure 7.1.

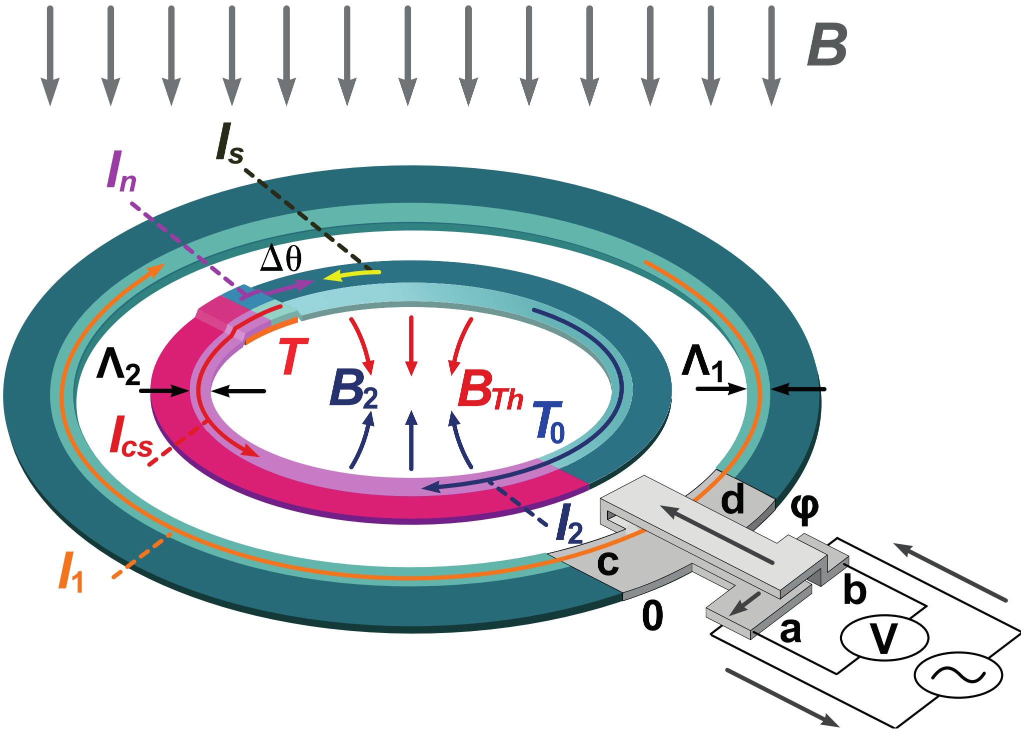

Figure 7.1: Schematic of the experimental structure for thermoflux measurements. The bimetallic loop is placed in a temperature gradient which results in a quasiparticle current I_n and counter-flowing supercurrent I_s. This causes a phase gradient $\Delta\theta$ that causes a circulating current I_cs to flow within the $\Lambda(T)$-layer of the loop. The circulating current thus generates a thermoelectric magnetic field and subsequently a thermoelectric flux component. Image courtesy of E. Matrozova [114].

As discussed in the previous chapter the hybrid interferometer takes advantage of the Andreev reflection mechanism to infer the phase difference between points c and d on the image. The phase difference between c and d is related to the measurable resistance between a and b by,

$$R = R_0 - r\cos\varphi \tag{7.1}$$

The phase difference φ is a function of the total flux through the interferometer loop, $\varphi = 2\pi\Phi_1/\Phi_0$. One must now take account of all the contributions to this total flux from both the interferometer (measuring) loop and the bimetallic loop.

The formulae that follow were derived in [115]. The total flux is given by,

$$\Phi_1 = BA_1 - \mathcal{L}_1 I_1 - M(I_2 + I_{\mathrm{cs}}), \tag{7.2}$$

where B is the externally applied magnetic field, A_1 is the area of the measuring loop, $I_1 = I_{\mathrm{c1}} \sin(2\pi\Phi_1/\Phi_0)$ is the Josephson screening current circulating in the measuring loop with a proximity induced critical current I_{c1}. I_2 is the Meissner current circulating in the bimetallic loop. $\mathcal{L}_1$ and $\mathcal{L}_2$ are the self-inductances of the measuring and bimetallic loops respectively and M is the mutual inductance between the two loops. It should be noted that information gained from the experiments detailed in Chapter 6 allowed for an optimised design of the measuring loop. In particular the loop and normal segment (between c and d) were made such that it would operate in the $\beta < 1$ regime (i.e. sinusoidal line-shape) without the need for additional dc current bias. This reduces the current being passed through the device and thus minimises sources of additional flux. A further optimisation of the device was achieved by folding the normal segment of the cross between a and b as depicted in Figure 7.1. This reduces any current-induced flux being directly coupled to the measuring loop.

The values of the magnetic field B are experimentally determined at the positions corresponding to $\Phi_1 = n\Phi_0$ which correspond to the extrema of resistance (as discussed in Section 6.1). Recall that the maxima occur at $n = (2m+1)/2$ and the minima occur at $n = 2m$ where $m = 0, \pm 1, \pm 2, \pm 3, \cdots$. As the inner loop is a closed superconducting loop and is subject to flux quantisation we can also write an equation describing the flux through the bimetallic loop,

$$\Phi_2 = BA_2 - MI_1 - \mathcal{L}_2 I_2 = k\Phi_0. \tag{7.3}$$

It is now clear that the measured position of extrema depend on both n and k - the position of extrema can now be defined as $B_{n,k}$.

As measurements are taken at the extrema, and it has already been stated that the experiment is in the $\beta < 1$ regime, a further simplification to the equations can be made. As $I_1 = I_\mathrm{c} \sin\left(2\pi\Phi_1/\Phi_0\right)|_{\Phi_1=\Phi_n} = 0$, the positions of the extrema are therefore independent of I_1 which can now be omitted from Equations 7.2 and 7.3 leading to the simplified definitions of the flux through each loop, in the absence of a temperature gradient,

$$\Phi_1 = B_{n,k}A_1 - MI_2 = n\Phi_0, \tag{7.4}$$

$$\Phi_2 = B_{n,k}A_2 - \mathcal{L}_2 I_2 = k\Phi_0. \tag{7.5}$$

To determine the circulating current in the bimetallic loop, I_2, we once again return to the flux quantisation requirement ($\Phi_2 = k\Phi_0$) which implies that $I_2 = (B_{n,k}A_2 - k\Phi_0/\mathcal{L}_2)$. By substituting I_2 into Equation 7.4 an expression for the measured values of $B_{n,k}$ can be written,

$$B_{n,k}\left(A_1 - \frac{M}{\mathcal{L}_2}A_2\right) + \frac{M}{\mathcal{L}_2}k\Phi_0 = n\Phi_0, \tag{7.6}$$

where $A = A_1 - (M/\mathcal{L}_2)A_2$ is the effective area of the measuring loop, therefore,

$$B_{n,k}A + \frac{M}{\mathcal{L}_2}k\Phi_0 = n\Phi_0. \tag{7.7}$$

7.1.1 The Influence of a Temperature Gradient

To investigate thermoelectric effects, one must be able to establish a temperature gradient across the device. A bifilar heater line is fabricated on the chip which allows local heating of one end of the bimetallic loop. This causes a temperature gradient through the bimetallic loop to appear. In addition, the average temperature of both the bimetallic loop and the measuring loops will increase. The temperature gradient induces the thermoelectric current I_{cs}, whilst the increased average temperature of the loops changes the superconducting penetration depth, $\Lambda(T)$. A result of the penetration depth change is that all the areas and inductances will also change and as such must be defined as $A', A'_1, A'_2, \mathcal{L}'_2$ and M'. The induced thermoelectric current must be taken into account leading to a new definition of the current through the bimetallic loop, $I'_2 = (B'_{n,k}A'_2 - k\Phi_0 + \Phi_{\mathrm{Th}})/\mathcal{L}'_2$. Although the total flux at the resistance extrema remains intact ($\Phi_1 = n\Phi_0$), the measured positions in magnetic field are now shifted to different values $B'_{n,k}$. Therefore, under the influence of a temperature gradient the measured positions are described by,

$$B'_{n,k}A' + \frac{M'}{\mathcal{L}'_2}(k\Phi_0 - \Phi_{\mathrm{Th}}) = n\Phi_0. \tag{7.8}$$

Although care was taken in the fabrication of the bifilar heater line there will always be some additional flux in the system generated by the heater current, $\Phi_{\mathrm{h}} = \mathrm{const}\cdot I_{\mathrm{h}}$. This term does not appear in any of the equations as it is easy to cancel this term by taking measurements at both positive and negative heater currents. Averaging these measurements simply cancels the heater flux term, $< \Phi_{\mathrm{h}} > |_{\pm I_{\mathrm{h}}} = 0$. Recall Equations 7.7 and 7.8 which describe the measured positions of extrema with and without a temperature gradient. The difference between the two values, $\Delta B_{n,k} = B_{n,k} - B'_{n,k}$ allows for a determination of the thermoelectric flux in the system. Using $B_0 = \Phi_0/A$ and rearranging Equation 7.7 we can now write the position of the extrema, $B_{n,k}$, normalised to the oscillation period B_0,

$$B_{n,k} = \frac{n\Phi_0}{A} - \frac{M}{\mathcal{L}_2 A}k\Phi_0, \tag{7.9}$$

$$\frac{B_{n,k}}{B_0} = n - \frac{M}{\mathcal{L}_2 A}k. \tag{7.10}$$

Similarly, Equation 7.8 describing the position of the extrema when a temperature gradient is present can also be rearranged and written normalised to B_0,

$$B'_{n,k} = \frac{n\Phi_0}{A'} - \frac{M'}{\mathcal{L}'_2 A'}(k\Phi_0 - \Phi_{\mathrm{Th}}), \tag{7.11}$$

$$\frac{B'_{n,k}}{B_0} = n\frac{A}{A'} - \frac{M'}{\mathcal{L}'_2}\frac{A}{A'}\left(k - \frac{\Phi_{\mathrm{Th}}}{\Phi_0}\right). \tag{7.12}$$

The difference $\Delta B_{n,k}/B_0 = (B_{n,k} - B'_{n,k})/B_0$ is subsequently given by,

$$\frac{\Delta B_{n,k}}{B_0} = \left(1 - \frac{A}{A'}\right) n - \left(\frac{M}{\mathcal{L}_2} - \frac{A}{A'}\frac{M'}{\mathcal{L}'_2}\right) k + \frac{A}{A'}\frac{M'}{\mathcal{L}'_2}\frac{\Phi_{\mathrm{Th}}}{\Phi_0}, \tag{7.13}$$

which can be stated as,

$$\frac{\Delta B_{n,k}}{B_0} = an - bk - c. \tag{7.14}$$

When there is no heater current and therefore no temperature gradient, Equation 7.13 describes the equation of a plane in 3D space where the x, y and z coordinates correspond to n, k and $\Delta B_{n,k}/B_0$ respectively.

7.1.2 Experimental Structure for Thermoflux Measurements

The preceding sections have emphasised some of the basic theory and equations describing the experimental set-up. It is clear now that for the experiment to take place the sample must contain a bimetallic ring in which the thermoelectric current can flow, a means of establishing the temperature gradient through the ring and a separate measuring loop, the hybrid interferometer. All of the equations discussed so far rely on the ability to vary the magnetic flux through the devices. In our experimental set-up this can be achieved by varying the field coarsely using a large superconducting solenoid, however the majority of measurements take advantage of the fine field tuning afforded by an on-chip antenna. Finally, in order to probe the temperature of the bimetallic loop and thus determine the temperature gradient applied, an SNS thermometer is also present on the chip. These five components are fabricated on a single chip in a multi-layer nano-fabrication process.

The bimetallic loop is made out of two superconductors with differing superconducting gaps, lead and aluminium. The superconducting transition temperatures of the two materials are also different, $T_{\mathrm{c}}^{\mathrm{Al}} \simeq 1.2\,\mathrm{K}$ and $T_{\mathrm{c}}^{\mathrm{Pb}} \simeq 7.2\,\mathrm{K}$. This ensures that the concentrations of normal quasiparticles in the lead part of the loop is negligible in the range of temperatures investigated (0.25 - 1 K). In order to establish a temperature gradient across the loop a bifilar normal metal (silver) wire was fabricated on the chip connected to a T-shaped silver wire which is connected to the top contact of the bimetallic loop. The thermometer was also connected to the hot spot of the heater, at the same distance as the heater-bimetallic loop distance.

The final sample is shown in a false colour scanning electron micrograph shown in Figure 7.2. The electron-beam lithography was done in five separate layers. The first layer made of 50 nm of silver contains the bottom layer of the interferometer cross, the normal component of the thermometer and the bottom layer of the heater lines. The second layer is a 30 nm spacer layer made of silicon monoxide. It is required to insulate the top and bottom layers of the folded components such as the bifilar heater and the interferometer cross as well as allowing the heater line to be separated from the interferometer loop. The third layer, again made of 50 nm of silver, finalises the interferometers normal cross and bifilar heater line. The fourth layer is made of 70 nm of aluminium and forms the superconduting measuring loop, one half of the bimetallic loop and the superconducting contacts of the SNS thermometer. The final layer, 150 nm of lead, is used to make the remaining half of the bimetallic loop and to provide a fine field tuning source in the form of an on-chip superconducting antenna. The area of the measuring loop and bimetallic loop are defined as $A_1 = 377\,\mu\text{m}^2$ and $A_2 = 171\,\mu\text{m}^2$ respectively.

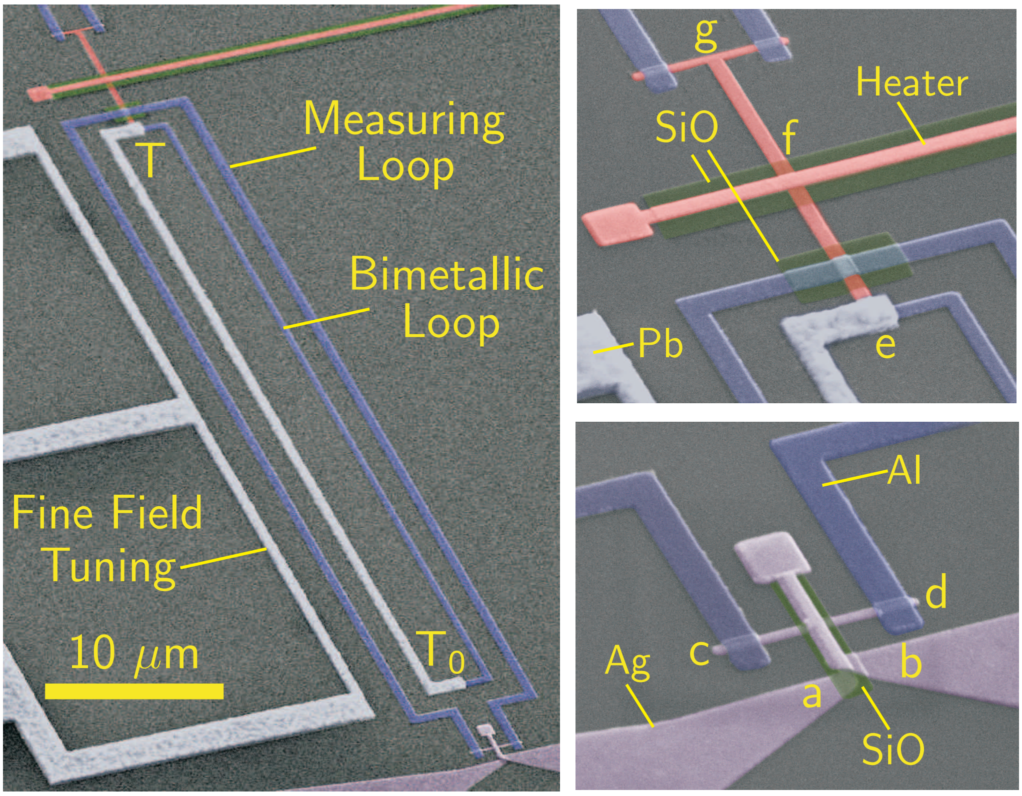

Figure 7.2: (left) False colour scanning electron micrograph of the bimetallic loop coupled to a bifilar heater and hybrid quantum interference device. The bimetallic loop is made of two different superconductors (aluminium and lead). The hybrid quantum interference device is used as a measuring loop and is made of aluminium. Fine field tuning is provided by the on-chip antenna made of lead. (top right) shows the bifilar heater (f) in close proximity to both the top contact of the bimetallic loop (e) and the SNS thermometer (g). The temperature T at (e) is measured by the thermometer at (g). (bottom right) highlights the hybrid quantum interferometer cross in a folded geometry. The phase difference between c and d is determined by the resistance measured between a and b. The false colouring is used to differentiate different materials and components. Insulating pads between different metallic layers, which are made of silicon-monoxide, can be seen in green.

7.2 Investigation of the Influence of Temperature Gradient on the Resistance Oscillations

7.2.1 Wide Range Field Measurements

Before measurements of $\Delta B_{n,k} = B_{n,k} - B'_{n,k}$ are undertaken, measurements of the oscillations as a function of the large superconducting solenoid are taken. This allows one to determine the range of magnetic fields available and the linearity of the oscillations. Figure 7.3 (top left) shows a large number of oscillations (> 100) measured by sweeping the large solenoid. Figure 7.3 (top right) shows the zoomed-in measurement exhibiting sinusoidal line-shape magnetoresistance oscillations. Finally, Figure 7.3 (bottom) shows the value of the magnetic field recorded at the peak of each oscillations. A fit is applied showing the linear relationship between the peak number (which corresponds to n) and the magnetic field. The period of oscillations is calculated from the fit to be 5.96 μT. Using the areas of the loops, A_1 and A_2, one can calculate to effective area of the system to be $A_{\text{eff}} = 342.8\,\mu\text{m}^2$. Using $B_0 = \Phi_0/A_{\text{eff}}$ the expected period is calculated to be $B_0 = 6.03\,\mu\text{T}$ which is in excellent agreement with the measured value from the linear dependence.

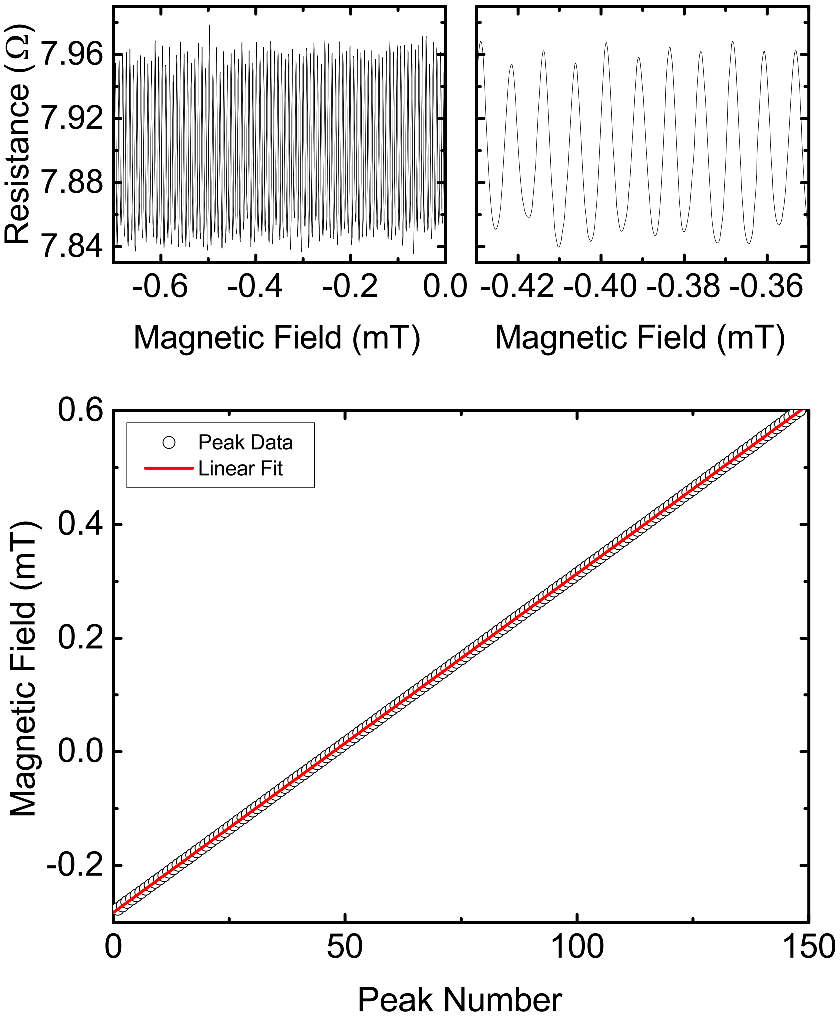

Figure 7.3: (Top Left) shows a large range of magnetoresistance oscillations obtained by sweeping the large field superconducting solenoid. (Top right) shows a smaller range of oscillations taken with the superconducting solenoid. The sinusoidal line-shape and periodicity is clearly seen. (Bottom) shows the detected peak position in magnetic field plotted against the peak number. A fit to the data shows a linear relationship between the magnetic field and the peak number n. The magnetic field period obtained from this data is $B_0 = 5.96\,\mu$T which is in excellent agreement with that calculated from the loop areas.

7.2.2 Measurement of Flux Contributions: $\Lambda(T)$-effect

As discussed in the background section, previous published measurements of thermoflux failed to account for the temperature dependent penetration depth, the $\Lambda(T)$-

effect. The measurement technique used in this experiment aims to remedy this oversight. In addition to separating the $\Lambda(T)$-effect from the measurement, one must also be in full control of the number of flux trapped inside the loop (this point was highlighted in Ref [13]). The remainder of the experiment is done using the on-chip fine field source which provides access to approximately 6-7 oscillations. The on-chip source can be more accurately and quickly controlled than the large superconducting solenoid which is generally used for much higher magnetic fields

Thermoflux is expected to add or subtract from the flux through the bimetallic loop when a temperature gradient is applied. This would be detected as a small shift in the oscillation as a function of the applied magnetic field when compared to the measured oscillation when no temperature gradient is applied across the system. It is evident that there are a number of effects present when a temperature gradient is applied to the bimetallic loop which can mask or confuse actual detection of a thermoflux signal.

Measurement of the device is achieved by measuring a sweep of five oscillations with the fine field source. Each measurement is recorded as a triplet: one sweep with zero applied heater current, one with positive applied heater current, and finally, one with negative applied heater current. The triplet of sweeps are measured a number of times (> 25) to reduce the signal-to-noise ratio. During analysis the positive and negative sweeps are averaged together to remove any stray heater-line flux as discussed in Section 7.1.1. The resulting data consists of a set of oscillations at zero heater current and a set of oscillations at a finite heater current. An example of the two sets of oscillations are shown in Figure 7.4. The finite heater current sweep shows a clear shift when compared to the zero current data however it is not a constant shift across the entire sweep; the period of the oscillations are also altered, which is a signature of $\Lambda(T)$-effect.

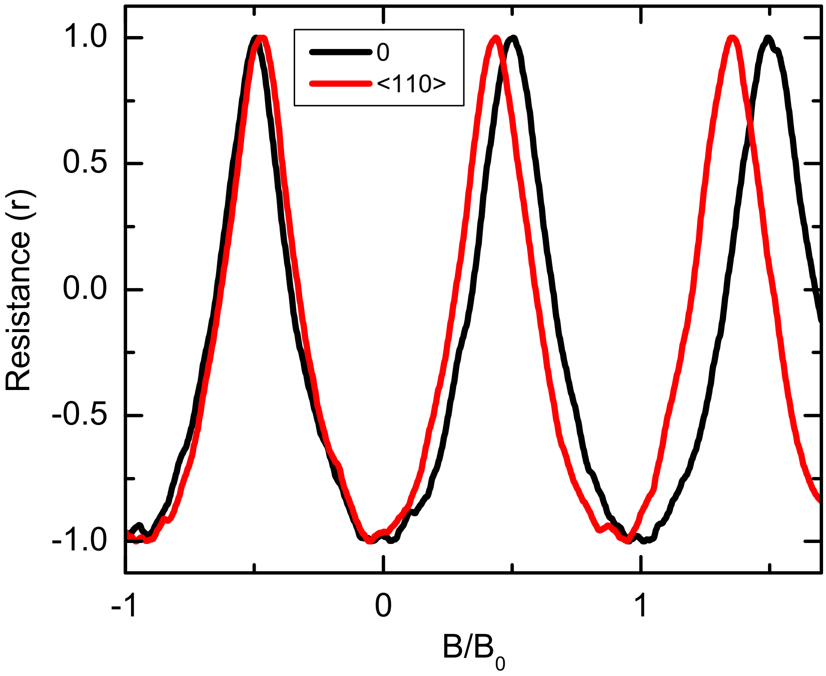

Figure 7.4: Graph showing the change to the period of oscillations when a heater current (110 μA) is applied.

To perform the analysis the maxima and minima for each oscillation in the data set are determined approximately using a peak detection algorithm, `peakdet.m` [116] in order to separate each oscillation. The 'center' of the oscillation is then defined by finding the midpoint at every resistance level. The array of midpoint values is then recorded and averaged. The difference between midpoints of the zero heater current set and the finite heater current set are defined as the peak shift. Figure 7.5 shows an example of the difference between midpoints of each peak in the series of five oscillations.

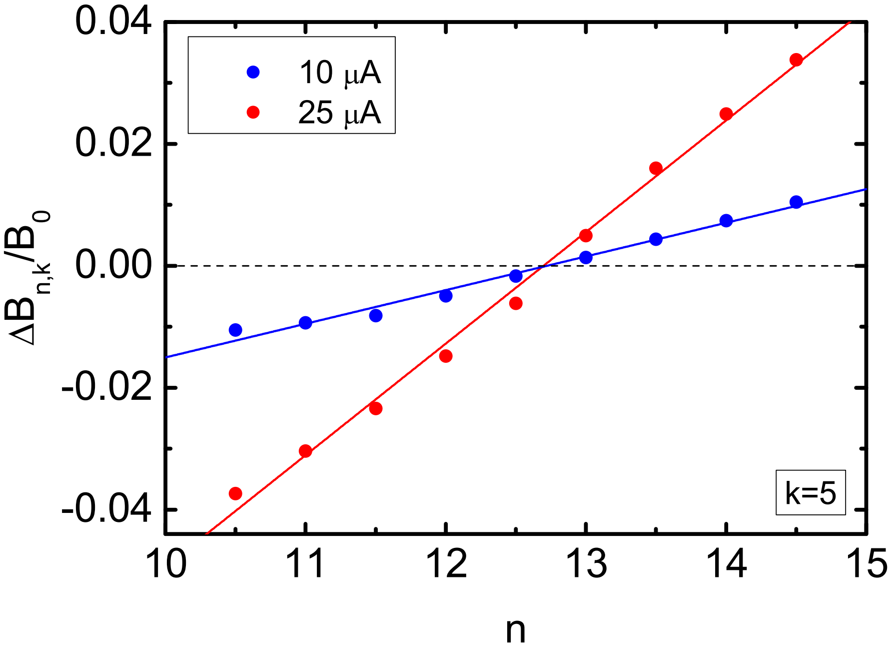

Figure 7.5: Peak shift as a function of n (at constant k). Each data point describes the difference between the zero-heater peak and the finite-heater peak. Due to the change in period caused by $\Lambda(T)$ there is a finite gradient associated with the measurement. A linear fit to each data set shows that the gradient increases as the applied heater current increases - this is expected due to a higher average temperature of the system.

The shift in period due to $\Lambda(T)$-effect is evident in the data points shown in Figure 7.5. Two measurements are shown at different heater currents, 10 and 25 μA. As the change in period is directly related to the temperature dependent $\Lambda(T)$-effect it is expected that a greater effect will be observed with higher heater currents, which increase the average temperature across the device. A linear fit is applied to each set of data which shows a distinct difference in the gradient of the slope. The gradient of the fit describes the first term on the right hand side of Equation 7.13,

$$a = \left(1 - \left(\frac{A}{A'}\right)\right). \tag{7.15}$$

It is directly related to the change in $\Lambda(T)$ as the heater current (and thus temperature) is varied.

7.2.3 Controlling the Trapped Flux Quantum Number by Thermocycling

An important part of this experiment is being able to have control over the number of trapped flux, $k\Phi_0$, through the bimetallic loop where $k = 0, \pm1, \pm2, \pm3 \cdots$. The number of trapped flux within the loop is dependent on the magnetic environment whilst the loop is cooled through its transition temperature. For example, if the sample is cooled through T_c with zero external magnetic field applied the bimetallic loop will trap a number of flux close to the magnitude of the residual geomagnetic field.

A number of the previous experiments claiming to present results of thermoflux failed to account for the number of trapped flux in their loops. This can result in very large values of thermoflux that are actually including other effects such as $\Lambda(T)$-effect contributions and finite trapped fluxes, $k\Phi_0$. Pegrum *et al* [13] state that in order to see true thermoelectric flux, one would want only a small number of trapped flux in the bimetallic loop, ideally zero.

In the work presented here we take advantage of our on-chip heater to raise and lower the sample through its superconducting transition. When the sample is heated to the normal state the magnetic field is tuned to a pre-calculated value. With the field held constant the heater is turned off and the loop is lowered back through its transition point allowing the magnetic flux to be trapped inside the loop. The field required to trap an addition flux quantum is easily calculable from the area of the bimetallic loop. Using the formula $\Phi_0 = BA$ it is possible to change the number of trapped flux in the bimetallic loop in steps of Φ_0.

During this manipulation the heater current is raised to a relativiely high value of 1 mA. Figure 7.6 shows a portion of the measurement of the resistance through the interferometer loop as the heater current is ramped to 1 mA. There is a sudden jump in the resistance as the bimetallic loop lets an additional Φ_0 in. When the heater current is subsequently reduced allowing the bimetallic loop to become superconducting once again the resistance remains changed, indicating an altered number of trapped flux through the bimetallic loop.

Figure 7.7 shows a set of oscillations after subsequent thermocycling operations. Each set of oscillations represent a sweep where an additional $k\Phi_0$ has been trapped in the bimetallic loop. It is clear that changing the number of flux trapped through the loop changes only the phase of the oscillations leaving the period intact. The shift ΔB of the extrema is consistent with Equation 7.7 such that $\Delta B = (M/\mathcal{L}_2)(\Phi_0/A)$ which is independent of n. The value of $M/\mathcal{L}_2$ can be determined for the shift and is equal to 0.2, this value agrees well with that calculated. The value of $M/\mathcal{L}_2$ is of importance and will be used later to calculate the absolute value of thermoflux.

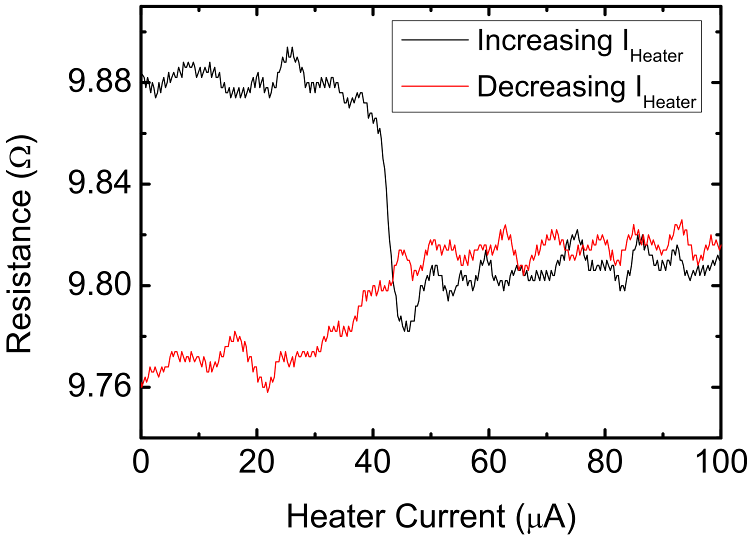

Figure 7.6: Measurements taken during a typical 'thermocycling' operation. The magnetic field is swept to a specific position using the antenna current. Once at the desired magnetic field the heater current is ramped up to 1000 μA (Only 0-100 μA range shown in figure) which raises the bimetallic loop above its transition temperature allowing flux to freely enter the loop. The heater current is then ramped back down to zero - as the loop cools through its transition point the flux is trapped inside the loop. By repeating this process at different magnetic fields it is possible to alter the number of flux quanta trapped in the loop on a one-by-one basis (see Figure 7.7).

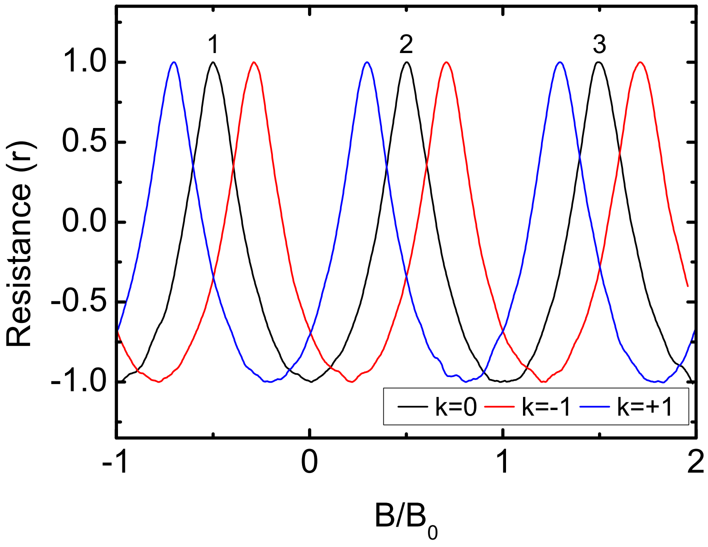

Figure 7.7: Magnetoresistance oscillations showing that the number of $k\Phi_0$ through the loop can be manipulated by thermocycling the system at different pre-calculated magnetic fields. The numbers 1 to 3 labelled above the oscillations refers to each cluster of three oscillations. This is the n number which does not change with k.

A measurement of the $\Delta B/B_0$ vs k at a constant n reveals how the peak shift varies as the number of flux trapped through the loop is changed using the thermocycling method. An example of this measurement is shown in Figure 7.8. A linear fit shows that the data is only dependent on the heater current through the system and is independent of both n and k. In this case the gradient of the fit describes the second term on the right hand side of Equation 7.13,

$$b = \left(\frac{M}{L_2} - \frac{A}{A'} \frac{M'}{L'_2} \right) . \tag{7.16}$$

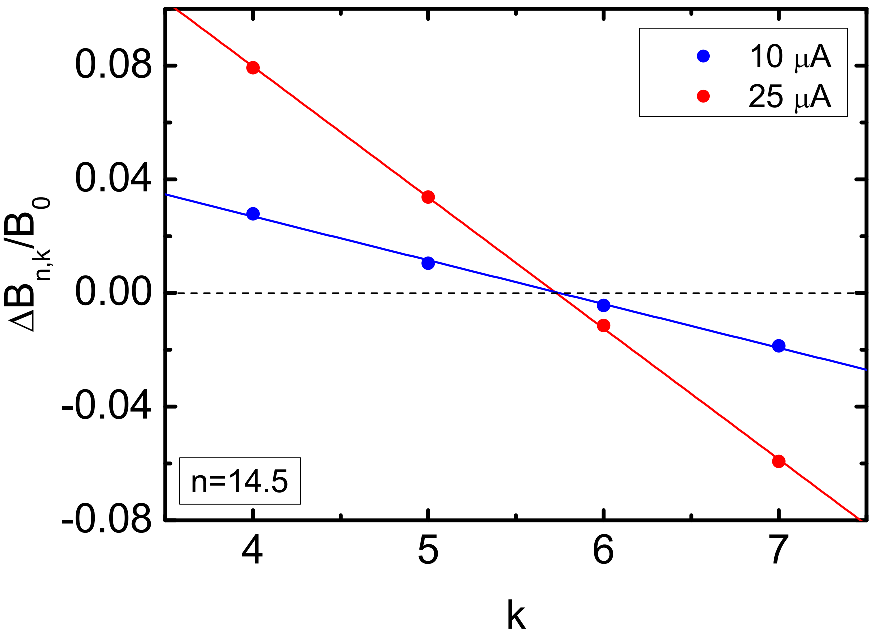

Figure 7.8: Peak shift as a function of k (at constant n). Each data point describes the difference between the zero-heater peak and the finite-heater peak.

7.2.4 The Separation of Thermoflux Contribution

From Equation 7.14, the final contribution, defined as c, describes the shift attributed to the thermoflux. As the thermoflux serves only to shift the points along the $\Delta B_{n,k}/B_0$ axis by the same value one can define a reference plane,

$$\frac{\Delta B^{R}_{n,k}}{B_0} = an - bk, \tag{7.17}$$

where a and b are the gradients already experimentally determined. The plane essentially gives the value of the contribution of the $\Lambda(T)$-effect to the values of $\Delta B_{n,k}/B_0$ that are measured. The reference plane is constructed for the four heater currents of interest in Figure 7.9.

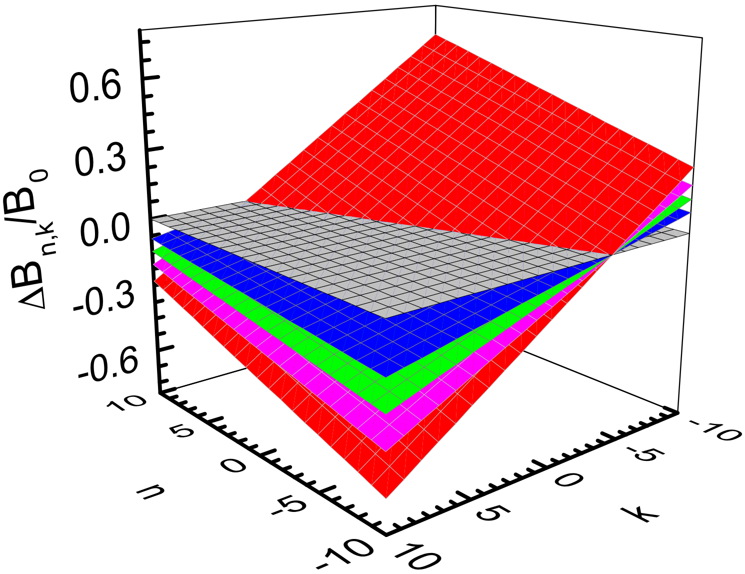

Figure 7.9: Calculated reference planes defined by Equation 7.17 for a number of different applied heater currents. The gradients a and b are experimentally determined values from measurements of peak shift vs n (at constant k) and measurements of peak shift vs k (at constant n). The final term in Equation 7.14 is associated with thermoflux and results in a shift of the plane.

In the unique situation that $n = k = 0$ the measured plane cuts the $\Delta B_{n,k}/B_0$ axis at $\Delta B_{0,0}/B_0$. In this case the value of thermoflux $\Phi_{\mathrm{Th}} = (\mathcal{L}_2/M)(\Delta B_{0,0}/B_0)$ can be immediately determined. However, it is possible to calculate the value of Φ_{Th} over a wide range of n and k values and then determine the value of c from the difference between the reference plane and the measured plane;

$$c = \frac{(\Delta B_{n,k} - \Delta B^R_{n,k})}{B_0} = \frac{A}{A'}\frac{M'}{\mathcal{L}'_2}\frac{\Phi_{Th}}{\Phi_0}. \tag{7.18}$$

Measuring c over a wide range of n and k means that Φ_{Th} can be averaged over a large set of data and thus determined more precisely. After averaging the value of thermoflux is given as,

$$\Phi_{\mathrm{Th}} \approx \langle c(\mathcal{L}_2/M)\Phi_0\rangle. \tag{7.19}$$

Note that the component A/A' is ignored as it accounts for only $\approx 1\%$ of the value of c. Now that it is clear how to separate the $\Lambda(T)$-effects from the genuine thermoflux signal it is advantageous to perform the experiment close to the line of intersection between the zero heater current plane and the finite heater current plane, i.e. when $\Delta B^R_{n,k} \simeq 0$. This is achieved by using the fine field source and the thermocycling procedure. Figure 7.10 shows a measurement of five oscillations ($5\,n$ values), each taken with a different number of trapped flux, k, in the system.

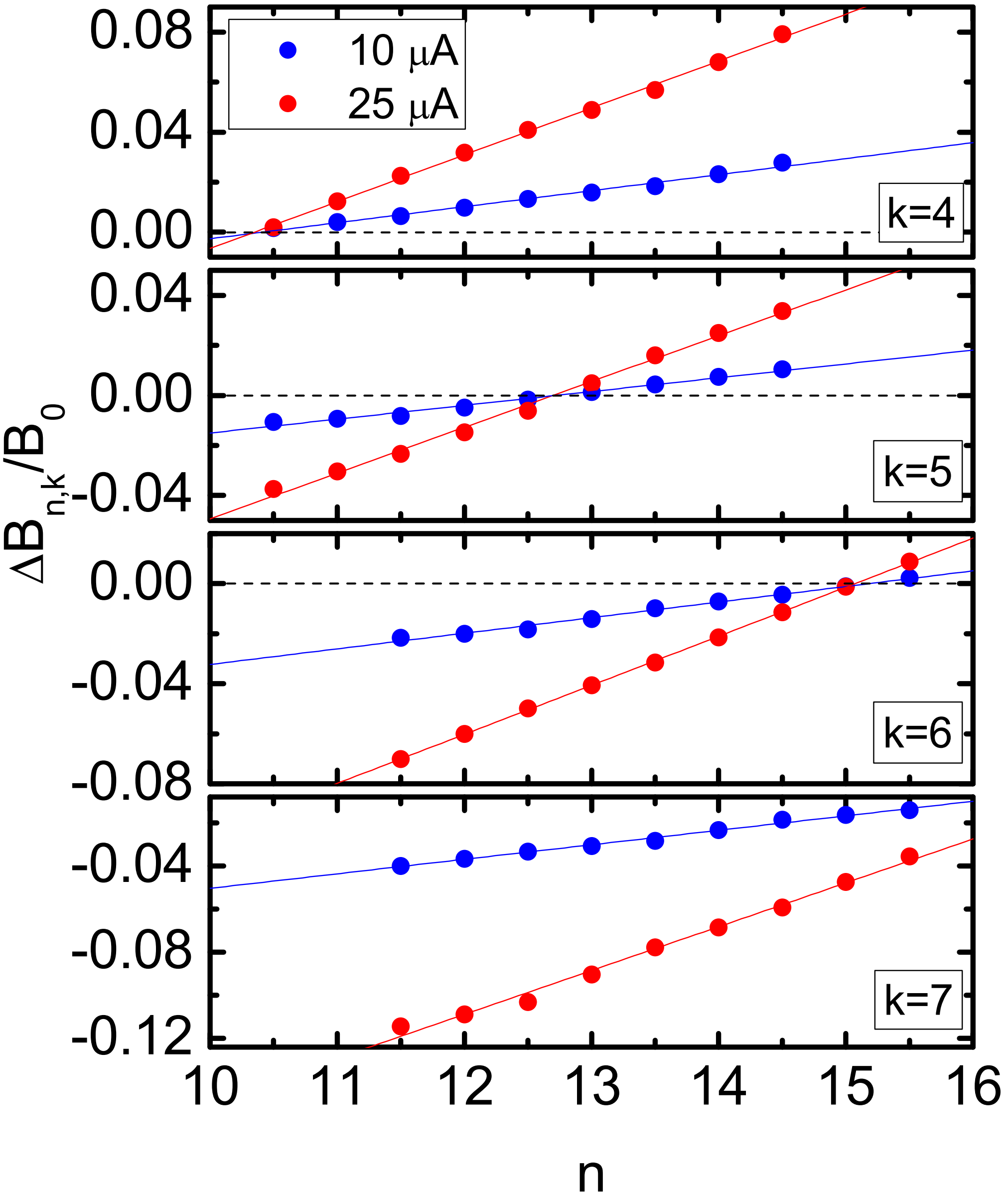

Figure 7.10: Peak shift vs n at four successive values of k. Note that the mimimal values of $\Delta B_{n,k}/B_0$ shift as k is varied. This graph also highlights that the gradient a is independent of the number of flux (k) trapped in the bimetallic loop.

From each graph (at each k) in Figure 7.10 the minimal value of $\Delta B_{n,k}/B_0$ are chosen, representing where the $\Lambda(T)$-effect is minimal. A graph of the minimal $\Delta B_{n,k}/B_0$ values plotted against $s = 2.5k/n$ is shown in Figure 7.11. It is important to note that in this case n is not constant.

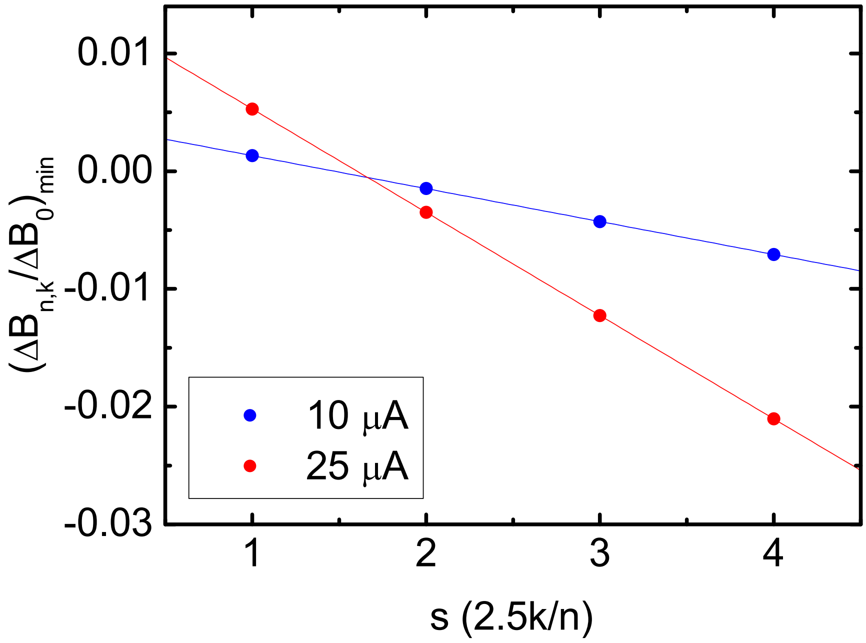

Figure 7.11: Minimal peak shift values taken as a function of $s = 2.5k/n$. Note that n is not constant in this plot.

Using the measured values of a and b, one can now calculate the corresponding reference points (at the correct values of n and k) to compare with the measured $(\Delta B_{n,k}/B_0)_{\min}$. Both sets of points, measured and reference values, are plotted on the same graph as shown for $I_{\mathrm{h}} = 25\,\mu\mathrm{A}$ in Figure 7.12.

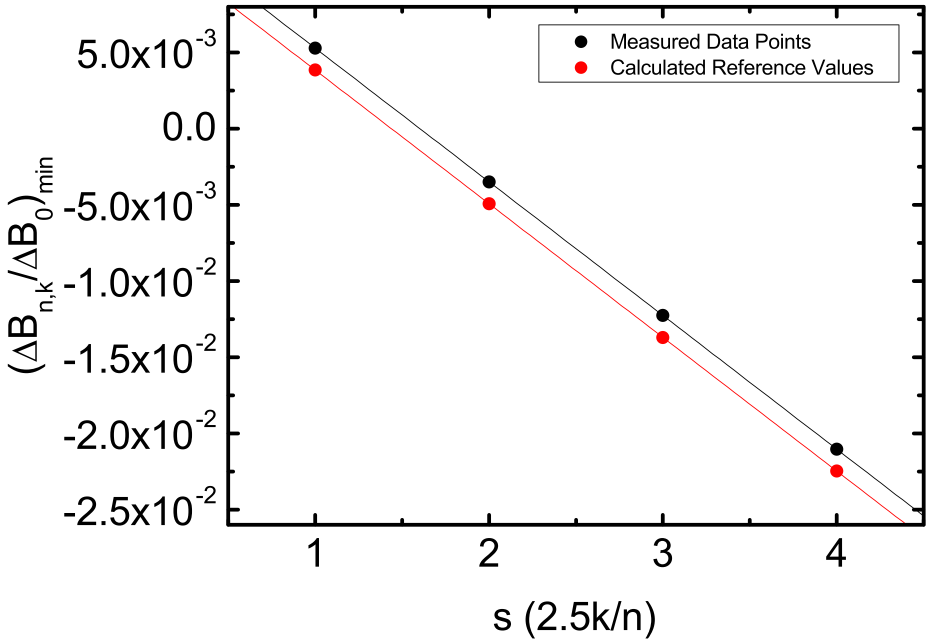

Figure 7.12: Measured data points representing the minimal values of $\Delta B_{n,k}/B_0$ as a function of k for $I_{\text{Heater}} = 25\ \mu$A. The difference between the two linear fits is equal to c, as defined by Equation 7.19.

The difference between the two points is simply the value of c. A linear fit is then applied to each of the lines showing clearly the constant difference between the two sets of data. By subtracting the linear fit of the reference data from measured values gives directly the value of $c = (\Delta B_{n,k} - \Delta B^R_{n,k}/B_0)$. The method is repeated for the remaining heater currents of interest, 10, 15 and 20 μA and is shown in Figure 7.13. It is clear from the figure that as the heater current is increased, so too is the thermoflux contribution c, note that the value of c is independent of both k and n. As we expect a larger heater current to provide a larger temperature gradient, the result is of the expected dependence.

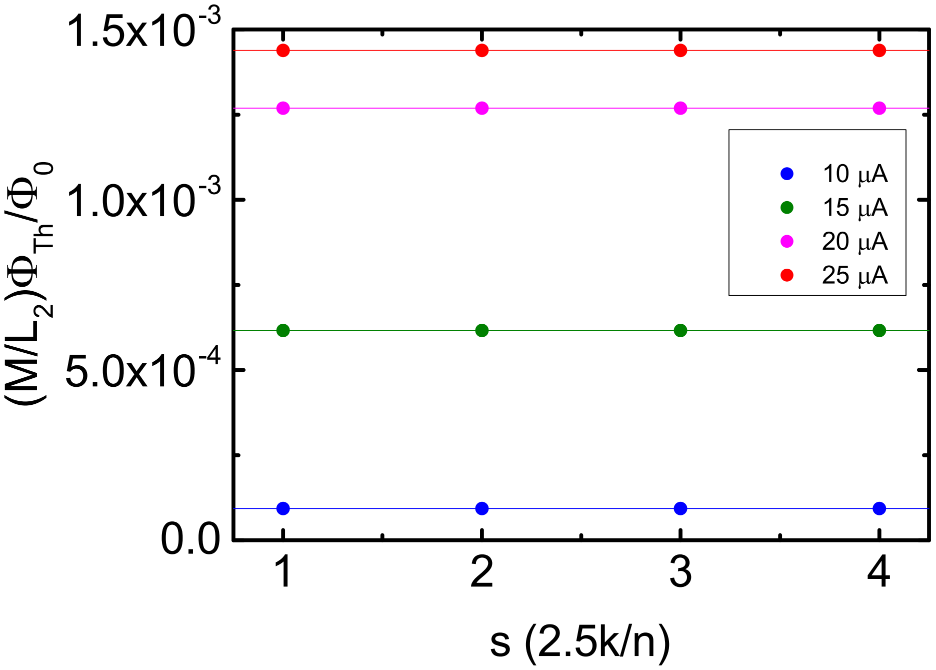

Figure 7.13: Measured data points after subtraction of calculated reference values.

An important test of a genuine thermoelectric flux measurement is to see if the direction of the flux changes when the sign of the temperature gradient is reversed. A second device was fabricated with a mirror reversal of the aluminium and lead layers in the bimetallic loop. Exchanging the position of the two superconducting metals is equivalent to reversing the direction of the temperature gradient and thus the circulating thermoelectric current. The measurement and analysis method already detailed in this chapter for the first sample was repeated for the mirrored device. The experimentally determined values of $c = \frac{M}{L_2}\frac{\Phi_{\mathrm{Th}}}{\Phi_0}$ for the mirrored device are shown in Figure 7.14. The identically performed experiment shows that the mirrored device gives a reversed value of c. Once again the effect increases with applied heater current and thus larger temperature gradient. At the highest heater current used (I_{heater}=25 μA) the measured value of the thermoflux was $\Phi_{\mathrm{Th}} \approx 10^{-2}\Phi_0$.

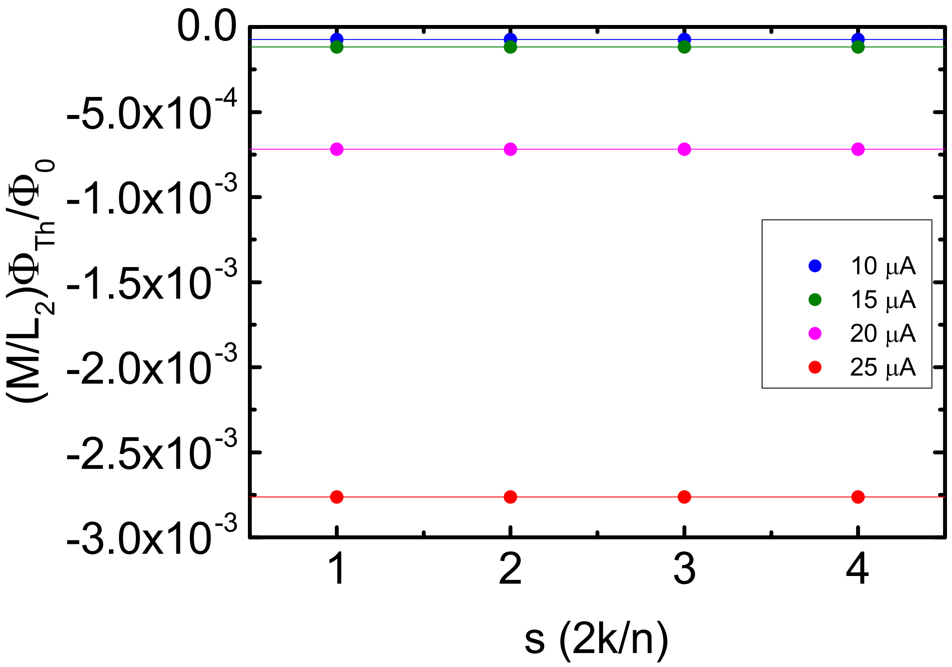

Figure 7.14: Measured data points after subtraction of calculated reference values for the mirrored device.

7.3 Comparison with Theory

7.3.1 Thermometry

The previous section detailed the experimental method and the required analysis to show that application of a heater current to the bimetallic loop results in an additional contirbution to the flux through the loop, the thermoflux. So far we have only discussed the results in terms of the heater current applied, not the temperature gradient. In order to determine the temperature gradient across the bimetallic loop it is necessary to investigate the temperatures in the system under an applied heater current. As the top contact of the loop is directly connected to the heater wire, it is obvious that this is the 'hot' contact. As mentioned previously a proximity SNS junction is connected to the other side of the heater wire at the same distance as the top loop contact. Differential resistance ($\mathrm{d}V/\mathrm{d}I$) measurements are taken at a range of applied heater currents to show the dependence as the temperature of the contact is increased. As the loop contact and thermometer are equidistant from the hot point of the heater wire it is expected that the thermometer gives a good approximation to the temperature of the hot contact of the bimetallic loop. In order to calibrate this thermometer it is necessary to also perform $\mathrm{d}V/\mathrm{d}I$ measurements as a function of the bath temperature. Figure 7.15 shows that the characteristics of the $\mathrm{d}V/\mathrm{d}I$ measurement change as a function of applied heater current. It can be seen from the lower heater current values that the critical current, I_{c}, and the retrapping current, I_{r}, can be of very different values. The value of interest is the $\mathrm{d}V/\mathrm{d}I$ zero bias position which is sensitive to both heater current and temperature. The measurement taken with respect to bath temperature (Figure 7.16) also show a sensitivity of the zero bias position. It is this position that can be calibrated between the two to provide a temperature reading of the top contact of the bimetallic loop. Note that the measurements at different temperatures were taken whilst the cryostat was cooling. The temperature stated for each curve refers to the measured bath temperature at the mid-point of the measurement, the zero bias position.

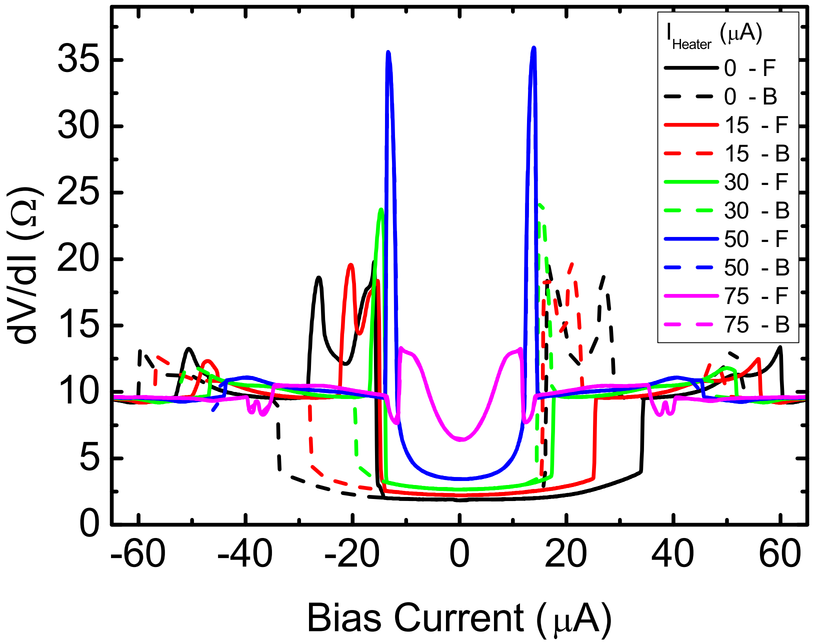

Figure 7.15: Differential resistance ($\mathrm{d}V/\mathrm{d}I$) measurements of the SNS thermometer taken at different heater currents. Solid lines show measurement sweeps taken in the left to right (forwards) direction, dashed lines show sweeps taken in the right to left (backwards) direction.

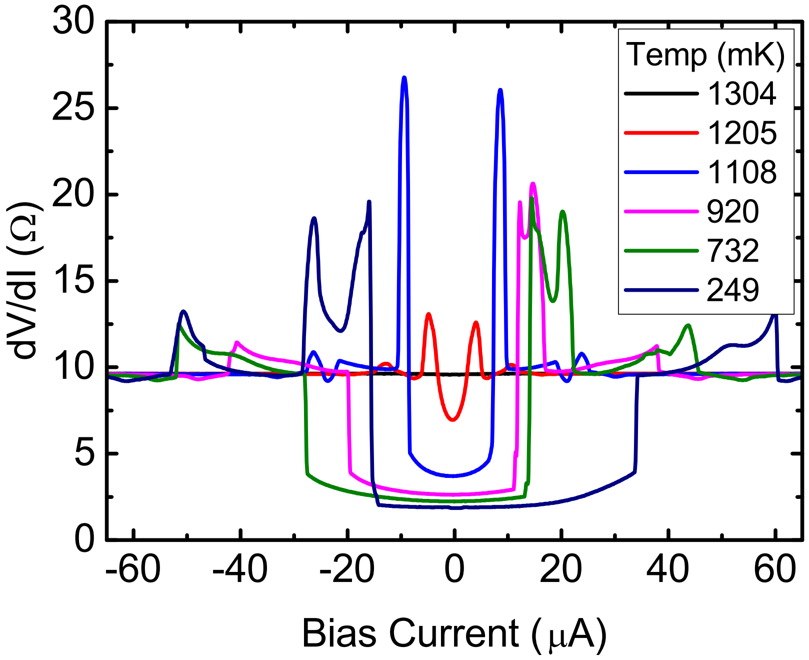

Figure 7.16: Differential resistance (dV/dI) measurements of the SNS thermometer taken at different bath temperatures. Some measurements were taken in a left to right direction and some vice versa. This was to ensure minimal non-measuring time was wasted as the fridge was continuously cooling. Note that each sweep took approximately 4 minutes. Stated temperatures are those of midway through the sweep - close to the zero bias point.

The bottom contact of the bimetallic loop is the 'cold' contact. The temperature difference between this contact and the top contact define the temperature gradient which drives the thermoelectric current. Due to no remaining free contacts on the chip it was not possible to directly measure the temperature using a SNS thermometer as was done for the upper 'hot' contact. In order to infer the temperature of the contact the Andreev interferometer oscillations were measured as a function of the bath temperature as well as at a range of different heater currents. Due to the close proximity of the 'cold' contact and the Andreev interferometer it is expected that any large temperature changes at the 'cold' contact will be observed as a reduction of the Andreev interferometer oscillation amplitude. Figure 7.17 shows that the amplitude of the resistance oscillations reduce as the bath temperature is raised. The corresponding oscillations as a function of the heater current (Figure 7.18) applied to the 'hot' contact show minimal change to the amplitude. Even at the highest heater currents, 110 μA, the inferred temperature is around 300 mK. The heater current range of interest in this investigation is 0 to 25 μA which show minimal change of temperature ($\simeq +30$ mK). Figure 7.19 shows the temperature scale providing estimated temperature values for the 'hot' and 'cold' contacts. It is clearly seen that applying a heater current shows a large response in the temperature of the 'hot' contact reaching temperatures close to 900 mK at 25 μA. The 'cold' contact remains relatively unaffected by the application of a heater current remaining under 300 mK over our range of interest (up to 25 μA), only reaching 300 mK at very high heater currents of 110 μA. The difference between the temperatures of the two contacts implies that a heater current does indeed establish a temperature gradient across the bimetallic loop.

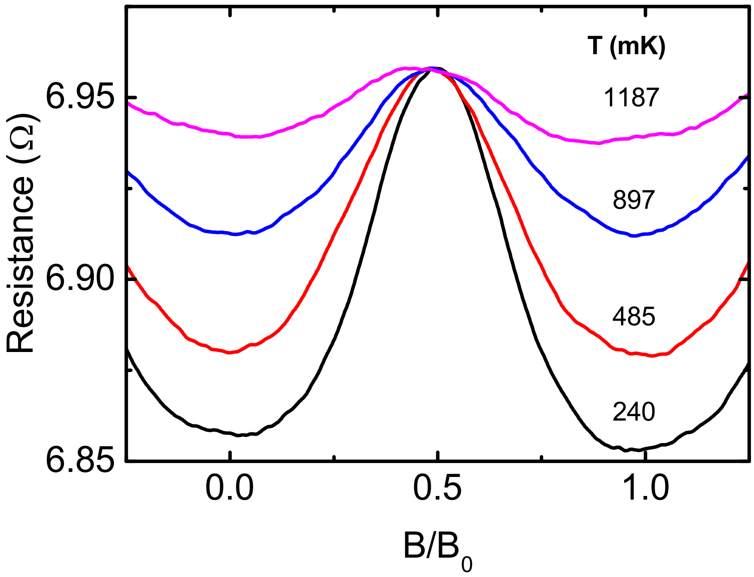

Figure 7.17: Andreev interferometer oscillations as a function of the bath temperature. There is a clear reduction of the amplitude as the bath temperature approaches the aluminium transition temperature.

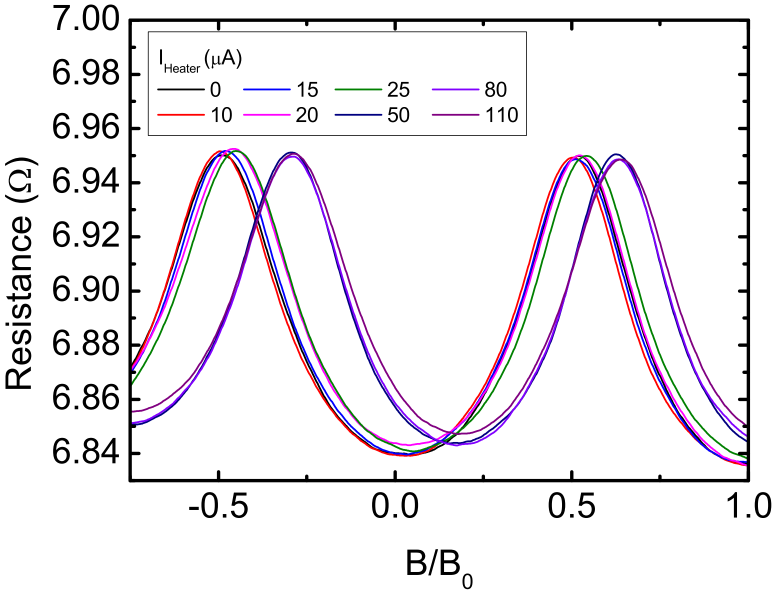

Figure 7.18: Andreev interferometer oscillations as a function of the heater current applied to the ‘hot’ contact. There is no change to the amplitude in the range of heater currents important to measurements in this investigation (0 to 25 μA). Even at high heater currents of 110 μA only small reductions of amplitude are observed corresponding to an inferred temperature of $\simeq$ 300 mK.

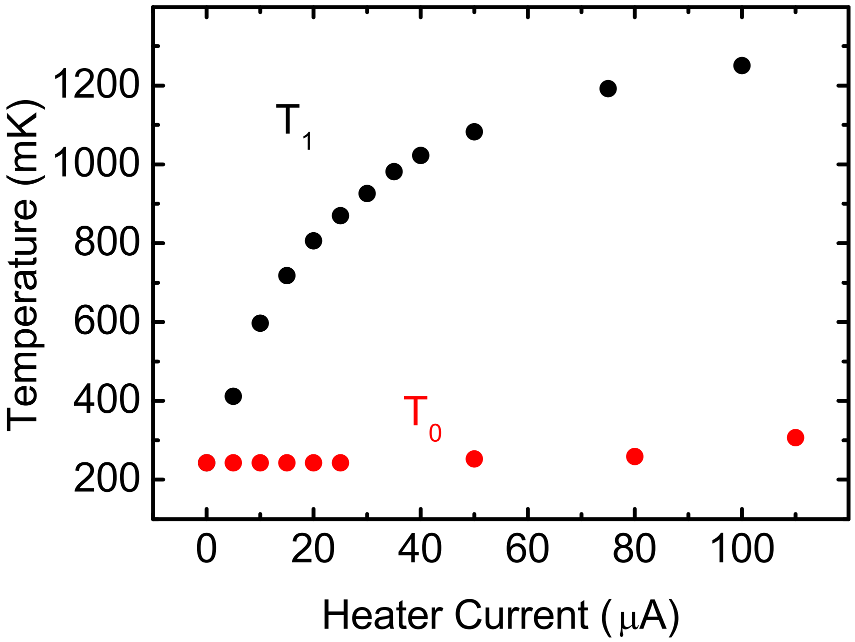

Figure 7.19: Temperatures corresponding to an applied heater current for the top and bottom contacts of the loop. Temperatures for the 'hot' contact are measured by $\mathrm{d}V/\mathrm{d}I$ of thermometer connected directly to the contact. Temperatures for the bottom contact are inferred by measuring the temperature dependence of the magnetoresistance oscillations of the Andreev cross.

7.3.2 Calculation of the Circulating Current

As discussed previously the thermoelectric flux is related to the circulating current around the loop $\Phi_{\mathrm{Th}} = \mathcal{L}_2 I_{\mathrm{cs}}$. The circulating current is subject to the current conservation requirement that $I_{\mathrm{n}}(x) + I_{\mathrm{s}}(x) = I_{\mathrm{cs}} = const$, where $I_{\mathrm{n}}(x) = S j_{\mathrm{q}}$ is the thermoelectric current and $I_{\mathrm{s}}(x)$ is the counter-flowing supercurrent component. S is the cross-sectional area of the aluminium wire of the bimetallic loop, x is the distance from the hot contact of the loop. Recall that $j_{\mathrm{q}} = -\eta_{\mathrm{q}} \nabla T$ where ∇T can now be written as $\frac{dT_{\mathrm{q}}}{dx}$ such that,

$$j_{\mathrm{q}} = -\eta_{\mathrm{q}} \frac{dT_{\mathrm{q}}}{dx} = -\sigma_{\mathrm{q}} \alpha_{\mathrm{q}} \frac{dT_{\mathrm{q}}}{dx}, \tag{7.20}$$

where σ_q, α_q and T_q are the electrical conductivity, the thermopower and the temperature of the quasiparticles respectively.

In order to calculate the circulating current in the system the technique given by Gurevich *et al* [22] is used whereby the total energy of the bimetallic loop is minimized. The total energy of the bimetallic loop is given by including two energy contributions, the first describes the kinetic energy of the superconducting electrons in the aluminium, $W_\mathrm{k} = \frac{1}{2}I_\mathrm{s}^2(x)\mathcal{L}_\mathrm{k}(x)$. The second term is the energy of the magnetic field created by the circulating current, $W_\mathrm{m} = \frac{1}{2}I_\mathrm{cs}^2\mathcal{L}_2$; $\mathcal{L}_\mathrm{k}$ is the kinetic inductance. $I_\mathrm{s}(x)$ is the supercurrent which counter-flows the thermoelectric current, $I_\mathrm{n}(x)$, in the aluminium wire. The total current in the aluminium wire $I_\mathrm{n}(x) + I_\mathrm{s}(x)$ must be equal to the current I_cs in the lead wire in order to satisfy the current conservation $I_\mathrm{n}(x) + I_\mathrm{s}(x) = I_\mathrm{cs} = const$, where x is the distance from the hot contact of the bimetallic loop. Calculating the total energy,

$$W = \int_0^{l_0} \frac{\mathrm{d}W_{\mathrm{k}(x)}}{\mathrm{d}x}\mathrm{d}x + W_\mathrm{m}, \tag{7.21}$$

and taking into account the current conservation and the requirement that each current must be continuous across the cold interface at $x = l_0$: $I_\mathrm{n}(l_0) = 0$, $I_\mathrm{s}(l_0) = I_\mathrm{cs}$, the total energy is given by,

$$W = \frac{1}{2}(I_\mathrm{cs} - I_\mathrm{n}(0))^2\mathcal{L}_\mathrm{k}(0) - \frac{1}{2}I_\mathrm{cs}^2\mathcal{L}_\mathrm{k}(l_0) + \frac{1}{2}I_\mathrm{cs}^2\mathcal{L}_2. \tag{7.22}$$

Minimizing the energy with respect to the circulating current, and solving the equation,

$$\frac{\mathrm{d}W}{\mathrm{d}I_\mathrm{cs}} = (I_\mathrm{cs} - I_\mathrm{n}(0))\mathcal{L}_\mathrm{k}(0) - I_\mathrm{cs}\mathcal{L}_\mathrm{k}(l_0) + I_\mathrm{cs}\mathcal{L}_2 = 0, \tag{7.23}$$

results in the circulating current being given as,

$$I_\mathrm{cs} = \frac{I_\mathrm{n}(0)\mathcal{L}_\mathrm{k}(0)}{\mathcal{L}_2 + \delta\mathcal{L}_\mathrm{k}}, \tag{7.24}$$

where $\delta\mathcal{L}_\text{k} = \mathcal{L}_\text{k}(0) - \mathcal{L}_\text{k}(l_0)$. Combining Equation 7.24 with the definition $I_\text{n}(x) = S\vec{j_\text{q}}$ where j_q is given by Equation 7.20, the thermoflux can be defined as,

$$\Phi_\text{Th} = -\eta_\text{q}(0)S\frac{\mathrm{d}T_\text{q}}{\mathrm{d}x}\frac{\mathcal{L}_2\mathcal{L}_\text{k}(0)}{\mathcal{L}_2 + \delta\mathcal{L}_\text{k}} \tag{7.25}$$

7.3.3 Heat Flow through the Aluminium Wire

One must now consider the quasiparticle heat flow through the aluminium wire of the bimetallic loop. The heat flow through the aluminium wire is given by Fourier's law [117] of heat transport,

$$Q_\text{q} = \kappa_\text{q}S\frac{\mathrm{d}T_\text{q}}{\mathrm{d}x} \tag{7.26}$$

where κ_q is the thermal conductivity.
To calculate the heat flow in the aluminium wire one must consider the rate at which the quasiparticles gain energy in the wire and the rate at which the quasiparticles transfer energy to the phonon system. The following equation describes these two components, the former on the left hand side and the latter on the right hand side,

$$-\frac{\mathrm{d}}{\mathrm{d}x}\left(\kappa_\text{q}S\frac{\mathrm{d}T_\text{q}}{\mathrm{d}x}\right)\mathrm{d}x = \Sigma S(T_\text{q}^n - T_\text{p}^n)\mathrm{d}x, \tag{7.27}$$

where Σ is the electron-phonon coupling constant [118] and n is the exponent of the electron phonon relaxation [119]. The value of n is determined by the relationship between the electron mean free path l and the phonon wavelength λ_p. The phonon wavevector is given by,

$$q_\text{p} = \frac{2\pi}{\lambda_\text{p}} \approx \frac{k_\text{B}T}{\hbar\nu_\text{s}} \tag{7.28}$$

where $\nu_\text{s} \approx 5 \times 10^3\,\text{ms}^{-1}$ is the velocity of sound. The mean free path in our aluminium films is roughly 10 nm. This results in $q_\text{p}l < 1$ at temperatures less than 1 K. In this case our films are described by the disordered limit and subsequently the exponent of the electron-phonon interaction is given by $n = 6$ [118]. Integration of Equation 7.27 over the length of the aluminium wire, l_0, whilst taking into account that the quasiparticle heat flow at the cold interface must be zero yields,

$$\kappa_{\mathrm{q}}(0)\left.\frac{\mathrm{d}T_{\mathrm{q}}}{\mathrm{d}x}\right|_{x=0}=l_0\langle\Sigma(T_{\mathrm{q}}^n-T_{\mathrm{p}}^n)\rangle. \tag{7.29}$$

Typically the temperature of the quasiparticles is higher than the temperature of the phonon system $T_{\mathrm{p}}<T_{\mathrm{q}}$. In thin films of thickness $h<\lambda_{\mathrm{p}}$ the Kapitza resistance (thermal resistance) between the wire-substrate interface is negligible. This means that the phonon temperature is very close to the bath temperature T_0 [120]. Therefore $(T_{\mathrm{q}}^6-T_{\mathrm{p}}^6)\rightarrow T_{\mathrm{q}}^6$. The parameters η_{q}, κ_{q} and Σ depend on the quasiparticle concentration [7, 121]. As the temperature is reduced it is expected that the quasiparticle concentration also drops. The values are connected with their normal-state counterparts such that $\eta_{\mathrm{q}}=\eta_{\mathrm{n}}G(x)$, $\kappa_{\mathrm{q}}=\kappa_{\mathrm{n}}G(x)$ and $\Sigma=\Sigma_{\mathrm{n}}G(x)$ where $G(x)$ is calculated in Ref [7, 122] as,

$$G(x)=\frac{3}{2\pi^2}\int_x^{\infty}\frac{y^2\mathrm{d}y}{\cosh^2(y/2)}, \tag{7.30}$$

where $x=\Delta(T_{\mathrm{q}})/k_{\mathrm{B}}T_{\mathrm{q}}$; $\Delta(T_{\mathrm{q}})$ is the superconducting gap.

The thermal conductivity is related to the electrical conductivity by the Wiedemann-Franz law $\kappa_{\mathrm{n}}=\sigma_{\mathrm{n}}L_0T_{\mathrm{q}}$ where $L_0=2.4\times10^{-8}\,\mathrm{V}^2\mathrm{K}^{-2}$ is the Lorenz number [123] and σ_{n} is the normal-state electrical conductivity. Thermoflux is thus given by the following formula,

$$\Phi_{\mathrm{Th}}=-\alpha_{\mathrm{n}}\Sigma_{\mathrm{n}}Sl_0\langle T_{\mathrm{q}}^6G(T_{\mathrm{q}})\rangle\frac{1}{L_0}\frac{\mathcal{L}_2\mathcal{L}_{\mathrm{k}}(0)}{\mathcal{L}_2+\delta\mathcal{L}_{\mathrm{k}}}. \tag{7.31}$$

From Equation 7.31, it is implied that the thermoelectric flux is proportional to the effective inductance of the loop and the thermoelectric current. The thermoelectric current is related to the quasiparticle heat flow as discussed above. In order to compare Equation 7.31 with the experiment, three important temperatures must be discussed. The temperature $T_{\mathrm{q}}(0)$ of the hot end of the bimetallic loop is inferred from the SNS thermometer. The dependence of the average temperature $\langle T_{\mathrm{q}}\rangle$ on the heater current is inferred from the $\Lambda(T)$-effect dependence. By plotting the relative change in area $\Delta A/A$ as a function of both temperature and heater current, as shown in Figure 7.20, a corresponding average temperature $\langle T_{\mathrm{q}} \rangle$ can be determined. As discussed in Section 7.3.1, T_0 is determined from sensitivity of the interferometer oscillations to the bath temperature. All three temperatures $T_{\mathrm{q}}(0)$, $\langle T_{\mathrm{q}} \rangle$ and T_0 are plotted in Figure 7.21; it is seen that $T_{\mathrm{q}}(0)$ and $\langle T_{\mathrm{q}} \rangle$ differ by approximately 50 mK.

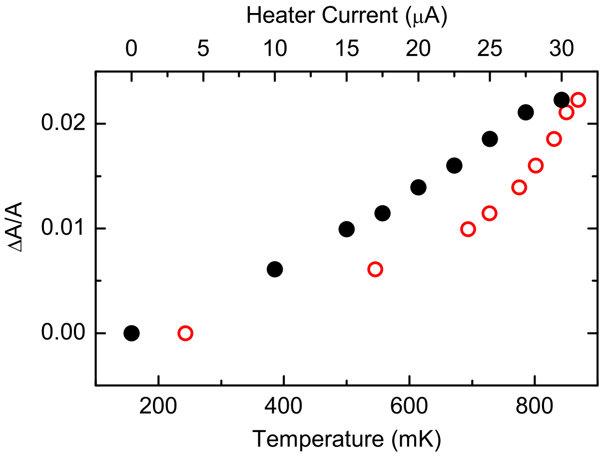

Figure 7.20: The relative change of the effective area as a function of both temperature (red, open circles - bottom axis) and heater current (black, solid circles - top axis). Using the effective area change, one can find the correspondence between the heater current applied and the average temperature $\langle T_{\mathrm{q}} \rangle$ and T_0.

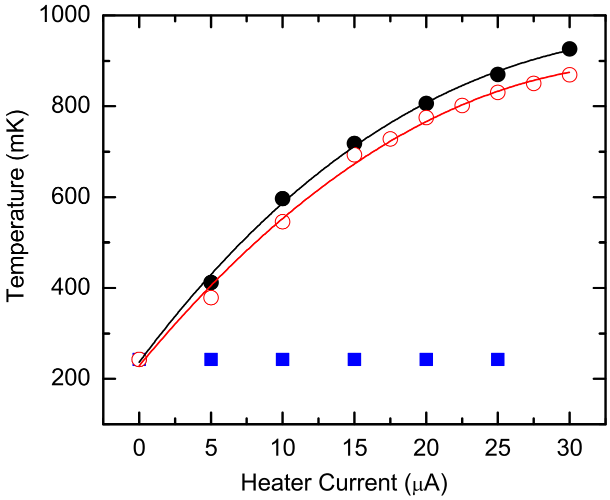

Figure 7.21: The three temperatures of interest $T_{\mathrm{q}}(0)$, $\langle T_{\mathrm{q}} \rangle$ and T_0 shown as a function of the heater current. $T_{\mathrm{q}}(0)$ (black, solid circles) is determined from the SNS thermometer measurements. $\langle T_{\mathrm{q}} \rangle$ (red, open circles) is determined from the correspondence between the relative change of the effective area as a function of temperature and heater current, as shown in Figure 7.20. T_0 (blue squares) is inferred from change in amplitude of the Andreev interferometer oscillations when a heater current is applied - note that over the range of interest (up to 25 μA) this value is unchanged from base temperature. The fit lines are constructed by interpolating the data and are intended as a guide to the eye only. The difference between $T_{\mathrm{q}}(0)$ and $\langle T_{\mathrm{q}} \rangle$ over the range of interest is approximately 30-50 mK.

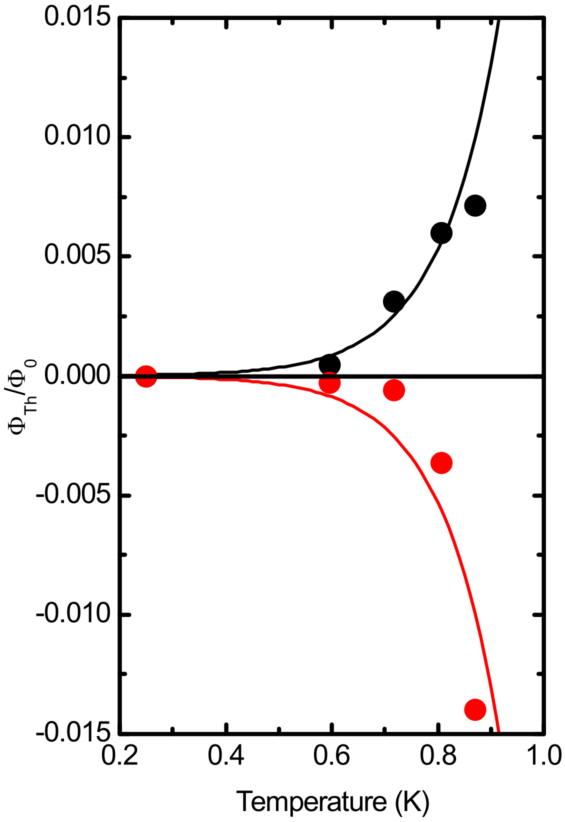

Figure 7.22: Measured thermoflux values at different hot spot temperatures for two samples with different temperature gradient directions. The curve is given by the Equation 7.31 in the text.

The final dependence of the thermelectric magnetic flux vs temperature $T_q(0)$ for both samples is shown in Figure 7.22. The theoretical curves are calculated using the formula given in Equation 7.31. The parameters used are the calculated inductance of the bimetallic loop $\mathcal{L}_2 = 1 \times 10^{-10}\,\mathrm{H}$, the measured cross-sectional area of the aluminium wire, $S = 6 \times 10^{-14}\,\mathrm{m}^2$, the measured length of the aluminium wire, $l_0 = 47 \times 10^{-6}\,\mathrm{m}$ as well as the thermopower, $\alpha_n \approx 2 \times 10^{-8}\,\mathrm{V\,K}^{-1}$, and the electron-phonon coupling $\Sigma \approx 5\times10^{10}\,\mathrm{W\,m}^{-3}\,\mathrm{K}^{-6}$, both of which are close to measured values available in the literature [118, 124]. It is assumed that $\langle T_q^6 G(T_q)\rangle \approx \langle T_q\rangle^6 \langle G(T_q)\rangle$; this is a valid assumption for an even temperature distribution. From Equation 7.29, the temperature gradient at the hot contact can be estimated as $5\times10^4\,\mathrm{K\,m}^{-1}$, which implies that the temperature reduces steeply from $T_q(0)$ to $\langle T_q\rangle$ over a distance of approximately 1 μm. Therefore $\delta x \approx (T_\mathrm{q}(0) - \langle T_\mathrm{q} \rangle)/(\mathrm{d}T_\mathrm{q}/\mathrm{d}x) \ll l_0$.

The kinetic inductance is calculated by taking into account the strong critical current suppression in the aluminium wire at the hot contact in close proximity to the silver wire. Test structures of Al/Ag sandwiches showed critical currents of order 1 μA; as a reduced critical current occurs at the hot contact it is considered to be a Josephson weak link interrupting the bimetallic loop. The kinetic inductance of a weak link is given by $\mathcal{L}_k(0) = \Phi_0/2\pi I_\mathrm{c}(0)$ [67]; the critical current at the hot end is described by $I_\mathrm{c}(0) = I_0(1 - T_\mathrm{q}/T_\mathrm{c})$ where $T_\mathrm{c} = 1.15\,\mathrm{K}$ for our device. The fitting parameter used in Figure 7.22 is I_0=6 μA - excellent agreement with theory is shown. As all other values in Equation 7.31 are either experimentally measured or taken from literature the final fit shown in Figure 7.22 is considered to have only one free fitting parameter - I_0.

7.4 Summary

The experiment presented in this chapter uses a single-chip that contains the entire experimental device; the hybrid interferometer, the bimetallic loop, a heater, a thermometer and an antenna for fine-field tuning. The control of single $k\Phi_0$ through use of a thermocycling technique is presented. Complete control over both k and n allow accurate experimental determination of gradients a and b, which in turn allow reference values to be calculated. The reference values are compared to the measured values which allow separation of the genuine thermoelectric magnetic flux from spurious $\Lambda(T)$-effects - the experimental methods and the analysis techniques are fully discussed. The circulating current in the system and the heat flow through the aluminium half of the bimetallic loop are used to determine the thermoelectric magnetic flux. The measured value of the thermoflux is shown to be in excellent agreement with the theory presented here.

CHAPTER 8

Conclusion

8.1 Conclusion

The primary aim of this project was to investigate the possibility of thermoelectric effects being present in superconductors as first proposed by Ginzburg [14]. The particular geometry used in this project is that of the bimetallic superconducting ring which was previously investigated by a number of different groups in the 1970s and 1980s [9–11, 13]. A “thermoelectric paradox” arose as the experimental results agreed neither with one another or the theory; sometimes in discrepancy with the theoretical values by up to five orders of magnitude. A possible reason for such variation in the results obtained by different groups, and correspondingly, the lack of agreement with theory was suggested to be due to thermoelectric effects being masked by other concomitant effects.

One of the possible masking effects is due to the number of flux quanta trapped inside the loop and the change in measured flux if additional flux is added or removed. All of the previous experiments referenced above used large scale bimetallic loops; a typical loop area would be 25 mm^2. A magnetic field of the order of the residual geomagnetic field ($\approx 50\ \mu$T) is enough to trap 6×10^5 flux quanta within the superconducting loop.

A second effect that masks the detection of the thermoelectric flux is the temperature dependence of the superconducting penetration depth, $\Lambda(T)$. Due to the change in the penetration depth with temperature, a sample's effective area will change under the influence of an applied heat. It is also important to note that the previous experiments all used a SQUID based read-out technique with the SQUID situated away from the bimetallic loop. This necessitates the use of a coupling wire which, in turn, can trap additional flux. The redistribution that arises due to the $\Lambda(T)$-effect can also register a change in flux if the SQUID is not properly coupled to the bimetallic loop.

During this project we have used the nano-fabrication facilities available at Royal Holloway's clean room. Using electron-beam lithography we have been able to make structures with much smaller loop sizes than those reported in previous works. A typical size of our superconducting loops is 200 μm^2. As a comparison to the macroscopic loops discussed above our loops will trap only a small number (≈ 6) of flux quanta when subject to the residual geomagnetic field.

To address the issue of having to use a coupled SQUID situated far away from the bimetallic loop, as per previous work, we have successfully fabricated a hybrid interferometer on the same chip, fully enclosing the bimetallic loop. This ensures that no region of the bimetallic loop will be uncoupled to the hybrid interferometer measuring loop. This eliminates any thermoelectric flux 'false positives' caused by a redistribution of flux as a result of the $\Lambda(T)$-effect. Again, the interferometer loop is of a similar area to the bimetallic loop (400 μm^2).

The requirements of the hybrid interferometer are that it must operate at its optimal working point with minimal, ideally zero, additional bias current. The mode of operation must be free from hysteresis when the applied magnetic field is swept back and forth. In addition, all possible causes of flux noise should be reduced to a minimum. In order to ensure that the hybrid interferometer could satisfy the above criteria and act as an appropriate read-out device for our thermoflux experiment a number of investigations were carried out. Initial experiments involved single SNS junctions in which the critical current of the junction could be measured as a function of varying other parameters. The first parameter varied was the length of the normal part (L_N) of the SNS junction, this is obviously a value that is fixed during the fabrication stage and thus a number of devices with different L_N were made. At a constant temperature of 240 mK, with identical measuring currents, it was observed that the critical current in the junction reduces as a function of L_N. This result was as expected due to the formula given by de Gennes [44] that predicts the relationship $I_\mathrm{c}(L) \propto \exp(-L/\xi_\mathrm{N})$. The fit of our experimental data to this theory showed excellent agreement. A more recent theory by Zaikin *et al* [45] was also fit to our data which showed reasonable agreement; however, the theory is only applicable in the 'long-junction' regime ($L > \xi_\mathrm{N}$) which some of our devices may not fall under. Using the same devices we were also able to investigate the effect of temperature on the critical current of the junctions. Again, we expected to see a reduction of the critical current as the temperature of the cryostat was increased. We fit the data to the simplified long-junction regime theory as per Ref [45]. It is not surprising that the theory is in better agreement with the data for the longer junctions.

Our devices were fabricated with an additional set of measurement leads which contact the normal junction perpendicularly at its center-point. This allowed us to apply an additional dc bias current to the device. A reduction in the critical current as the bias current was increased was observed; this was also expected from the theory discussed in Section 3.2.1.

The next set of devices fabricated joined the two superconductors with a superconducting wire to form a superconducting loop interrupted by a normal metal junction. A similar program of experiments to those described above were carried out. In this case the screening parameter $\beta \approx \mathcal{L} I_\mathrm{c}$ is important (see Section 3.2). As the inductance $\mathcal{L}$ is fixed during fabrication, β can be varied simply by varying the critical current. As the hybrid interferometer exhibits magnetoresistance oscillations we were interested to see how they were affected by varying β. It was observed that the oscillations could evolve through a number of states as the screening parameter was decreased (i.e., as the critical current was reduced). At low bias currents and low temperatures the oscillations were strongly-hysteretic as a result of the flux-phase relationship shown in Figure 6.2. As β is reduced the oscillations become non-hysteretic forming a cusp-like sinusoidal shape at $\beta \approx 1$. Further increase of the screening parameter saw the oscillations become increasingly sinusoidal. This evolution of line-shape was observed both as a function of temperature of the cryostat and as a function of the applied bias current.

To reduce flux noise in the loop due to coupling of the measuring current a new interferometer design was devised. In this design the perpendicular normal metal wire was folded back on itself with an insulating spacer placed between. This removed the measuring current from inside the measurement loop. The fabrication of this design was challenging as it was necessary to have precise alignment (≈100 nm) to ensure the two halves of the normal metal were in good contact.

As an aside to the main aim of optimising the interferometer for our purpose of thermoelectric flux detection, some of the novel properties of our test devices were investigated in their own right. Another set of the devices used to test the effect of an additional bias current were fabricated but one of the normal metal reservoirs was replaced with a superconducting reservoir of similar thickness. As the bias current was increased in these devices the critical current reduced as seen previously. Additional application of bias current, once the critical current had been suppressed, resulted in a reappearance of the critical current before, once again, becoming fully suppressed. This effect, known as the π-effect, is typically seen in devices with thick (hundreds of nanometers) normal metal reservoirs whereas the effect here is seen in a device with reservoirs only 50 nm thick; it is noted that the effect is only observed when one of the normal reservoirs is replaced with a superconductor. Although great care was taken to avoid operating the hybrid interferometer in the hysteretic regime during our thermoflux experiment a brief investigation was performed to investigate the behaviour of the device in this mode of operation. As the magnetoresistance oscillations exhibit a jump due to the unstable branch of the phase-flux relationship the interferometer may be used in a 'latching' detector regime. As there is such a large jump in resistance to a very small flux change the device can be initialised to a starting value and await an event that will shift the flux and subsequently measure a large change in the resistance value measured. This idea was tested during this project by using a multi-level flux pulse profile that initialised the system at a set point before applying a variable flux pulse that could tip the flux over the edge of the resistance drop. After the flux pulse is turned off the resistance of the system is remeasured. Due to the hysteresis in the magnetoresistance oscillations, if the flux pulse was sufficient to overcome the resistance drop then the system is considered to be in another state, it is not possible for the system to escape back into its initial state from this point. By varying the size of the flux pulse we were able to experimentally determine the fidelity of the read-out system.

With the aforementioned investigations providing a set of fabrication guidelines for our proposed thermoelectric effect device, we designed and fabricated a complex multi-layer sample containing all the necessary components on one chip. The bimetallic loop was designed using lead and aluminium and made to have a small area to avoid trapping large numbers of flux quanta at small magnetic fields. The bimetallic loop was surrounded by a hybrid interferometer measuring loop specifically designed to operate in the non-hysteretic regime without additional dc bias current. A heater and thermometer were also included on the same chip, as well as a lead antenna to provide a fine controllable magnetic field source. The reason for fabricating the entire sample on one chip is to avoid the need for coupling pick up coils, etc. that are inherent in the previous attempts at observing the thermoelectric flux.

During the experiment we were able to demonstrate excellent control over the number of flux quanta in the loop, moving them in and out of the loop one-by-one using a thermocycling operation. Using the magnetoresistance oscillations of the hybrid interferometer we were able to separate the genuine thermoelectric flux generated as a result of the applied temperature gradient from the $\Lambda(T)$-effects that are also present due to a raised average temperature of the bimetallic loop. As the previous measurements did not account for the out-of-control scatter of the number of trapped flux quanta, their observed effects are explained by a large $\Lambda(T)$-effect contribution that gives results in such large discrepancy with the theory.

Starting from the recently proposed technique for calculating the circulating current in the loop by means of minimizing the total energy of the system [22], we were able to theoretically deduce a formula for the circulating current in our system and subsequently the thermoelectric flux. We also show that it is important to consider the heat flow equations of the system to determine the value of the circulating current. We find that our experimentally determined value of the thermoelectric flux is in excellent agreement with the theory presented.

8.2 Further Work

Further work should be carried out investigating the range of geometries in which the novel π-effect can be observed. Varying the thickness of the reservoirs could give a lower limit at which the reappearance of a critical current will be observed. This result also deserves theoretical input to determine why the presence of the superconductor causes this effect and what similarities our design has to other measured devices.

The work presented in this thesis has shown that the hybrid interferometer is a device capable of being tuned (during fabrication, or in-situ) to operate at different working points. Although primarily used here in the sinusoidal regime, our proof-of-principle experiments of a latching read-out device are promising. As the device utilises a variable pulse profile to operate, the act of probing a device-under-test and the measurement of the interferometer state are separated. This could prove particularly useful in measurements of superconducting quantum circuits such as qubits as the back-action on the device would be minimal. This could serve to lower the effect of measurement on the decoherence of the qubit.

The methods used to separate the thermoelectric flux from masking $\Lambda(T)$-effects can be used to further explore thermoelectric phenomena in superconducting devices. An avenue for potential further work in this area is to test some of the recently published theories [125] that propose that a superconductor doped with magnetic impurities can result in an enhancement of the thermoelectric effect. If true, this effect would be observed using the techniques outlined in this thesis.

Bibliography

[1] Meissner, W. *Z. Ges. Kalte-Industrie*, **34**, 197 (1927).

[2] Borelius, G., Keesom, W. H., Johansson, C. H., and Linde, J. O. *Proc. Koninhl. Ned. Akad. Wetenschap*, **34**, 1365 (1931).

[3] Keesom, W. and Matthijs, C. *Physica*, **5**, 1 – 16 (1938).

[4] Casimir, H. and Rademakers, A. *Physica*, **13**, 33 – 40 (1947).

[5] Burton, E. F., Tarr, F. G. A., and Wilhelm, J. O. *Nature*, **136**, 141 (1935).

[6] Ginzburg, V. L. *Sov. Phys. JETP*, **14**, 177 (1944).

[7] Galperin, Y. M., Gurevich, V. L., and Kozub, V. I. *Sov. Phys. JETP*, **39**, 680 (1974).

[8] Garland, J. C. and van Harlingen, D. J. *Physics Letters A*, **47**, 423 – 424 (1974).

[9] Zavaritskii, N. V. *JETP Lett.*, **20**, 97 (1974).

[10] Falco, C. M. *Solid State Communications*, **25**, 419 (1978).

[11] van Harlingen, D. J. and Garland, J. C. *Solid State Communications*, **25**, 419 – 422 (1978).

[12] van Harlingen, D. J., Heidel, D. F., and Garland, J. C. *Phys. Rev. B*, **21**, 1842–1857 (1980).

[13] Pegrum, C. and Guénault, A. *Physics Letters A*, **59**, 393 – 395 (1976).

[14] Ginzburg, V. L. *Rev. Mod. Phys.*, **76**, 981–998 (2004).

[15] Matsinger, A., de Bruyn Ouboter, R., and van Beelen, H. *Physica B+C*, **93**, 63 – 74 (1978).

[16] Ioffe, A. *Semiconductor Thermoelements, and Thermoelectric cooling*, (Infosearch Ltd., 1957).

[17] Tilley, D. R. and Tilley, J. *Superfluidity and Superconductivity*, (Hilger, Bristol, England, 1990).

[18] Annett, J. A. *Superconductivity, Superfluids and Condensates*, (Oxford University Press, Oxford, UK, 2004).

[19] Meissner, W. and Ochsenfeld, R. *Naturwissenschaften*, **21**, 787–788 (1933).

[20] Schmidt, V. *The Physics of Superconductors: Introduction to Fundamentals and Applications*, (Springer, 1997).

[21] Shoenberg, D. *Superconductivity*, (University Press, 1960).

[22] Gurevich, V. L., Kozub, V. I., and Shelankov, A. L. *The European Physical Journal B - Condensed Matter and Complex Systems*, **51**, 285–292 (2006).

[23] Kozub, V. I. *Sov. Phys. JETP*, **47**, 178 (1978).

[24] Kozub, V. I. *Sov. Phys. JETP*, **61**, 1095 (1985).

[25] Galperin, Y. M., Gurevich, V. L., Kozub, V. I., and Shelankov, A. L. *Phys. Rev. B*, **65**, 064531 (2002).

[26] Abrikosov, A. *Fundamentals of the theory of metals.* Fundamentals of the Theory of Metals, (North-Holland, 1988).

[27] Lynton, E. *Superconductivity*, (John Wiley & Sons 1971).

[28] Guénault, A. M. and Webster, K. A. *J. Phys. Colloques*, **39**, C6–539 (1978).

[29] Brandt, E. H. and Clem, J. R. *Phys. Rev. B*, **69**, 184509 (2004).

[30] Hao, L., Macfarlane, J. C., Gallop, J. C., and Lam, S. K. H. *Journal of Applied Physics*, **99**, 123916 (2006).

[31] Ginzburg, V. L. and Landau, L. D. In Haar, D. T. (Editor), *Collected Papers of L.D. Landau: On the Theory of Superconductivity*, pages 546 – 568, (Pergamon, 1965).

[32] Deutscher, G. and de Gennes, P. G. In Parks, R. D. (Editor), *Superconductivity, Volume 2*, (Marcel Dekker Inc, New York, 1969).

[33] Tinkham, M. *Introduction to superconductivity*, (Dover Publications, Mineola, New York, 2004).

[34] Bardeen, J., Cooper, L. N., and Schrieffer, J. R. *Phys. Rev.*, **108**, 1175–1204 (1957).

[35] Zagoskin, A. *Quantum Engineering: Theory and Design of Quantum Coherent Structures*. Quantum Engineering: Theory and Design of Quantum Coherent Structures, (Cambridge University Press, 2011).

[36] Andreev, A. F. *Sov. Phys. JETP*, **19**, 1228 (1964).

[37] Zagoskin, A. *Quantum Theory of Many-Body Systems: Techniques and Applications*. Graduate Texts in Contemporary Physics, (Springer, London, 2012).

[38] Beenakker, C. In Kulik, I. and Ellialtioglu, R. (Editors), *Quantum Mesoscopic Phenomena and Mesoscopic Devices in Microelectronics*, **NATO Science Series**, volume 559, pages 51–60, (Springer, Netherlands, 2000).

[39] Pannetier, B. and Courtois, H. *Journal of Low Temperature Physics*, **118**, 599–615 (2000).

[40] Edwards, J. T. and Thouless, D. J. *Journal of Physics C: Solid State Physics*, **5**, 807 (1972).

[41] Kutchinsky, J., Taboryski, R., Clausen, T., Sørensen, C. B., Kristensen, A., Lindelof, P. E., Bindslev Hansen, J., Schelde Jacobsen, C., and Skov, J. L. *Phys. Rev. Lett.*, **78**, 931–934 (1997).

[42] Josephson, B. *Physics Letters*, **1**, 251–253 (1962).

[43] Likharev, K. K. *Rev. Mod. Phys.*, **51**, 101–159 (1979).

[44] de Gennes, P. G. *Rev. Mod Phys*, **36**, 225–237 (1964).

[45] Dubos, P., Courtois, H., Pannetier, B., Wilhelm, F. K., Zaikin, A. D., and Schön, G. *Physical Review B*, **63**, 064502 (2001).

[46] Wilhelm, F., Zaikin, A., and Schön, G. *Journal of Low Temperature Physics*, **106**, 305–310 (1997).

[47] Courtois, H., Gandit, P., and Pannetier, B. *Phys. Rev. B*, **52**, 1162–1166 (1995).

[48] Spivak, B. Z. and Khmelnitskii, D. E. *JETP Lett.*, **35**, 412 (1982).

[49] Petrashov, V. T., Antonov, V. N., Delsing, P., and Claeson, R. *Phys. Rev. Lett.*, **70**, 347–350 (1993).

[50] de Vegvar, P. G. N., Fulton, T. A., Mallison, W. H., and Miller, R. E. *Phys. Rev. Lett.*, **73**, 1416–1419 (1994).

[51] Petrashov, V. T., Antonov, V. N., Delsing, P., and Claeson, T. *Pis'ma Zh. Eksp. Teor. Fiz*, **60**, 689–594 (1994).

[52] Petrashov, V. T., Antonov, V. N., Delsing, P., and Claeson, T. *Phys. Rev. Lett.*, **74**, 5268–5271 (1995).

[53] Nazarov, Y. V. and Stoof, T. H. *Phys. Rev. Lett.*, **76**, 823–826 (1996).

[54] Lambert, C. J. and Raimondi, R. *Journal of Physics: Condensed Matter*, **10**, 901 (1998).

[55] Kastalsky, A., Kleinsasser, A. W., Greene, L. H., Bhat, R., Milliken, F. P., and Harbison, J. P. *Phys. Rev. Lett.*, **67**, 3026–3029 (1991).

[56] Courtois, H., Charlat, P., Gandit, P., Mailly, D., and Pannetier, B. *Journal of Low Temperature Physics*, **116**, 187–213 (1999).

[57] Volkov, A. F. and Pavlovsky, V. P. *Proceedings of Moriond International Symposium on Correlated Fermions and Transport in Mesoscopic Systems* (1996).

[58] Maki, K. *Progress of Theoretical Physics*, **41**, 902–918 (1969).

[59] Thompson, R. S. *Phys. Rev. B*, **1**, 327–333 (1970).

[60] Volkov, A. F. and Takayanagi, H. *Phys. Rev. B*, **56**, 11184–11194 (1997).

[61] Charlat, P., Courtois, H., Gandit, P., Mailly, D., Volkov, A. F., and Pannetier, B. *Phys. Rev. Lett.*, **77**, 4950–4953 (1996).

[62] Petrashov, V. T., Shaikhaidarov, R., and Sosnin, I. A. *JETP Lett.*, **64 (11)**, 839 (1996).

[63] Petrashov, V. T., Shaikhaidarov, R., Sosnin, I. A., Delsing, P., Claeson, T., and Volkov, A. *Phys. Rev. B*, **58**, 15088–15093 (1998).

[64] Seviour, R., Lambert, C., and Leadbeater, M. *Superlattices and Microstructures*, **25**, 639 – 645 (1999).

[65] Courtois, H., Gandit, P., Mailly, D., and Pannetier, B. *Phys. Rev. Lett.*, **76**, 130–133 (1996).

[66] van Wees, B. J., den Hartog, S. G., and Morpurgo, A. F. *Phys. Rev. Lett.*, **76**, 1402 (1996).

[67] Likharev, K. K. *Dynamics of Josephson Junctions and Circuits*, (Gordon and Breach Publishers, Amsterdam, 1986).

[68] Checkley, C. *Andreev Interferometry of Flux Qubits Driven by Radio Frequency Field*. Ph.D. thesis, Royal Holloway, University of London (2009).

[69] Barone, A. and Paternò, G. *Physics and applications of the Josephson effect*, (Wiley, 1982).

[70] Morpurgo, A. F., Klapwijk, T. M., and van Wees, B. J. *Applied Physics Letters*, **72**, 966–968 (1998).

[71] Klapwijk, T. *Journal of Superconductivity*, **17**, 593–611 (2004).

[72] Wilhelm, F. K., Schön, G., and Zaikin, A. D. *Phys. Rev. Lett.*, **81**, 1682–1685 (1998).

[73] Volkov, A. F. *Phys. Rev. Lett.*, **74**, 4730–4733 (1995).

[74] Pothier, H., Guéron, S., Birge, N., Esteve, D., and Devoret, M. *Zeitschrift für Physik B Condensed Matter*, **104**, 178–182 (1997).

[75] Pothier, H., Guéron, S., Birge, N. O., Esteve, D., and Devoret, M. H. *Phys. Rev. Lett.*, **79**, 3490–3493 (1997).

[76] Guéron, S. *Quasiparticles in a diffusive conductor: Interaction and pairing*. Ph.D. thesis, CEA Saclay (1997).

[77] Morpurgo, A., Baselmans, J., van Wees, B., and Klapwijk, T. *Journal of Low Temperature Physics*, **118**, 637–651 (2000).

[78] Heikkila, T. *Superconducting Proximity Effect in Mesoscopic Metals*. Ph.D. thesis, Helsinki University of Technology (2002).

[79] Baselmans, J. J., Morpurgo, A. F., van Wees, B. J., and Klapwijk, T. M. *Nature*, **397**, 43 (1999).

[80] Baselmans, J. J., van Wees, B. J., and Klapwijk, T. M. *Physical Review B*, **63**, 094504 (2001).

[81] Shaikhaidarov, R., Volkov, A. F., Takayanagi, H., Petrashov, V. T., and Delsing, P. *Phys. Rev. B*, **62**, R14649–R14652 (2000).

[82] Huang, J., Pierre, F., Heikkilä, T. T., Wilhelm, F. K., and Birge, N. O. *Phys. Rev. B*, **66**, 020507 (2002).

[83] Mooij, J. E., Orlando, T. P., Levitov, L., Tian, L., van der Wal, C. H., and Lloyd, S. *Science*, **285**, 1036–1039 (1999).

[84] Chiorescu, I., Nakamura, Y., Harmans, C. J. P. M., and Mooij, J. E. *Science*, **299**, 1869–1871 (2003).

[85] Petrashov, V. T., Chua, K. G., Marshall, K. M., Shaikhaidarov, R. S., and Nicholls, J. T. *Physical Review Letters*, **95**, 147001 (2005).

[86] Chua, K. G. *Andreev Interferometry with Superconducting Persistent Current Qubits*. Ph.D. thesis, Royal Holloway, University of London (2005).

[87] Marshall, K. M. *An Andreev Probe of Superconducting Quantum Circuits*. Ph.D. thesis, Royal Holloway, University of London (2007).

[88] Marsh, R. *Superconducting Phase Coherent Electron Transport In Nano-engineed Ferromagnetic Vortices*. Ph.D. thesis, Royal Holloway, University of London (2012).

[89] Wells, J. *Mutual Proximity Effects in Hybrid Superconducting-Ferromagnetic Nanostructures*. Ph.D. thesis, Royal Holloway, University of London (2013).

[90] Giazotto, F., Peltonen, J. T., Meschke, M., and Pekola, J. P. *Nature Physics*, **6**, 254–259 (2010).

[91] Madou, M. J. *Fundamentals of microfabrication: the science of miniaturization*, (CRC Press, Boca Raton, FL, 2002).

[92] Harriott, L. R. *Proceedings of the IEEE*, **89**, 366–374 (2001).

[93] Bhushan, B. *Springer Handbook of Nanotechnology.* Gale virtual reference library, (Springer, 2007).

[94] Kyser, D. and Viswanathan, N. S. *Journal of Vacuum Science and Technology*, **12**, 1305–1308 (1975).

[95] Balshaw, N. H. *Practical Cryogenics: An Introduction to Laboratory Cryogenics*, (Oxford Instruments, Scientific Research Division, 1996).

[96] White, G. K. and Meeson, P. J. *Experimental Techniques in Low-Temperature Physics*, (Oxford University Press, Oxford2002).

[97] London, H., Clarke, G. R., and Mendoza, E. *Phys. Rev.*, **128**, 1992–2005 (1962).

[98] London, H. *Proceedings of the International Conference on Low-Temperature Physics, Oxford* (1951).

[99] Hall, H. E., Ford, P. J., and Thompson, K. *Cryogenics*, **6**, 80 (1966).

[100] Neganov, B. S., Borisov, N., and Liburg, M. *Sov. Phys. JETP*, **23**, 959 (1966).

[101] Nichols, G. *A Torsional Oscillator Study of Solid Helium.* Ph.D. thesis, Royal Holloway University of London (2013).

[102] Nichols, G. Private Communication.

[103] Antonov, V. Private Communication.

[104] Martinis, J. M., Devoret, M. H., and Clarke, J. *Phys. Rev. B*, **35**, 4682–4698 (1987).

[105] Lukashenko, A. and Ustinov, A. V. *Review of Scientific Instruments*, **79**, 014701 (2008).

[106] Iagallo, A. *Observation of metastable states in a superconducting Josephson circuit using an Andreev Interferometer*. Ph.D. thesis, Royal Holloway University of London (2011).

[107] Checkley, C., Iagallo, A., Shaikhaidarov, R., Nicholls, J. T., and Petrashov, V. T. *Journal of Physics: Condensed Matter*, **23**, 135301 (2011).

[108] Fuechsle, M., Bentner, J., Ryndyk, D. A., Reinwald, M., Wegscheider, W., and Strunk, C. *Phys. Rev. Lett.*, **102**, 127001 (2009).

[109] Lisenfeld, J. *Experiements on Superconducting Josephson Phase Quantum Bits*. Ph.D. thesis, Universitat Erlangen-Nurnberg, (2007).

[110] Harris, R., Johnson, M. W., Han, S., Berkley, A. J., Johansson, J., Bunyk, P., Ladizinsky, E., Govorkov, S., Thom, M. C., Uchaikin, S., Bumble, B., Fung, A., Kaul, A., Kleinsasser, A., Amin, M. H. S., and Averin, D. V. *Phys. Rev. Lett.*, **101**, 117003 (2008).

[111] Siddiqi, I., Vijay, R., Pierre, F., Wilson, C. M., Metcalfe, M., Rigetti, C., Frunzio, L., and Devoret, M. H. *Phys. Rev. Lett.*, **93**, 207002 (2004).

[112] Siddiqi, I., Vijay, R., Metcalfe, M., Boaknin, E., Frunzio, L., Schoelkopf, R. J., and Devoret, M. H. *Phys. Rev. B*, **73**, 054510 (2006).

[113] Lupascu, A., Driessen, E. F. C., Roschier, L., Harmans, C. J. P. M., and Mooij, J. E. *Phys. Rev. Lett.*, **96**, 127003 (2006).

[114] Shelly, C. D., Matrozova, E. A., and Petrashov, V. T. *Resolving the Thermoelectric Paradox in Superconductors* - unpublished (2014).

[115] Petrashov, V. T. unpublished (2014).

[116] Billauer, E. http://www.billauer.co.il/peakdet.html (2012).

[117] Zhang, Z. *Nano/Microscale Heat Transfer*, (McGraw-Hill Education, 2007).

[118] Karvonen, J. T., Taskinen, L. J., and Maasilta, I. J. *Phys. Rev. B*, **72**, 012302 (2005).

[119] Giazotto, F., Heikkilä, T. T., Luukanen, A., Savin, A. M., and Pekola, J. P. *Rev. Mod. Phys.*, **78**, 217–274 (2006).

[120] Wellstood, F. C., Urbina, C., and Clarke, J. *Phys. Rev. B*, **49**, 5942–5955 (1994).

[121] Timofeev, A. V., Garcia, C. P., Kopnin, N. B., Savin, A. M., Meschke, M., Giazotto, F., and Pekola, J. P. *Phys. Rev. Lett.*, **102**, 017003 (2009).

[122] Ginzburg, V. L. and Zharkov, G. F. *Soviet Physics Uspekhi*, **21**, 381 (1978).

[123] Pobell, F. *Matter and Methods at Low Temperatures*, (Springer, 2007).

[124] Mamin, H. J., Clarke, J., and Van Harlingen, D. J. *Phys. Rev. B*, **29**, 3881–3890 (1984).

[125] Kalenkov, M. S., Zaikin, A. D., and Kuzmin, L. S. *Phys. Rev. Lett.*, **109**, 147004 (2012).